NAVAL POSTGRADUATE SCHOOL

MONTEREY, CALIFORNIA

THESIS

NON LINEAR INTERNAL WAVES: MODELING OF THEIR INFLUENCE ON ACOUSTIC MODE ENERGY FLUCTUATIONS AND CHARACTERIZATION USING SAR SYSTEMS

by

Alban Simon

December 2007

Thesis Co-advisors:
John A. Colosi
Philip A. Durkee

Approved for public release; distribution is unlimited

THIS PAGE INTENTIONALLY LEFT BLANK

REPORT DOCUMENTATION PAGE		*Form Approved OMB No. 0704-0188*
Public reporting burden for this collection of information is estimated to average 1 hour per response, including the time for reviewing instruction, searching existing data sources, gathering and maintaining the data needed, and completing and reviewing the collection of information. Send comments regarding this burden estimate or any other aspect of this collection of information, including suggestions for reducing this burden, to Washington headquarters Services, Directorate for Information Operations and Reports, 1215 Jefferson Davis Highway, Suite 1204, Arlington, VA 22202-4302, and to the Office of Management and Budget, Paperwork Reduction Project (0704-0188) Washington DC 20503.		
1. AGENCY USE ONLY *(Leave blank)*	**2. REPORT DATE** December 2007	**3. REPORT TYPE AND DATES COVERED** Master's Thesis
4. TITLE AND SUBTITLE Non Linear Internal Waves: Modeling of Their Influence on Acoustic Mode Energy Fluctuations and Characterization using SAR Systems		**5. FUNDING NUMBERS**
6. AUTHOR(S) Alban Simon		
7. PERFORMING ORGANIZATION NAME(S) AND ADDRESS(ES) Naval Postgraduate School Monterey, CA 93943-5000		**8. PERFORMING ORGANIZATION REPORT NUMBER**
9. SPONSORING /MONITORING AGENCY NAME(S) AND ADDRESS(ES) N/A		**10. SPONSORING/MONITORING AGENCY REPORT NUMBER**
11. SUPPLEMENTARY NOTES The views expressed in this thesis are those of the author and do not reflect the official policy or position of the Department of Defense or the U.S. Government.		
12a. DISTRIBUTION / AVAILABILITY STATEMENT Approved for public release; distribution is unlimited		**12b. DISTRIBUTION CODE**
13. ABSTRACT (maximum 200 words) Non Linear Internal Waves (NLIW) are ubiquitous and appear wherever a proper combination of stratified water, current and bathymetry occur. In recent years, they have also been proven of primary interest for acoustic oceanography, since they are known to play an important role in sound speed fluctuations in shallow waters. The predictability of acoustic variability caused by these waves has been somewhat limited, and largely based on direct numerical simulation. Through this project, we present a simple and computationally efficient analytic model based on coupled mode theory. For this purpose, narrow and broadband acoustic normal mode fluctuations in the 2001 South China Sea ASIAEX experiment are first examined. Then ASIAEX environmental data are used to characterize the space/time scales of NLIW sound speed structure. Finally, a comparison is conducted between the observed normal mode variability and the predictions from an analytic model utilizing the observed NLIW structure, such as its width, amplitude and speed. As the model proves to be very sensitive to these characteristics, an overview of the Synthetic Aperture Radar capabilities to retrieve them is also conducted. In this latter part of the project, particular attention is given to wind effects on SAR data.		
14. SUBJECT TERMS Shallow Water Acoustics, Non Linear Internal Waves, Soliton, Mode Coupling, Synthetic Aperture Radar, ASIAEX		**15. NUMBER OF PAGES** 111
		16. PRICE CODE
17. SECURITY CLASSIFICATION OF REPORT Unclassified	**18. SECURITY CLASSIFICATION OF THIS PAGE** Unclassified	**19. SECURITY CLASSIFICATION OF ABSTRACT** Unclassified	**20. LIMITATION OF ABSTRACT** UU

NSN 7540-01-280-5500

Standard Form 298 (Rev. 2-89)
Prescribed by ANSI Std. 239-18

THIS PAGE INTENTIONALLY LEFT BLANK

NON LINEAR INTERNAL WAVES: MODELING OF THEIR INFLUENCE ON ACOUSTIC MODE ENERGY FLUCTUATIONS AND CHARACTERIZATION USING SAR SYSTEMS

Alban Simon
Lieutenant, French Navy
M.S., French Naval Academy, 2001

Submitted in partial fulfillment of the
requirements for the degree of

**MASTER OF SCIENCE IN PHYSICAL OCEANOGRAPHY
AND
MASTER OF SCIENCE IN METEOROLOGY**

from the

**NAVAL POSTGRADUATE SCHOOL
December 2007**

Author: Alban Simon

Approved by: John A. Colosi
                 Thesis Co-Advisor

                 Philip A. Durkee
                 Thesis Co-Advisor

                 Mary L. Batteen
                 Chairman, Department of Oceanography

                 Philip A. Durkee
                 Chairman, Department of Meteorology

iii

THIS PAGE INTENTIONALLY LEFT BLANK

ABSTRACT

Non Linear Internal Waves (NLIW) are ubiquitous and appear wherever a proper combination of stratified water, current and bathymetry occur. In recent years, they have also been proven of primary interest for acoustic oceanography, since they are known to play an important role in sound speed fluctuations in shallow waters. The predictability of acoustic variability caused by these waves has been somewhat limited, and largely based on direct numerical simulation. Through this project, we present a simple and computationally efficient analytic model based on coupled mode theory. For this purpose, narrow and broadband acoustic normal mode fluctuations in the 2001 South China Sea ASIAEX experiment are first examined. Then ASIAEX environmental data were used to characterize the space/time scales of NLIW sound speed structure. Finally, a comparison is conducted between the observed normal mode variability and the predictions from an analytic model utilizing the observed NLIW structure, such as its width, amplitude and speed. As the model proves to be very sensitive to these characteristics, an overview of the Synthetic Aperture Radar capabilities to retrieve them is also conducted. In this latter part of the project, particular attention is given to wind effects on SAR data.

THIS PAGE INTENTIONALLY LEFT BLANK

TABLE OF CONTENTS

LIST OF FIGURES

LIST OF TABLES

THIS PAGE INTENTIONALLY LEFT BLANK

ACKNOWLEDGMENTS

THIS PAGE INTENTIONALLY LEFT BLANK

I. INTRODUCTION

With the emergence of asymmetric threats, modern naval warfare has moved from the deep ocean to the shallow waters, a fact that has necessitated a thorough understanding of this complex and variable environment. With regards to acoustics, much attention has been paid to the variability of the bottom geology and geoacoustic parameters due to the importance of bottom interaction in shallow water acoustics. However, it has also been recognized in recent years that the water column and its fluctuations also have a large impact on modulating acoustic signal in shallow water (Headrick et al., 2000, Duda and Preisig, 1999). One aspect of this variability includes non linear internal waves (NLIWs), the so-called solitons or Internal Solitary Waves (ISW). These waves are accompanied by huge vertical displacements of water, upward or downward in accordance with the local density profile, and they affect significantly sound speed profiles. Thus, the present thesis aims at improving the understanding and prediction of the influence of solitons on sound propagation in shallow waters. Toward this end, this thesis tests a Dyson series-based method presented by Colosi (2007) using in-situ data collected during the Asian Seas International Acoustic Experiment (ASIAEX), conducted in May 2001 in the Northeastern South China Sea. Because of the importance of the inner characteristics of solitons in this theory, such as their half-width or their amplitude, this paper will also present an overview of the remote sensing techniques used to detect and characterize them. Particular attention was given to the wind effects while retrieving this information.

A. OVERVIEW ON NON LINEAR INTERNAL WAVES

Apel et al. (2007) have provided a thorough review of non linear internal waves and solitons, and this section presents only some of the main characteristics.

As their name implies, internal waves travel within the interior of the ocean and are particularly characterized by strong vertical anomalies in temperature. As illustrated in Figure 1, non linear internal waves are ubiquitous, appearing wherever the proper

combination of stratified waters, currents, and bathymetry occur. This characteristic makes them of primary interest from a military perspective.

Solitons tend to occur in packets, usually rank-ordered, with the largest oscillations appearing at the packet front. They generally precede an oscillating undulatory bore associated with a depression of the equilibrium pycnocline. Despite the growing interest on this topic, their generation is still ill monitored; however, hydraulic control by seamounts or continental shelves during energetic tidal cycles seems to be an adequate explanation in many cases (Ramp, 2006, personal communication). However, their physical characteristic show significant modulations on diurnal, fortnightly, seasonal and semiannual time scales, and these changes are greatly associated with the changes in the water column stratification. Furthermore, non linear internal waves are evolving events. Actually, as they propagate, their shape shifts from a single, relatively sharp peak to a series of spikes, one oscillation being added per Brunt-Vaisala frequency. They also tend to slow down before finally being dissipated by different mechanisms, among which are radial spreading, bottom interaction, instability and fluid turbulence (Apel et al., 2002). The lifetime of a soliton is on the order of a few days in the open sea to a day on the continental shelf.
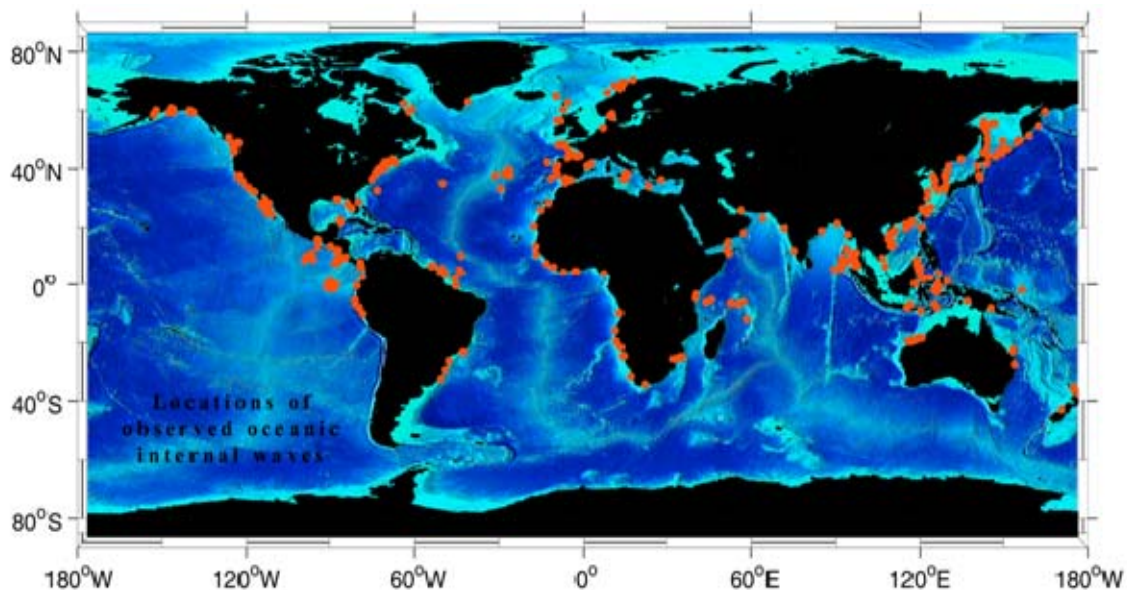
Figure 1.   Locations of internal wave imagery and data presented in *Internal solitons in the ocean and their effect on underwater sound* (Apel et al., 2007).

2

The first scientists to give mathematical representation to this phenomenon were Korteweg and De Vries (KdV) in 1897 who based their work on the observations made by Russel in 1838 and 1844. Since this original work, many additional solitary wave equations have been derived, and new solutions, such as the dnoidal representations, have been found. However, the KdV equation or the extended KdV equation (Apel et al., 2007) offer results whose accuracy is sufficient for the purpose of this project and will be used to characterize non linear internal waves.

Solitons can be described by a product of solutions to the weakly non linear KdV equation, $D(x,t)$, and the eigenfunctions of the Taylor-Goldstein equation for the vertical structure function $W_{k,n}(z)$:

$$\eta(x,z,t) = \sum_{n=1}^{n_{max}} \eta_{0n}.W_{k,n}(z).D_n(x,t) \tag{1.1}$$

$D(x,t)$, the normalized vertical displacement of an isopycnal surface from its equilibrium level, and $W_{k,n}(z)$ are the solutions of the two following equations:

$$\frac{\partial D}{\partial t} + c_0 \left[\frac{\partial D}{\partial x} + \alpha.D.\frac{\partial D}{\partial x} + \gamma \frac{\partial^3 D}{\partial x^3} \right] = 0 \tag{1.2}$$

$$\frac{d^2 W_{k,n}}{dz^2} + k^2.\left[\frac{N^2(z) - \omega^2}{\omega^2 - f^2} \right].W_{k,n}(z) = 0 \tag{1.3}$$

In the three previous equations, α, γ and c_0 are environmental coefficients describing the nonlinearity, the dispersion and the phase speed associated with the waves, and are functions of the reduced gravity and the thicknesses of the upper and lower layers as illustrated with the following equations; f represents the Coriolis parameter. Thus, if h_1 is the thickness of the upper layer and h_2 the thickness of the lower layer, then α, β and c_0 are defined by:

$$\alpha = \frac{3}{2}.\frac{c_0}{h_1.h_2}.\frac{\rho_2.h_1^2 - \rho_1.h_2^2}{\rho_2.h_1 + \rho_1.h_2}, \tag{1.4}$$

3

$$\beta = \frac{c_0.h_1.h_2}{6} \cdot \frac{\rho_1.h_1 + \rho_2.h_2}{\rho_2.h_1 + \rho_1.h_2} \quad \text{and} \tag{1.5}$$

$$c_0 = [\frac{g.h_1.h_2.(\rho_2 - \rho_1)}{\rho_2.h_1 + \rho_1.h_2}]^{1/2}. \tag{1.6}$$

$N(z)$ is the buoyancy frequency, k characterizes the horizontal wavenumber of the soliton and ω is the radial frequency. Two boundary conditions finally add to make this set of equations a Sturm-Liouville system. The description of the physics behind the ISWs using a two-layer model is convenient since it offers a simple interpretation of the problem, nevertheless, any of the three previous parameters α, γ and c_0, as well as the ISW mode functions can currently be calculated using a continuous stratification of the water column. In this thesis, both approaches are used, a continuous stratification for the section dedicated to the acoustics fluctuations associated with the solitons and the two-layer model during manipulation of SAR images.

If the shallow water approximation holds and if the upper layer depth is small compared to the width of the soliton, the typical solution for a single soliton pulse is then given by:

$$\eta(x,t) = \eta_0 \sec h^2(\frac{x - Vt}{\Delta}) \tag{1.7}$$

where $\Delta = \sqrt{\frac{12\beta}{\alpha.\eta_0}}$ is the characteristic width and $V = c_0 + \frac{\alpha.\eta_0}{3}$, the so called non linear speed. Figure 2 represents $\eta(x,t)$ as described by equation 1.7 whereas Figure 3 shows the dnoidal model, a more realistic but more complex solution to equations 1.2 and 1.3. ISWs are often seen as depression associated with downward vertical displacements of surface waters, elevation or upward water displacements are also observable particularly in very shallow waters where h_1 can be greater than h_2.

In this report, equation 1.7 operates for $\eta(x,t)$ in the section dedicated to the remote parameterization of solitons using SAR systems, but is approximated by a Gaussian profile during work with solitons and acoustics in shallow water (Young, 2006).
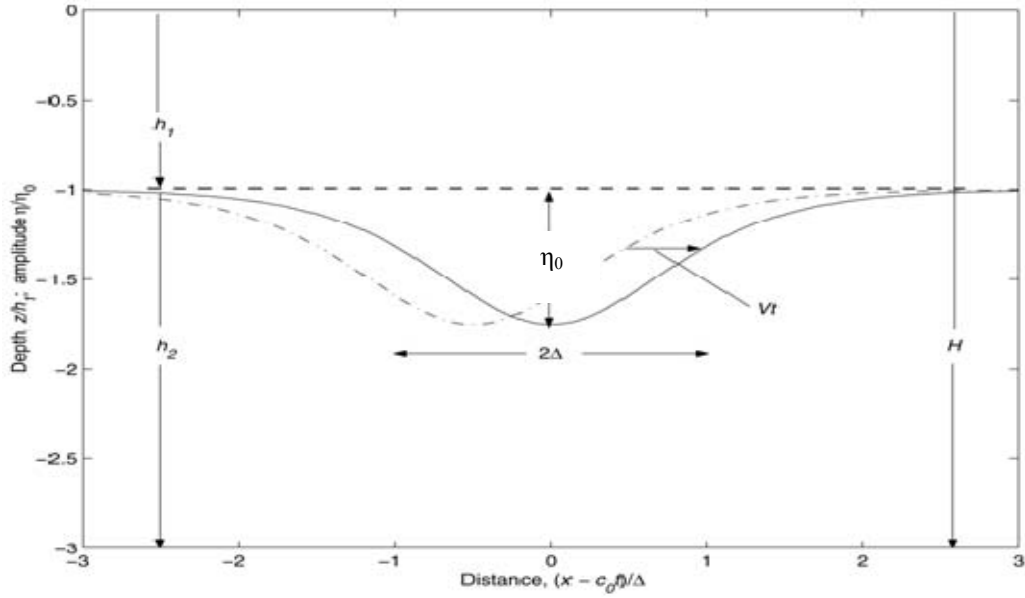
Figure 2.   Classic secant profile for KdV soliton at two different times, viewed in a moving coordinate system. Adapted from *Internal solitons in the ocean and their effect on underwater sound* (Apel et al, 2007).
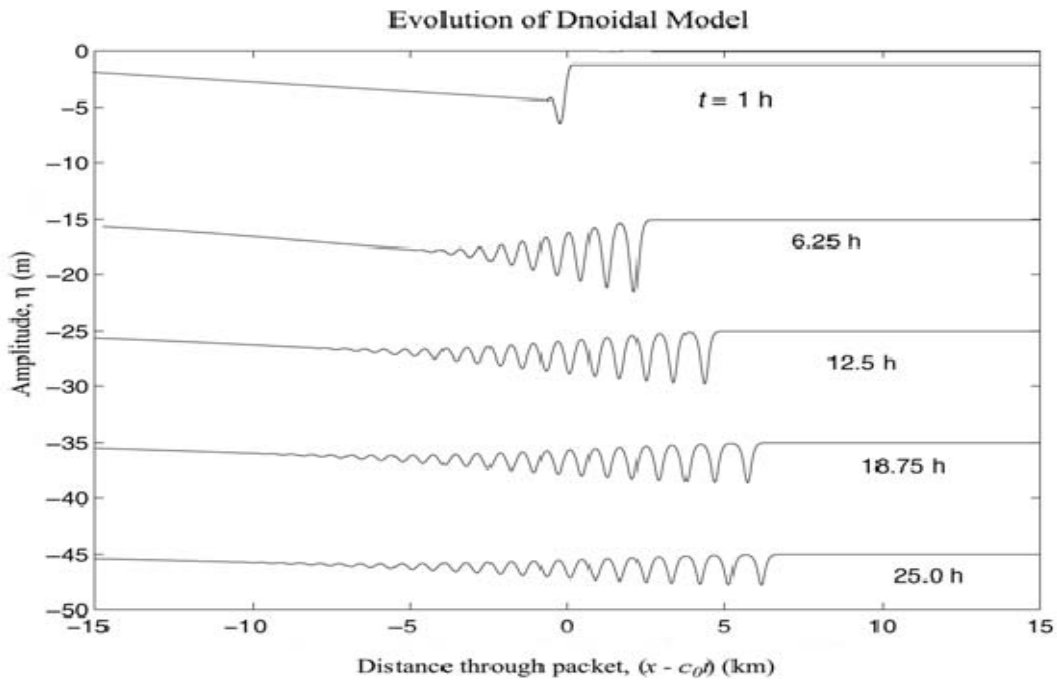
Figure 3.   Dnoidal model evolution over one diurnal period. This model includes the vertical structure function and attenuation, and adds one cycle every buoyancy period. Adapted from *Internal solitons in the ocean and their effect on underwater sound* (Apel et al., 2007).

5

B.   THE ASIAEX PROGRAM

To support all the results presented here, this project used data collected in the South China Sea (SCS) during the second leg of the Asian Seas International Acoustics Experiment (ASIAEX) which took place in April and May 2001. The goal of the SCS project was to understand acoustic propagation through shallow water when strong variability in the form of fronts, eddies, and internal waves, is present (Ramp et al., 2004). In essence, the project was a progression from previous similar coupled physical oceanography and acoustics experiments, namely the Shallow Water Acoustic Random Media (SWARM) (Headrick et al. (2000)) and Shelfbreak PRIMER (Lynch et al. (1997)) experiments. As an added benefit, this experiment presented a unique opportunity for international cooperation in oceanography and a significant effort to improve the knowledge of non linear internal waves that occur significantly in this strategic area. Numerous works were published about this experiment, particularly in volume 29, number 4 of the IEEE Journal of Oceanic Engineering published in October 2004. The current section presents only the data used for this project.
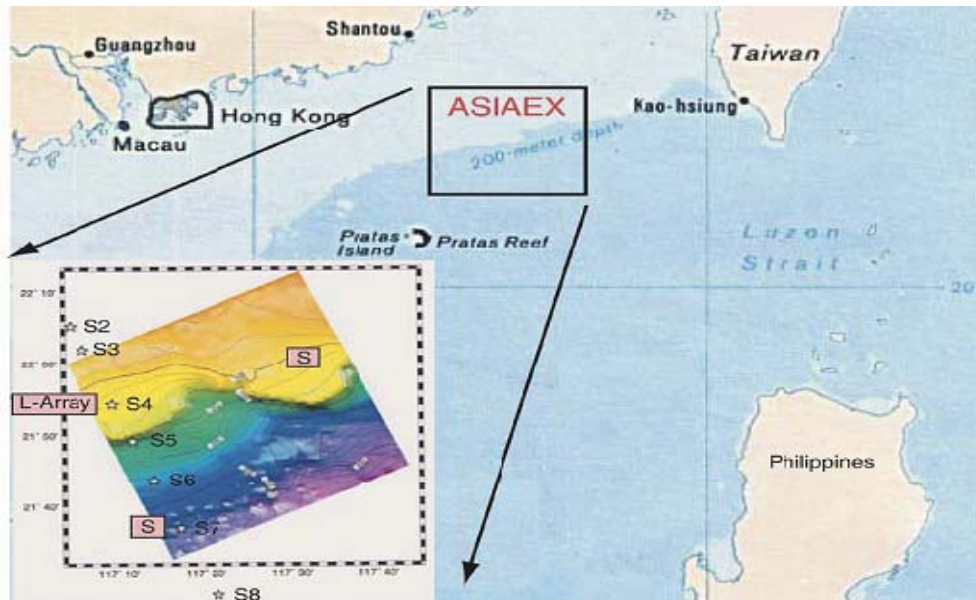
Figure 4.   Map showing the locations of the ASIAEX moorings. The oceanographic moorings are indicated by stars labeled S2-S8. The shaded red boxes indicate acoustic assets, with an "S" indicating sources and "L-Array" the receiving arrays. Adapted from *Internal Solitons in the Northeastern South China Sea. Part I: Sources and Deep Water Propagation* (Ramp et al., 2004).

6

In order to get a close look at the effects of solitons on sound propagation in this shallow and variable environment, measurements of water column properties but also vertical and horizontal distributions of acoustic pressure were collected using numerous moorings (Figure 4). To resolve the high variability of the medium, temperature, salinity and pressure were collected at high resolution in space and time. In particular, the array consisted of seven densely instrumented oceanographic moorings deployed across the continental shelf. With this configuration, the moorings spanned depths from 800m to 72m, along the primary acoustic paths, recording at a 2 minute-sampling rate (Ramp et al, 2004). During this experiment, Ramp et al., described carefully the generation and propagation of the solitons under observation and particularly noted the evolution of the solitons as they moved shoreward. Actually, Ramp et al., discerned that the extended KdV model gave better results than the basic KdV theory in a description of the solitons as they shoal. The former theory cannot adequately account for the changes in wave shape and speed. Numerous results concerning the amplitude, speed and width were also collected.

Regarding sound transmission, one sound source operating at 224 and 400Hz was deployed on the 350m-isobath. The source transmitted phase-modulated signals at a carrier frequency of 400 Hz with a bandwidth of 100 Hz and a source level of 180 dB (1 μPa). Frequencies on the order of a few hundreds hertz are actually known to limit scattering and bottom effects. The phase modulation employed was a 5.11-s-long511-digit pseudorandom sequence resulting in a compressed pulse of 10 ms-resolution after matched filtering. The acoustic data were received by an L-shaped hydrophone array, 16 were moored vertically in the water column and 32 hydrophones horizontally. The sampling was realized at a rate of 3.2 kHz over the first three weeks of May 2001 (Chiu et al., 2004). This work focused only on data recorded by the vertical array (VLA) for the 400Hz source.

Many significant results arose from these different observations. For instance, Chiu and al. (2004) highlighted the fact that the variability of the sound speed occurred within three distinct spectral domains which they labeled tidal, subtidal or mesoscale, and supertidal, that is due to internal waves. They also discovered that this variability could

disturb the acoustic field by a few decibels due to the vertical redistribution of acoustic energy, particularly in the presence of internal waves. This phenomenon is known as mode coupling; it was already observed during the SWARM experiment and is within the purviews of this work as well.

Concomitantly with this experiment, SAR images of the area were taken and will allow us to look at the relevance of this system in detecting and characterizing solitons. During the time frame of the experiment, only images from the Canadian system RADARSAT were available; these will also be used in this project.

C. STATEMENT OF RESEARCH

1. Acoustics

The present analysis aims to study the acoustic intensity fluctuations, such as time modulation and spreading, caused by the presence of solitons along the acoustic path. For this work, acoustic pressure and energy are described in terms of normal modes. This decomposition originates from the resolution of the Helmholtz equation using a separation of variables technique. The natural frequencies governing this decomposition define mode functions and are highly dependent on the boundary conditions. This common analysis of the propagation of acoustic signals was initially designed for range independent environment but can also be generalized to range dependent medium. However, in these latter kinds of environment, normal modes are generally no longer independent, which may conduct to the vertical redistribution of acoustic energy. Three main points of views are commonly expressed regarding this topic: adiabatic approximation, weak mode coupling and strong mode coupling. With the first approximation, interaction between modes is neglected, this assumption was proven to be erroneous regarding this topic (Rousseff et al., 2002). The second approximation assumes that the primary interaction occurs between consecutive mode orders and is used all along this thesis. Finally, the third approximation is generally associated with a complex bathymetry where the bottom effects exceed the effects caused by the water column. In

this work, we also looked at this redistribution of acoustic energy by analyzing the exchanges which occurred between modes during the Asian experiment for different environmental conditions.

The second goal of this thesis was to test the ability of a simple and fast analytic model to predict the changes induced by the ISWs. This model designed by Colosi (2007) builds upon works from Dozier and Tappert (1978), Dozier (1982), and Creamer (1996). The model also clarifies the work of Zhou et al., (1991), which noted the resonance condition that exists between various wavenumbers of a NLIW and the beat wavenumbers of the acoustic normal modes. The basic solutions of this problem can take the form of the Dyson series from quantum mechanical perturbation theory (Sakurai (1985)). Indeed, they are designed to solve for the change in modal amplitudes after acoustic propagation through ocean NLIWs. This treatment is confined to coupling in the depth-range space, and thus azimuthal coupling is ignored. Moreover, as this theory only assumes weak single scattering, it is limited to frequencies between 100 and 400Hz and breaks down at higher frequencies. Finally, this approach can treat either single NLIW or packets of NLIWs.

Young (2006) verified the relevance of this theory by successfully testing it against numerical simulation to determine if the total acoustic pressure field could be accurately predicted in an ocean environment with ISWs. The present study aims to validate the theory in a real environment, based on the oceanographic and acoustic data provided by the ASIAEX experiment.

2. Remote Sensing using SAR Images

Synthetic Aperture Radars (SAR) are radar systems which have improved their resolution by extracting information from the spectral shifts caused by Doppler effects. Because of their global coverage and their specifications, SAR satellites act as primary providers for information about NLIWs. As it will be detailed in the fourth chapter of the present document, SAR satellites possess a unique ability to detect these waves by using the interaction between wind waves and the current induced by ISWs (Alpers (1985)). They also allow users to retrieve some essential soliton features such as their half-width,

their wavelength or their amplitude (Liu et al. (2004), Zheng et al. (2001)). These latter characteristics are essential for the previous acoustic considerations.

The goal of the fourth and fifth sections is to synthesize the main results of the works made in the last 20 years regarding soliton detection by SAR systems. Thus, these sections will introduce basic theories about soliton detection by SAR satellites. Attention will particularly focus on two previous works. The first, a study by Zheng et al. (2001), presents an interesting method of retrieving soliton information from SAR images. The second, a study by Liu et al. (2004), gathers the results observed using SAR images during the ASIAEX experiment. As mentioned previously, this work also carefully investigated the wind effects to determine how they can bias the soliton information. Unfortunately, because of the lack of data, the study will offer only a couple of images. Thus, if the statistical aspect of the study does not prove very conclusive, the project still provides an interesting qualitative overview of the advantages and limitations of SAR satellites with regard to this topic.

II.   THEORY AND PRESENTATION OF THE PROCESS

A.   THEORETICAL MODEL

1.   Shallow Water Acoustics

The present model was designed to compute the acoustic intensity fluctuations induced by NLIWs in shallow waters. The model assumes only single weak scattering, and thus provides noteworthy results solely for frequencies ranging from 100 Hz to 400Hz, which are of primary interest for submariners.

Regarding the spectral domain and the distances used, the attenuation of the signal due to the water column is negligible; only the attenuation due to the bottom is considered. Moreover, the model considers that the total acoustic wavenumber will have a small imaginary part:

$$k(r,z,\omega) = \frac{\omega}{c(r,z)} + i.\alpha(z).\qquad(2.1)$$

Here $\alpha(z)$ is the attenuation coefficient and is considered non-zero in the seabed. $c(r,z)$ is the sound speed profile at a distance r from the source and at depth z. k and ω are respectively the wavenumber and the radial frequency of the signal.

The present theory furthers assumes that the incoming soliton will convey an isolated sound speed perturbation to the background sound speed profile. In their study, Chiu et al. (2004) noticed the importance of the tidal and subtidal variabilities; however, the present study sets these effects aside to focus only on the high frequency variability induced by non linear internal waves. With this assumption, one can decompose the sound speed profile, such as:

$$c(r,z) = \overline{c}(z) + \delta c(r,z)\qquad(2.2)$$

where $\overline{c}(z)$ is the background sound speed profile and $\delta c(r,z)$ is a perturbation due to some NLIWs.

The development outlined by Dozier and Tappert(1978), Dozier (1982), and Creamer (1996) decomposes the acoustic pressure field for the radial frequency ω in terms of the acoustic normal modes of the range independent problem such that:

$$p(r,z) = \sum_{n=1}^{N} \frac{A_n(r)}{\sqrt{r}}.\phi_n(z).$$ (2.3)

$A_n(r)$ represents the amplitude and characterizes the range-dependent effects of scattering on acoustic pressure. $A_n(r)$ is a solution of equation 2.6 with $A_n(0)$ being the mode amplitude at the source. $\phi_n(z)$ is the nth normal mode function and is a solution of equation 2.4. Actually, $\phi_n(z)$ represent the unperturbed normal modes calculated in the absence of ISW and all the variability conveyed by the ISWs is included in the amplitude term $A_n(r)$:

$$[\sigma(z)\frac{\partial}{\partial z}\frac{1}{\sigma(z)}\frac{\partial}{\partial z} + \bar{k}^2(z) - l_n^2]\phi_n = 0.,$$ (2.4)

where $\bar{k}(z) = \frac{\omega}{\bar{c}(z)} + i.\alpha(z)$ and $\sigma(z)$ is the background density profile. The orthonormality relation associated with $\phi_n(z)$ is given by: $\int_0^\infty \frac{\phi_n(z).\phi_m(z)}{\sigma(z)}dz = \delta_{mn}$.

In equation 2.4, l_n, the complex wavenumber is written $l_n = k_n + i.\alpha_n$, where k_n is the usual modal wavenumber in the absence of attenuation, and α_n is the complex part of the wavenumber, obtained using the perturbation theory:

$$\alpha_n \approx \frac{\omega}{k_n}\int_0^\infty \frac{\alpha(z).\phi_n^2(z)}{\bar{c}(z).\sigma(z)}dz << k_n.$$ (2.5)

To complete this close Sturm-Liouville problem, the boundary condition at the surface is defined by $\phi_n(z=0)=0$. Then, in order to take into account the bottom attenuation and to keep this model computationally efficient, the bottom boundary condition is chosen to be $\frac{\partial \phi_n}{\partial z}\Big|_{z=h} = 0$ at some seabed depth far below the water-bottom

12

interface, generally 3 or 4 times the bottom depth. Finally, to overcome computational difficulties related to the interface between the water column and the seabed, the discontinuous density or sound speed profiles were substituted by sharp but continuous profiles.

In the quasi-static, narrow angle, weak forward scattering approximation Dozier and Tappert (1978), and Dozier (1982) show that the mode amplitudes can be approximated by the one-way wave equation:

$$\frac{\partial A_n}{\partial r} - i.l_n.A_n = -i.\sum_{m=1}^{N} \rho_{mn}.(\frac{k_m}{k_n})^{1/2}.A_m \tag{2.6}$$

where the symmetric coupling matrix ρ_{mn}, initiated by the perturbed sound speed profile, is given by:

$$\rho_{mn}(r) = \frac{k_0^2}{(k_m.k_n)^{1/2}}.\int_0^\infty \mu(r,z).\frac{\phi_n(z).\phi_m(z)}{\sigma(z)} dz \text{ with } \mu(r,z) = \frac{\delta c(r,z)}{c_0}. \tag{2.7}$$

Here, $k_0 = \dfrac{\omega}{c_0}$ and c_0 is a reference sound speed for the local water column. In equation 2.7, the coupling matrix does not depend on the bathymetry and is only a function of the sound speed perturbation induced by the ISWs. It is one of the strongest assumptions of the model which assumes that the adiabatic approximation holds once the energy is redistributed among the modes by the solitons.

Finally, it is useful to remove the rapid oscillations, which also makes the equation symmetrical, by introducing φ_n such as:

$$\varphi_n(r) = A_n(r).\exp(-i.l_n.r).k_n^{1/2}. \tag{2.8}$$

Then, equation (2.6) becomes:

$$\frac{\partial \varphi_n}{\partial r} = -i.\sum_{m=1}^{N} \rho_{mn}.e^{i.l_{mn}.r} \varphi_m \text{ with } l_{mn} = l_m - l_n. \tag{2.9}$$

13

## 2.	Solution using the Dyson Series

Although it can be significant, the sound speed perturbation induced by a soliton is small compared to the background sound speed and generally less than 30 m/s. From this observation, it can be deduced that ρ_{mn} and μ are small, as expected from equation 2.7, and that the mode coupling is relatively weak. In fact, this strong assumption suggests that the problem can be solved using a perturbation theory, such as may be found in standard quantum mechanics texts. Actually, the Dyson series proved valuable for this purpose and were used to solve this set of equations. Through this approach, it can be shown that:

$$\varphi_n(R) = \varphi_n(0) - i.\sum_{m=1}^{N} \varphi_m(0).\int_0^R \rho_{mn}(r').e^{i.l_{mn}.r'} dr' \qquad (2.10)$$

$$\text{with } \varphi_n(0) = k_n^{1/2}.\int_0^h p(0,z).\frac{\phi_n(z)}{\sigma(z)} dz . \qquad (2.11)$$

$\varphi_n(0)$, like $A_n(0)$ earlier, represents the amplitude of the normal modes at the source and is greatly dependent on the depth of the source. Using the Fourier transform of ρ_{mn}, equation 2.10 becomes:

$$\varphi_n(R) = \varphi_n(0) - i.\sum_{m=1}^{N} \varphi_m(0).\int_{-\infty}^{\infty} \hat{\rho}_{mn}(k).\int_0^R e^{i.(l_{mn}-k).r'} dr'.dk \qquad (2.12)$$

$$\text{with } \hat{\rho}_{mn}(k) = \frac{1}{2\pi}.\int_{-\infty}^{\infty} \rho_{mn}(r).e^{i.k.r} dr .$$

Moreover, for the considered range of frequency, as R is large and α is small, one can approximate $H_{mn}(R,k) = \int_0^R e^{i.(l_{mn}-k).r'} dr'$ by a Dirac function such as $H_{mn}(R,k) \approx 2\pi.\delta(k_{mn}-k)$ where $k_{mn} = k_m - k_n$ is the beat wavenumber between mode m and n. The Dirac representation of $H_{mn}(R,k)$ is really a cornerstone of this model since it enhances the fact that the resonant coupling condition is conditioned by the match between the beat wavenumber and the horizontal wavenumber of the ISW.

14

Finally, the equation becomes:

$$\varphi_n(R) = \varphi_n(0) - i.\sum_{m=1}^{N} \varphi_m(0).J_{mn}(R) \qquad (2.13)$$

with $J_{mn}(R) = \int_{-\infty}^{\infty} \hat{\rho}_{mn}(k).H_{mn}(R,k)dk \approx 2\pi.\hat{\rho}_{mn}(k_{mn})$

and, $A_n(R) = [A_n(0) - i.\sum_{m=1}^{N} (\frac{k_m}{k_n})^{1/2}.A_m(0).J_{mn}(R)].e^{i.l_n.R}$. $\qquad (2.14)$

In this equation, J_{mn} is the scattering matrix for mode m and n. For multiple solitons, because of the linear relationship between $\varphi_n(R)$ and $\rho_{mn}(k)$, J_{mn} will simply becomes: $J_{mn}(R) = \sum_{j=1}^{N_s} \int_{-\infty}^{\infty} \hat{\rho}_{mn}(k,j).H_{mn}(R,k)dk \approx 2\pi.\sum_{j=1}^{N_s} \hat{\rho}_{mn}(k_{mn})$ where N_s is the number of solitons.

3.   Non Linear Internal Wave Sound Speed Perturbations

In the previous set of equations, the sound speed perturbation created by the presence of one or more solitons is included in the variable $\mu(r,z) = \dfrac{\delta c(r,z)}{c_0}$. Munk and Zachariasen (1976) derived the following equation for μ including the internal wave vertical displacement:

$$\mu(r,z) = \frac{\delta c(r,z)}{c_0} = -\frac{1}{c_0}.(\frac{dc}{dz})_p.\zeta(r,z) = -\frac{1}{c_0}.(\frac{dc}{dz})_p.\zeta_0.W_1(z).F(r) . \qquad (2.15)$$

In this equation, $(\dfrac{dc}{dz})_p$ represents the potential sound speed gradient which is used because internal waves move water parcels adiabatically. The shape of the vertical displacement induced by a soliton was already presented in section I.A and is reduced to the first mode of equation 1.1 as it is generally assumed in the literature. $F(r)$ is essentially described by equation 1.7 but is approximated with a Gaussian soliton in this section as described by Young (2006). It is important to note that changes in the NLIW as

15

it propagates, specifically its bore-like structure, are not considered; these changes introduce analytical complexities which encumber the computational efficiency of the model. However, the linear decay of the waves with the bathymetry is simulated. Finally, one can rewrite equation 2.7 thus:

$$\rho_{mn}(r) = \frac{k_0^2}{(k_m.k_n)^{1/2}} \cdot \int_0^\infty \mu(r,z) \cdot \frac{\phi_n(z).\phi_m(z)}{\sigma(z)} dz = C_{mn}.F(r) \tag{2.16}$$

$$\text{with } C_{mn} = -\frac{\zeta_0}{c_0} \frac{k_0^2}{(k_m.k_n)^{1/2}} \cdot \int_0^\infty (\frac{dc}{dz})_p.W_1(z).\frac{\phi_n(z).\phi_m(z)}{\sigma(z)} dz. \tag{2.17}$$

Here matrix C_{mn} characterizes the contribution to coupling due to the vertical structure of the acoustic modes and of the soliton. As such, C_{mn} is determined by the overlap between the depth structure of the NLIW and modes n and m. For a packet of Gaussian solitons located at the distance $r_0(j)$ from the source, one can rewrite J_{mn} such that:

$$J_{mn}(R) = \sum_{j=1}^{N_s} C_{mn}(j).K_{mn}(j) \text{ with } K_{mn}(j) \approx \sqrt{\pi}.\Delta(j).e^{-\frac{k^2.\Delta(j)^2}{4}+i.r_0(j).t}. \tag{2.18}$$

As explained in section II.A.2, H_{mn} can be viewed as a Dirac function centered on k_{mn}, and then, using equations 2.15 and 2.18, the equation becomes:

$$A_n(R) = [A_n(0) - i.\sqrt{\pi}\sum_{j=1}^{N_s}\sum_{m=1}^{N}(\frac{k_m}{k_n})^{1/2}.A_m(0).C_{mn}(j).\Delta(j).e^{-\frac{k_{mn}^2.\Delta(j)^2}{4}+i.r_0(j).t}].e^{i.l_n.R}. \tag{2.19}$$

The latter equation quantifies the mode energy for the nth mode received at a distance R from the source when a group of ISWs are located at the distances $r_0(j)$. This equation can be considered as time dependent, since it oscillates with the displacement of the ISW whose position is given by $r_0(j)$, and is then a function of time. Moreover, as $A_n(R)$ is still a complex number, it contains both amplitude and phase information. Later, this analysis will involve separation of these two quantities and introduction of the expressions for the mode energy and the time spread.

16

Equation 2.19 also emphasizes the role of the main parameters involved in this problem, particularly $A_n(0)$, the amplitude at the source which sets an average value, $\Delta(j)$ the width of the jth ISW and the beat wavenumber k_{mn}, which act together to modulate the oscillations. Actually, k_{mn} plays a significant role for neighbor modes only. Finally the coupling matrix $C_{mn}(j)$ clearly appears as a centerpiece of the perturbation.

B.   ANALYSIS

1.   Preliminaries

As introduced earlier, the goal of this project consisted in applying this theory to in-situ data in order to check its relevance for operational purposes. Hence, all the acoustic and oceanographic data involved in the numerous computations presented in this work were provided by the acoustic array described in section I. The local temperature was measured at eight different levels at S4 and S5 and at 16 levels at S7, while salinity measurements were respectively collected at three, five and four different levels at the three locations. Along the vertical array, 16 hydrophones expanded from the 42m-depth to the bottom, located 120m below the surface, and recorded acoustic pressure at 3.2 kHz.

Based on the temperature variations in time and depth at these three locations, three periods of time were thought to be of first interest for this analysis. These simple temporal windows were ultimately chosen because they were highly characteristic of a fluctuating environment. Thus, a first sequence with a single soliton, a second one with a well-defined soliton packet and finally, a third one presenting no soliton activity were used. The last sequence is taken as a reference for periods with very little acoustic fluctuation. The first timeframe extends from May 5, 2001 around 1945GMT to May 6, 2001 around 0100GMT. During that period, a single soliton propagated shoreward along the acoustic path, its characteristic half-width evolved from 240m near S7 to 290m near S4, its speed was estimated to be around 2 m/s between S7 and S5 and slow down to 1 m/s between S5 and S4, its amplitude also varied from 65 to 40 m. Compared to the results presented by Duda et al. (2004) or Ramp et al. (2004), this soliton seems to be

much faster between S7 and S5 but this latter result is only an artifact. The direction in which the soliton propagated was not parallel to the acoustic path; therefore, the pulse did not cross perpendicularly with the soliton. Then, with respect to the pulse, the wave appeared larger and seemed to propagate faster. Moreover, the decrease in speed after S5 was probably due to the interaction between the soliton and the bottom. It was accompanied by a horizontal spreading and a vertical squeezing of the soliton which refracted as it shoaled.

The second sequence occurred on May 6, 2001 between 0700GMT and 1500GMT. The soliton packet was composed of three solitons, the same spreading/squeezing phenomenon and decrease in speed were observed as the solitons moved to the coast. In that case, the initial amplitude of the leading soliton was 110 m and decreased to 60m as it passed S4. The characteristic half-widths varied from 320m to 450m. The third environment was observed on May 7 between 0330GMT and 0730GMT.
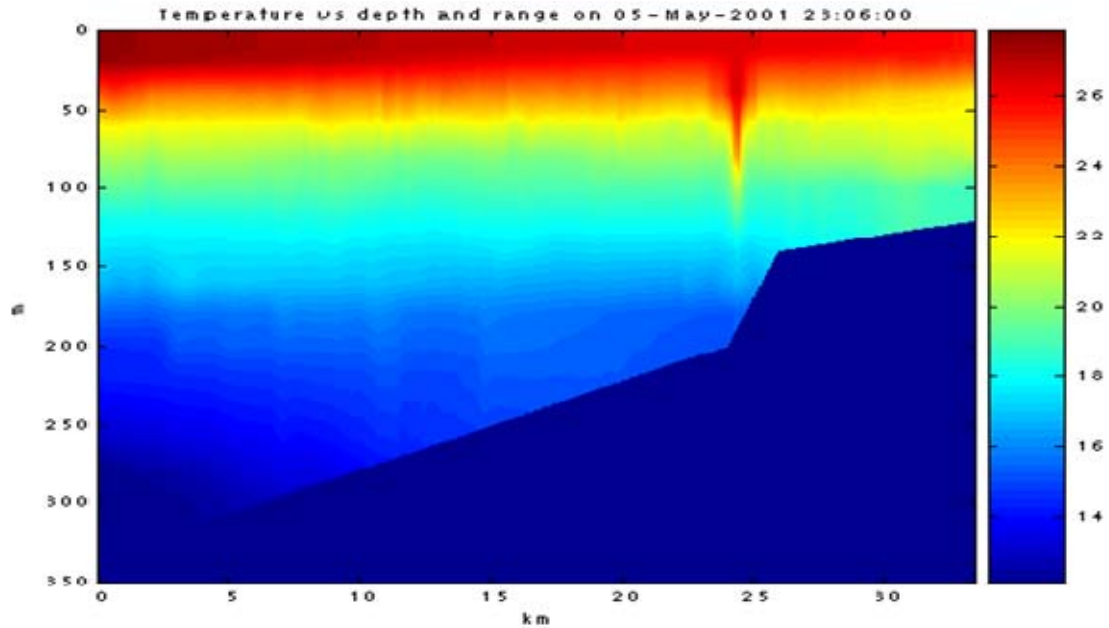
Figure 5.   Temperature field from mooring S7 (x=0) to mooring S4 (x=33km) on May 5, 2001 at 2306GMT.

It is noted here that the observed values for characteristic width or speed at S7 and S5 still agree quite well with the theory described in section I which is not true anymore when the wave interacts with the bottom between S5 and S4.

18
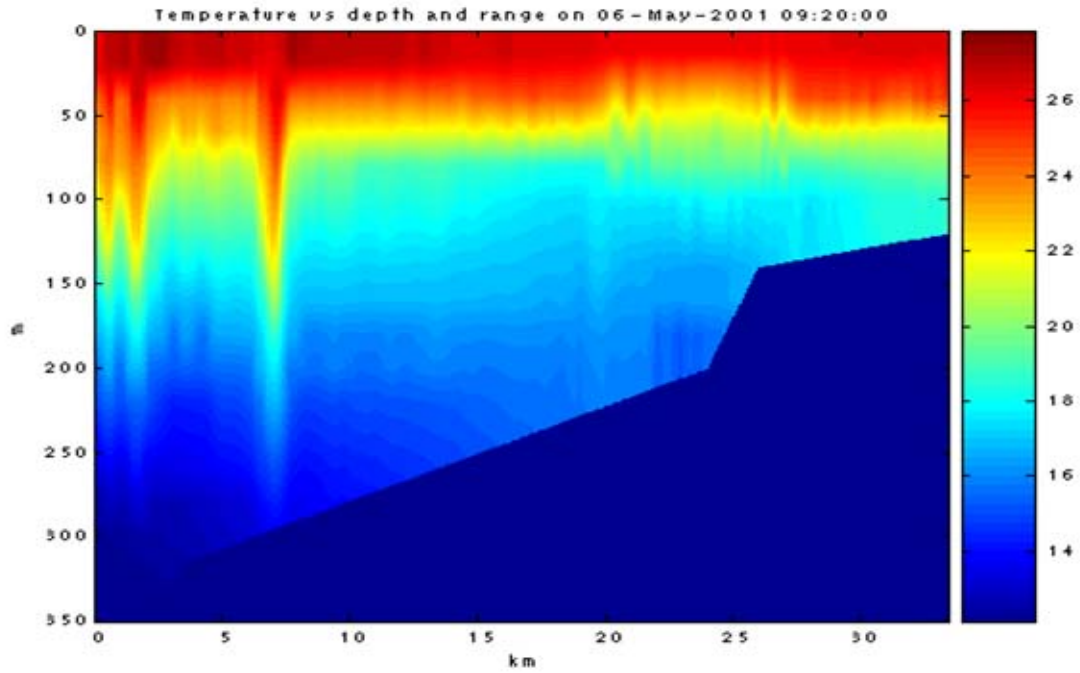
Figure 6.   Temperature field from mooring S7 (x=0) to mooring S4 (x=33km) on
May 6, 2001 at 0920GMT.
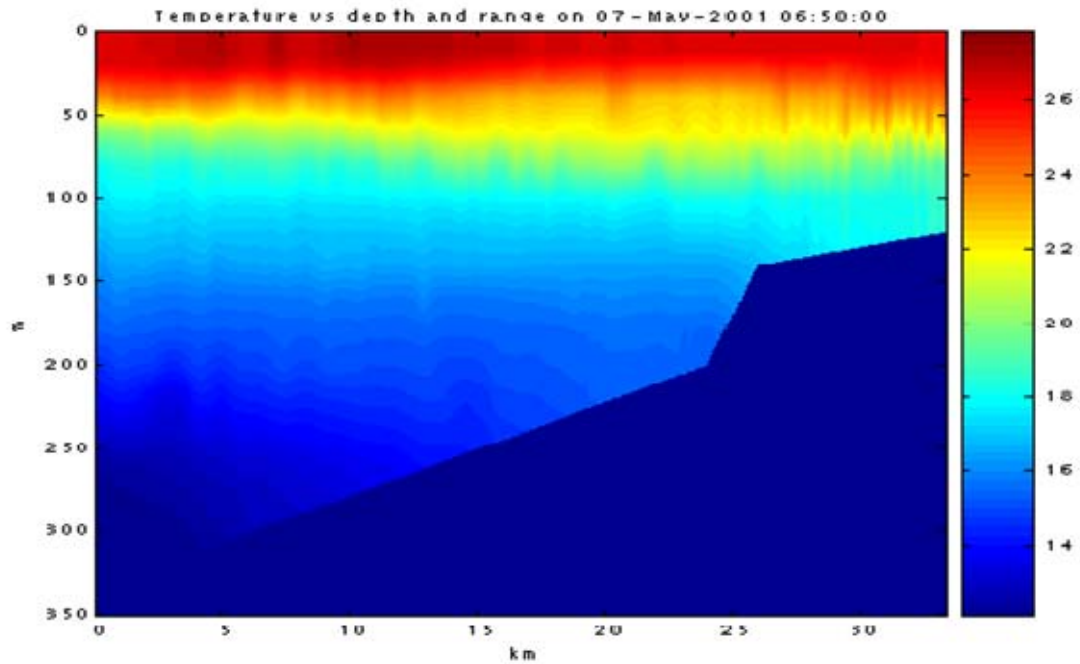
Figure 7.   Temperature field from mooring S7 (x=0) to mooring S4 (x=33km) on
May 7, 2001 at 0650GMT.

Once these three periods of time were identified, the second step of the project consisted in determining the associated background sound speed profiles which would serve as input in the theoretical model. These background profiles were based on the recorded temperature, pressure and salinity measured at S7 and S4. In order to remove the effect of the non linear internal waves in these calculations, a low pass filter was also applied to the data. As illustrated in Figure 8, the profile did not change significantly from one time to another, or between S7 and S4. A slight decrease in sound speed, around 2m/s, was observed between S7 and S4 in the presence of solitons. This effect may have been caused by the bore-like trail of the soliton on the measurements at mooring S7, which was hit first by the waves.
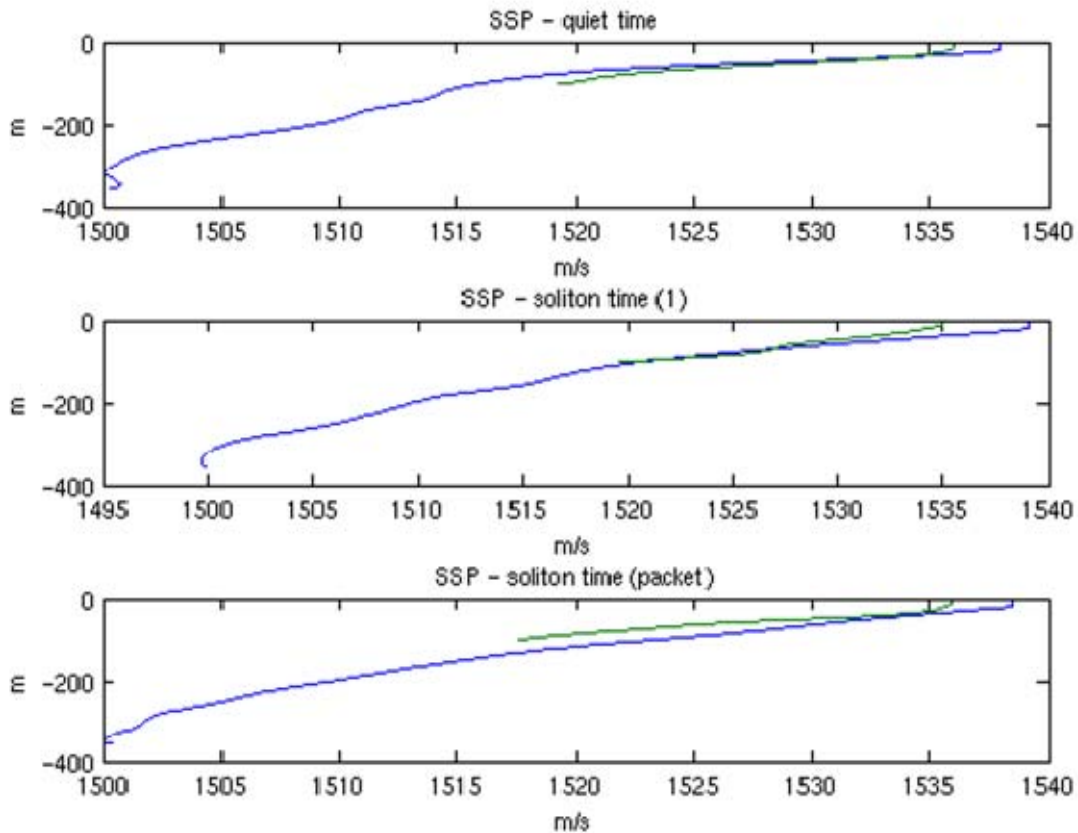
Figure 8.   Background sound speed profiles for the three periods of time: quiet time, 1st soliton time (1) and 2nd soliton time (packet) at S7 (blue) and S4 (green).

The third step of this work consisted in calculating the normal modes associated with these environments for a 400Hz-source with a 100Hz bandwidth. However, only the normal modes evaluated at S4 for a 400Hz-source were used in this theory. This calculation does not present a great computational challenge but does raise two important questions regarding the influence of the bathymetry and the frequency dependence of the normal modes. The observations and assumptions resulting from these interrogations are presented in the next sections.

The final step of this project was the basic comparison of the modal amplitudes calculated through the simple analytic model with those retrieved from the modal decomposition of the acoustic pressure, measured on the hydrophones as the soliton propagated between the source and the VLA. All these results are presented in the third chapter of this report. As the acoustic pressure was recorded on a discrete array of only 16 deep hydrophones, the next section addresses the relevance of this comparison by analyzing the cross-talk matrix.

2. Assumptions

Young and Colosi (2006) tested the present theory against the simulation to determine if the total acoustic pressure field can be predicted in a flat bottom ISW environment. For this purpose, they used different frequencies, source depths, a theoretical point source and Gaussian solitons. Although their results were conclusive, this present study will test the theory in a realistic environment with in-situ data and a variable bathymetry. With regard to simulation, comparisons of theoretical results to observed measurements present other challenges. Specifically, the discrete and relatively small number of hydrophones moored during ASIAEX 2001 raises a central question: is it possible to compare objectively simulated data from this theory with observed data collected through only 16 hydrophones? Then, if the model works well for a point source, one must also anticipate its behavior with regard to a pulse covering a larger spectral band.

a.   *Frequency Dependence:Mode Processing of ASIAEX Data*

From the normal mode theory as seen previously, for a source at a depth z_s, the acoustic pressure field at the radial frequency ω_0 and at a range R can be written such that:

$$p(z,t) = \sum_{n=1}^{N} a_n(\omega_0).\phi_n(\omega_0,z).e^{-i\omega_0 t} \qquad (2.20)$$

with $a_n(\omega_0) = \phi_n(\omega_0,z_s).e^{il_n(\omega_0)R}$.

For this mode processing test in an unperturbed environment, this work considers only acoustic losses caused by attenuation due to the bottom and omit, for computational efficiency, cylindrical spreading and attenuation due to the water column.

By applying the standard orthonormality relation, one then obtains:

$$a_m(\omega_0) = \phi_m(\omega_0,z_s).e^{ik_m(\omega_0)R} = e^{i\omega_0 t}\int_{-\infty}^{0} \frac{p(z,t).\phi_m(\omega_0,z_s)}{\rho(z)}dz \; . \qquad (2.21)$$

For a pulse, the pressure will be given by:

$$p(z,t) = \sum_{n=1}^{N}\int_{\omega_0-\Delta\omega}^{\omega_0+\Delta\omega} a_n(\omega).\phi_n(\omega,z).e^{-i\omega t}d\omega \; . \qquad (2.22)$$

The theory states that frequency plays a role in the definition of the normal modes at a particular location. However, as shown below in Figure 9, it appears that its influence is negligible compared to the amplitude of the modes for a 100Hz-spectral window. This statement can also be verified for any other modes and is generally truer near the bottom than near the surface. Thus, one can assume that $\phi_n(\omega,z) \approx \phi_n(\omega_0,z)$ at any depth and for any frequency.
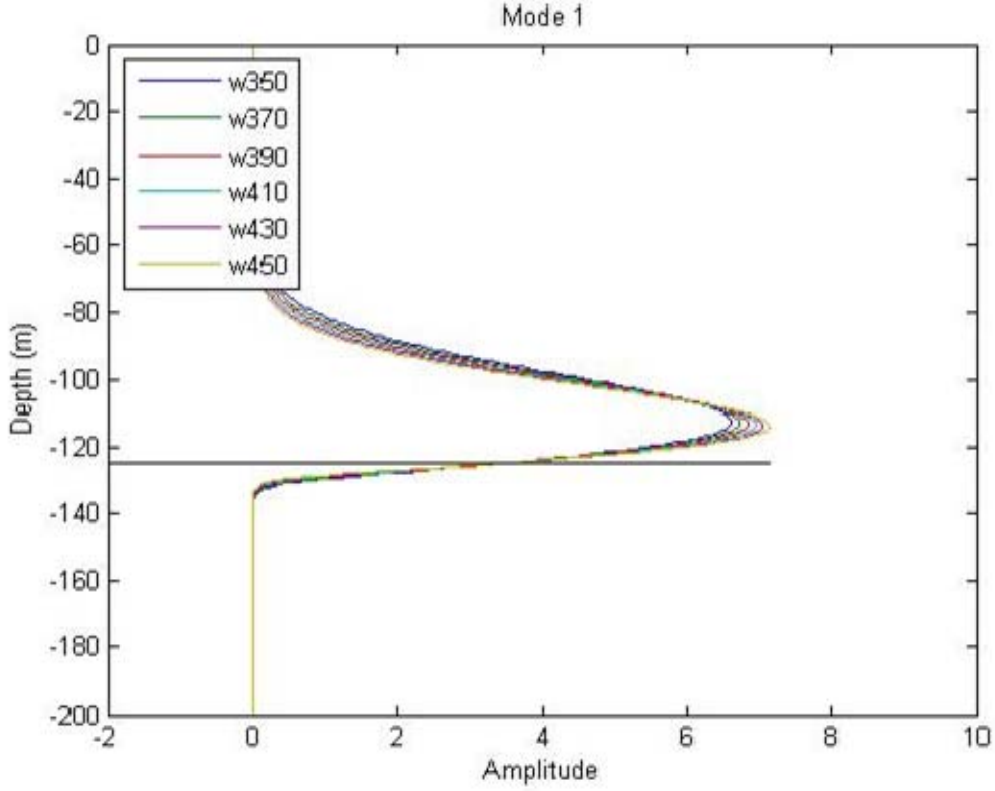
Figure 9.   Comparison of first normal modes obtained at the location of the VLA
(depth =125m) for different frequencies ranging from 350 Hz to 450 Hz.

From the previous definitions, it is also apparent that the frequency influences the
phase of the acoustic pressure field through the phase term $e^{i(l_n(\omega)R-\omega t)}$. In order to account
for the different phase speeds of the various frequencies and dispose of the phase term,
one can introduce the modal group speed and make the following approximation:

$$\int\limits_{\omega_0-\Delta\omega}^{\omega_0+\Delta\omega} a_n(\omega).e^{-i\omega t}d\omega = \int\limits_{\omega_0-\Delta\omega}^{\omega_0+\Delta\omega} \phi_n(\omega,z_s).e^{i(l_n(\omega)R-\omega t)}d\omega \approx \phi_n(\omega_0,z_s).\int\limits_{\omega_0-\Delta\omega}^{\omega_0+\Delta\omega} e^{i(l_n(\omega)R-\omega t)}d\omega \qquad (2.23)$$

$$\int\limits_{\omega_0-\Delta\omega}^{\omega_0+\Delta\omega} a_n(\omega).e^{-i\omega t}d\omega \approx \phi_n(\omega_0,z_s).e^{il_n(\omega_0)R}.\int\limits_{\omega_0-\Delta\omega}^{\omega_0+\Delta\omega} e^{-i\omega(t-t_n)}d\omega \text{ where } t_n = R/\frac{\partial\omega}{\partial k_n}. \qquad (2.24)$$

In order to evaluate this result, one compares simulated pressure fields with and without the approximation. Figure 10 illustrates the relevance of one such calculation.

Comparison between data1(no approximation) and data2(approximation)
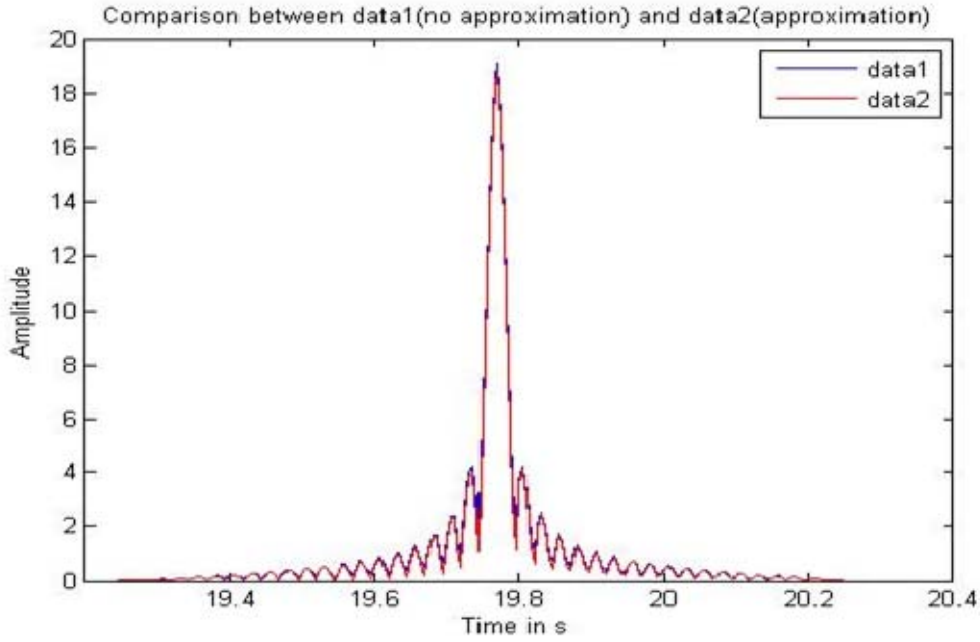
Figure 10.   Comparison between the acoustic pressures calculated at a distance R=30km from the source ($f_0 = 400Hz$ - $\Delta f = 20Hz$) with (data1) and without (data2) any approximation of the amplitude and the phase term regarding frequency.

Using (2.21), (2.23) and (2.24), the equation becomes:

$$a_m(\omega_0) = \phi_m(\omega_0, z_s).e^{ik_m(\omega_0)R} \approx \frac{1}{F_m(t)} \int_{-D}^{0} \frac{p(z,t).\phi_m(\omega_0, z_s)}{\rho(z)} dz \qquad (2.25)$$

$$\text{where } F_m(t) = \int_{\omega_0 - \Delta\omega}^{\omega_0 + \Delta\omega} e^{-i\omega(t-t_m)} d\omega.$$

From these results, one can assume the possibility of amplitude retrieval for any modes based on the acoustic pressure field and the normal mode theory. Thus, evaluation of the model's accuracy is easily achievable by comparing these values to those simulated by the model.

24

b.   Cross-Talk Matrix

Because of the discrete number of hydrophones, the orthonormality matrix, also called the cross talk matrix, is not the perfect identity and tends to skew results. For a discrete array, the orthonormality matrix (Γ_{mn}) is also approximated by:

$$\Gamma_{mn} = \int_{-D}^{0} \frac{\phi_m(z).\phi_n(z)}{\rho(z)} dz \approx \sum_{j=1}^{16} \frac{\phi_m(z_j).\phi_n(z_j)}{\rho(z_j)}\Delta z \;.$$

(2.26)

As it is represented in the following figure, the orthormality matrix is no longer perfect; the diagonal terms are not all equal to one and some of the non-diagonal terms are not null. However, because only the first modes are of interest, this matrix still proves promising. Indeed, for the 5 first modes, the diagonal terms are still greater than 0.9 which appears to be strong enough for the purpose of this study. Note that this theory would partly break for a shallow source since the energy would be concentrated in higher modes in that case.
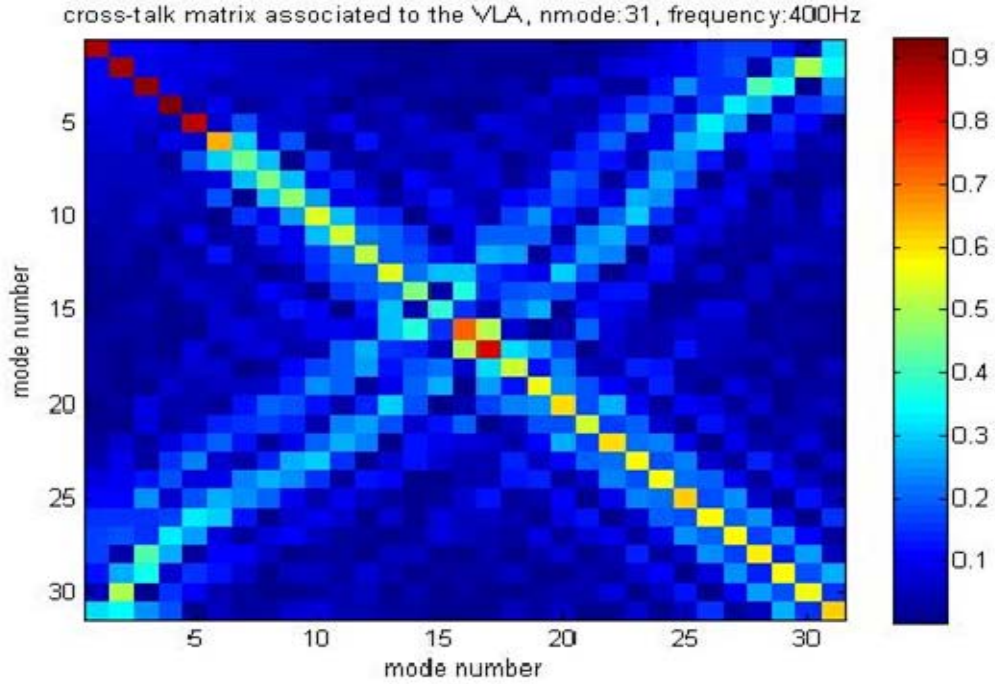
Figure 11.   Cross-talk matrix for a sparse array of 16 hydrophones – the frequency is 400Hz and the number of retained modes is 31 modes (trapped modes).

25

The last step of this preparatory work is to check the ability to retrieve the amplitude of the acoustic pressure at a distance R equal to 30 kilometers from the perfect source in an undisturbed environment and with a sparse array, through equations 2.27, 2.28 and 2.29.

$$(a_m(\omega_0))_{m\in[1,6]} = (\phi_m(\omega_0, z_s).e^{ik_m(\omega_0)R})_{m\in[1,6]} \tag{2.27}$$

$$(a_m(\omega_0))_{m\in[1,6]} = (\sum_{j=1}^{16} \frac{\phi_m(\omega_0, z_j).p(z_j,t)}{F_m(t)})_{m\in[1,6]} = (D_m)_{m\in[1,6]} \tag{2.28}$$

$$(a_m(\omega_0))_{m\in[1,6]} = (\sum_{j=1}^{16} \frac{\phi_m(\omega_0, z_j).p(z_j,t)}{F_m(t)})_{m\in[1,6]} = (D_m)_{m\in[1,6]}.(\Gamma_{mn}^{-1})_{\substack{m\in[1,6]\\n\in[1,6]}}. \tag{2.29}$$

Note: Equations 2.28 and 2.29 calculate the same coefficients but a perfect cross-talk matrix is assumed in equation 2.28 while the observed one is used in equation 2.29.
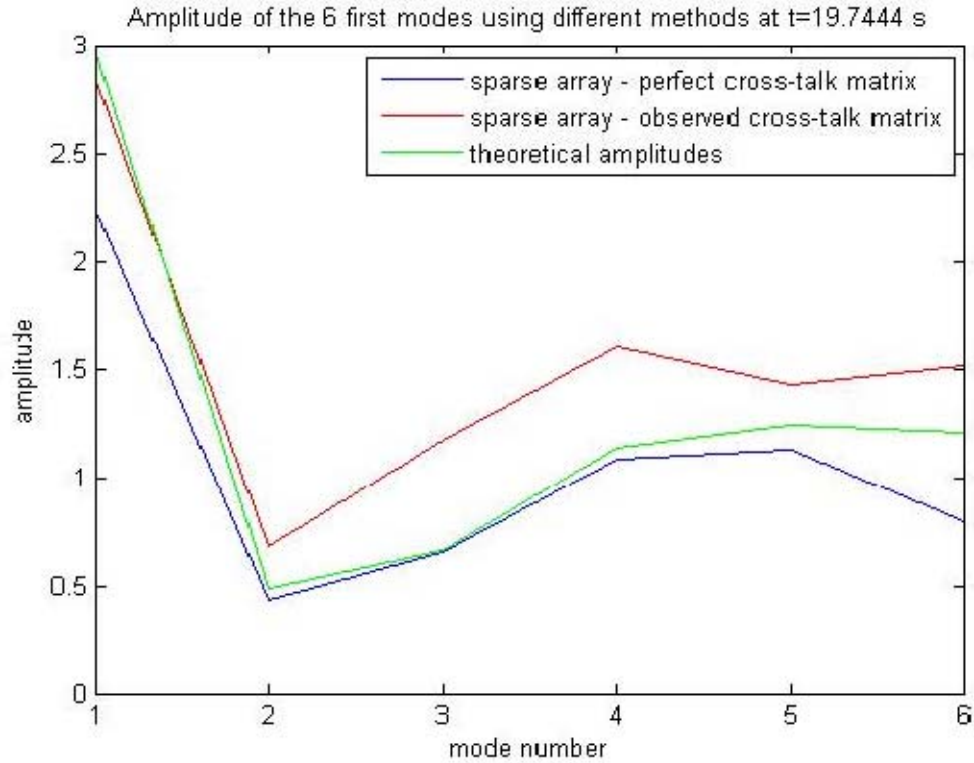
Figure 12.   Comparison of the mode amplitude (amplitude only) recorded 30 km away from the source, and retrieved using three different methods.

26

Based on the results displayed in the above picture, one may conclude that equation (2.28) should be accurate enough to obtain the amplitude of the first six modes. From that, one may evaluate the relevance of this theory by examining mode coupling as the solitons appear.

THIS PAGE INTENTIONALLY LEFT BLANK

III.   RESULTS AND OBSERVATIONS (1)

A.   GENERAL COMMENTS ABOUT THE ENERGY RECEIVED AT THE VLA

Using the acoustic pressure measurements recorded at the receiver, this study was able to retrieve the mode amplitudes for the first three modes, which were used to conduct the comparison. Indeed, this model assumes both weak coupling between modes and adiabatic propagation of the mode energy. Combined with the deep location of the source, these two assumptions make these modes the most energetic and relevant for this project.

As they will appear frequently in the following figures and comments, it is also important to introduce the two time scales that frame the observations. The first one, t, corresponds to the geotime and sets the temporal reference of the experiment with regard to the Greenwich Mean Time (GMT). This time scale is somewhat discontinuous, since it only accounts for the beginning of each sequence and each pulse. In fact, the acoustic data observed at the array were not recorded continuously; rather sequences of 88 pulses were sent every 30 minutes from the source, 5.11 seconds separating the launch of two successive pulses. Then, only seven minutes of acoustic information were recorded per sequence and are available for this comparison. Any referenced time in Figure 13, 15 or 17, such as 1815GMT or 1845GMT, is also a composition of 88 pulses, which are vertically displayed. Due to technical issues, it was not possible to retrieve the acoustic pressure for all the pulses in sequences such as 2345GMT or 0045 GMT in Figure 13; these sequences also appear narrower on the display. A second time scale, named τ, was also introduced to analyze the data. This second temporal scale represents pulse travel time between the source and the receiver.

Finally, this study chose to work with the mode acoustic energy, defined by:

$$I_n(t,\tau) = |A_n(t,\tau)|^2.$$ (3.1)

29

Thus, Figures 13, 15 and 17 display the relative mode acoustic energy for mode 1 with respect to t and τ for any of the three case studies presented in the second chapter. The energy is expressed in decibels in these three figures and represents the fluctuations in mode energy relative to the maximum mode energy observed during the sequence, which is assumed to be similar to the energy at the source. Only mode 1 is presented here. However, the results for mode 2 and 3 looked quite similar.

Figures 14, 16 and 18 show the 400Hz component of the mode energy for the three case studies. Instead of working with the whole broadband pulse, this study chose to extract the 400Hz component from the signal for the initial analysis; the narrowband comparison is then simpler since the spreading induced by the non linear coupling between modes is removed. Additionally, this central frequency carries the main acoustic information.
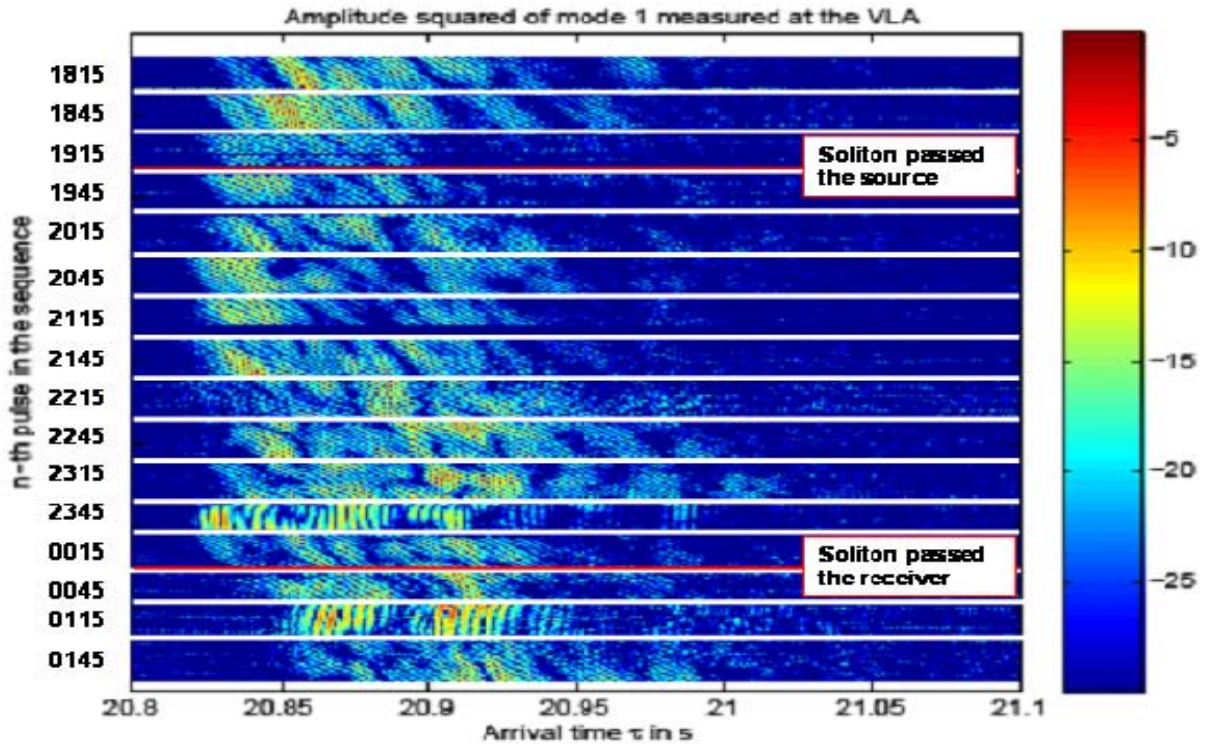
Figure 13.   Relative Mode energy for mode 1(in dB) received at the VLA between 1815 GMT on May 5, 2001 and 0145GMT on May 6. A few soliton locations are indicated with the red lines.

Finally, this section compares the results obtained during the first and second case studies, when solitons were present in the acoustic path, to the results observed during the third case, which this work has called quiet time.
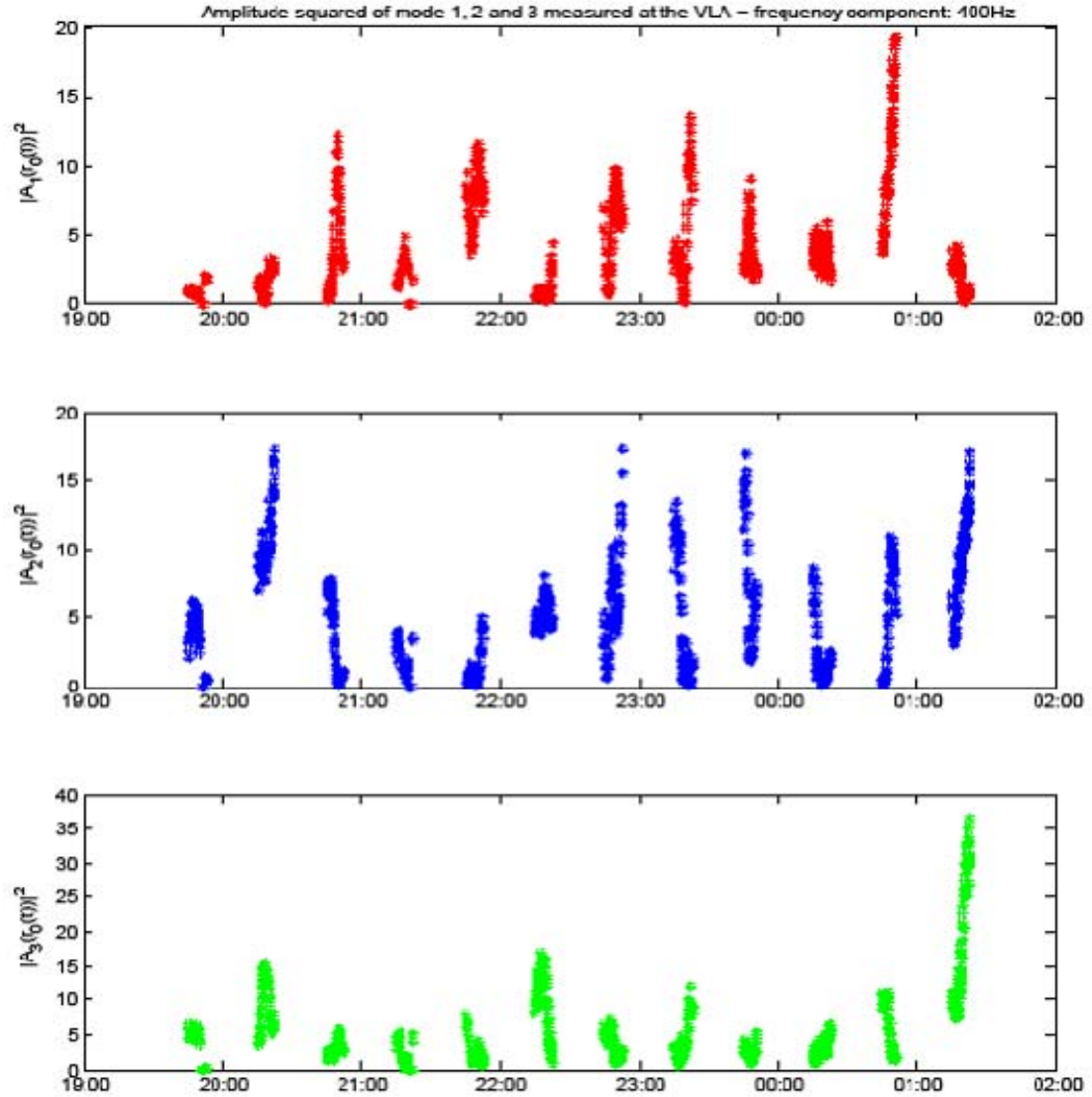
Figure 14. Temporal variations of the 400Hz component of the mode acoustic energy recorded at the VLA for mode 1, 2 and 3 between May 5, 2001 at 1945GMT and May 6, 2001 at 0145GMT.

Starting with this first case study, a few main characteristics are readily noticeable. First, as shown in Figure 13 compared to Figure 17, the signal seems to be more spread in time. Moreover, the analysis of the 400Hz signal (Figure 14) emphasizes the fact that the signal fluctuates more quickly as an ISW enters the acoustic path. Then, in the presence of solitons, mode energy also seems to decrease on average, as illustrated by the comparison of Figures 14 and 18. On May 5 (Figure 14) and 6 (Figure 16) mode 1 and 2 seem to convey a little bit less energy in the presence of solitons than during the quiet time (Figure 18), while mode 3 seems to carry more energy. Many of the referenced papers talk about mode coupling and describe how this phenomenon was observed while dealing with acoustics and solitary internal waves; this theory also forms the core of the model presented in Chapter II and is responsible for the exchanges of energy between modes. Rousseff et al. (2002) detailed these exchanges of energy, but this paper focuses only on the predictability of these exchanges rather than quantifying the observed coupling.
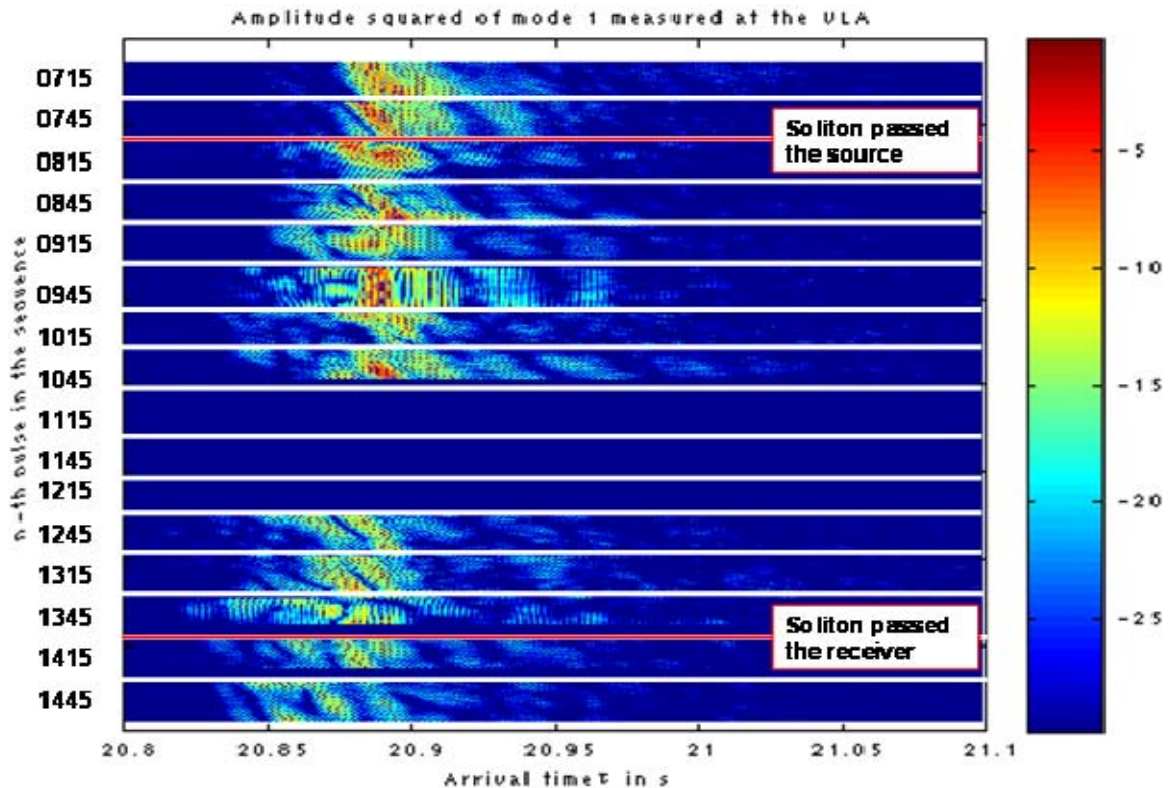
Figure 15.   Same as Figure 13 for a signal observed between 0700 GMT and 1500GMT on May 6, 2001.
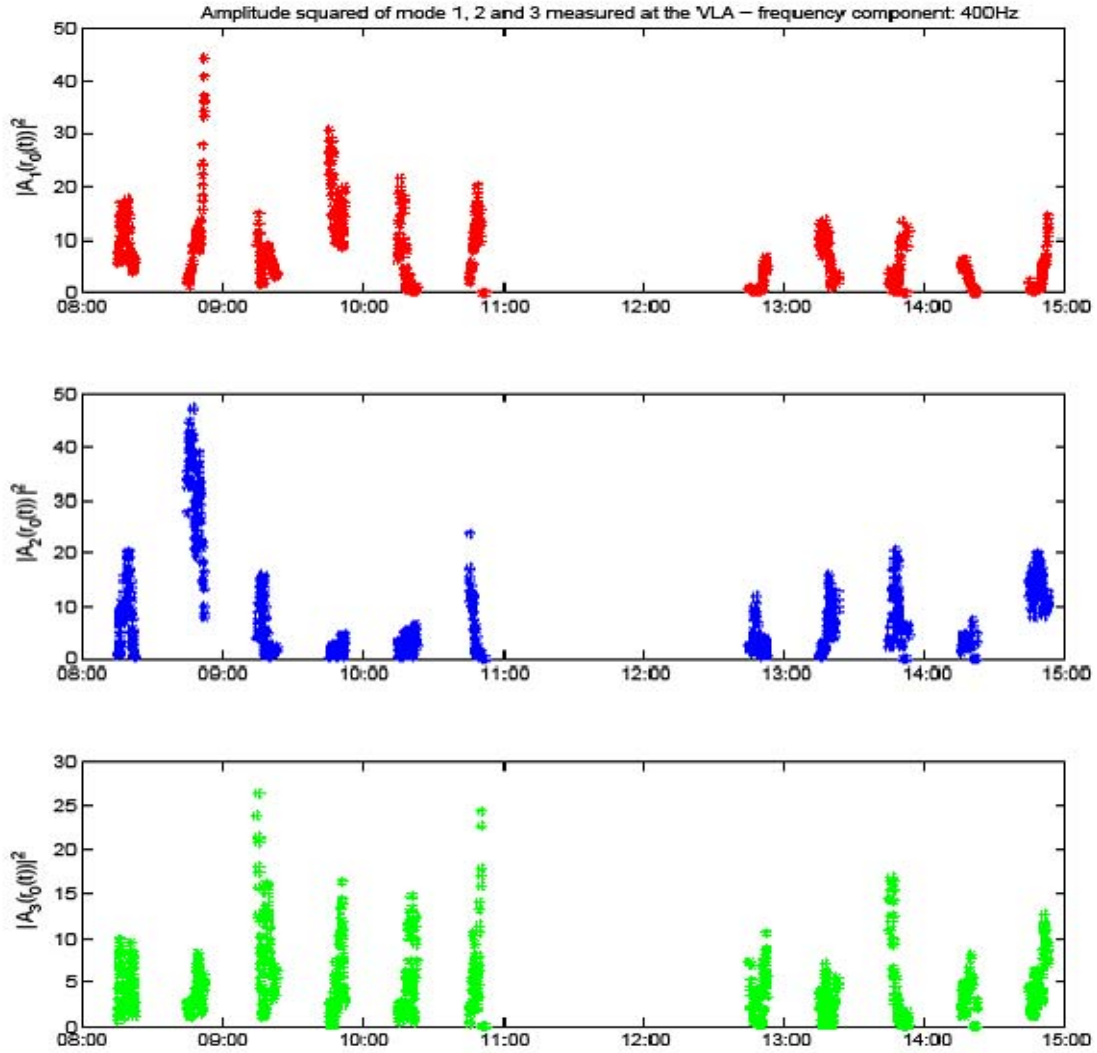
Figure 16.   Same as Figure 14 for a signal observed between 0700 GMT and 1500GMT on May 6, 2001.

Besides the exchanges of energy between modes, the variability of the signal also signifies the presence of solitons along the acoustic path. In fact, some evidence of variability is clearly observable on May 7, during the so-called quiet time, though the fluctuations measured on May 5 and May 6 are much faster. Indeed, as stated in chapter 1, non linear internal waves are not the only parameters which control the variability of the water column. In contrast, linear internal waves, as well as subtidal or tidal phenomena, occur simultaneously and are probably responsible for the changes in the mode energy for the third case study, on May 7.

33

The comparison between May 5 and May 6 also reveals some interesting features. Surprisingly, the presence of more than one soliton on the acoustical path does not seem to significantly affect the amplitude of the mode energy oscillations observed at the VLA. Compared with the soliton on May 5, the three ISWs on May 6 were also bigger. Based on the theoretical model presented in the predictions outlined in Chapter II, one could expect more dramatic effects in the presence of these solitons. However, it is probable that the presence of three solitons makes the constructive and destructive phases more complicated and may explain the previous result.
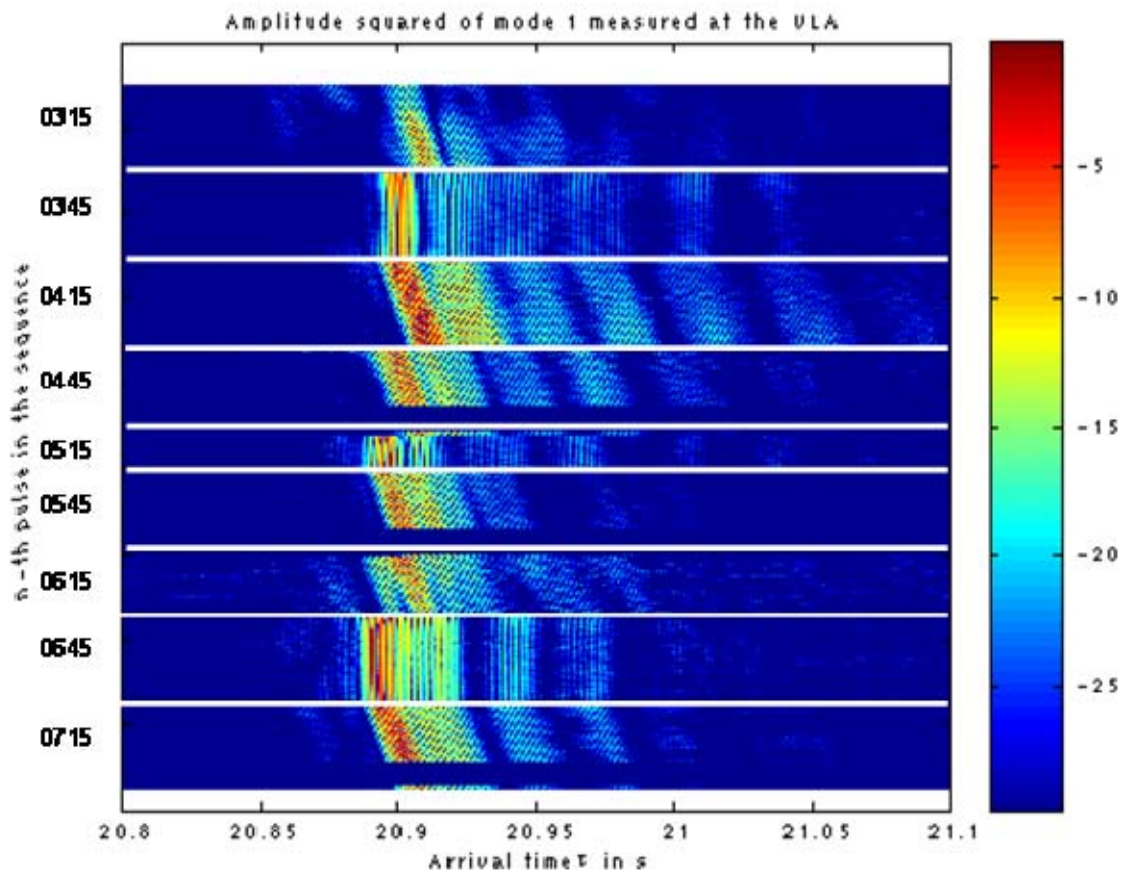
Figure 17.   Same as Figure 13 for a signal observed between 0315 GMT and 0715GMT on May 7, 2001.

Finally, from these few pictures it appears that non linear internal waves might be partly responsible for the time spreading of the signal. This theoretical model predicted a small amount of spreading caused by solitons, and most of the spreading could be

attributed to the presence of other phenomena, such as linear waves or mesoscale events; this point will be further developed later in this chapter.
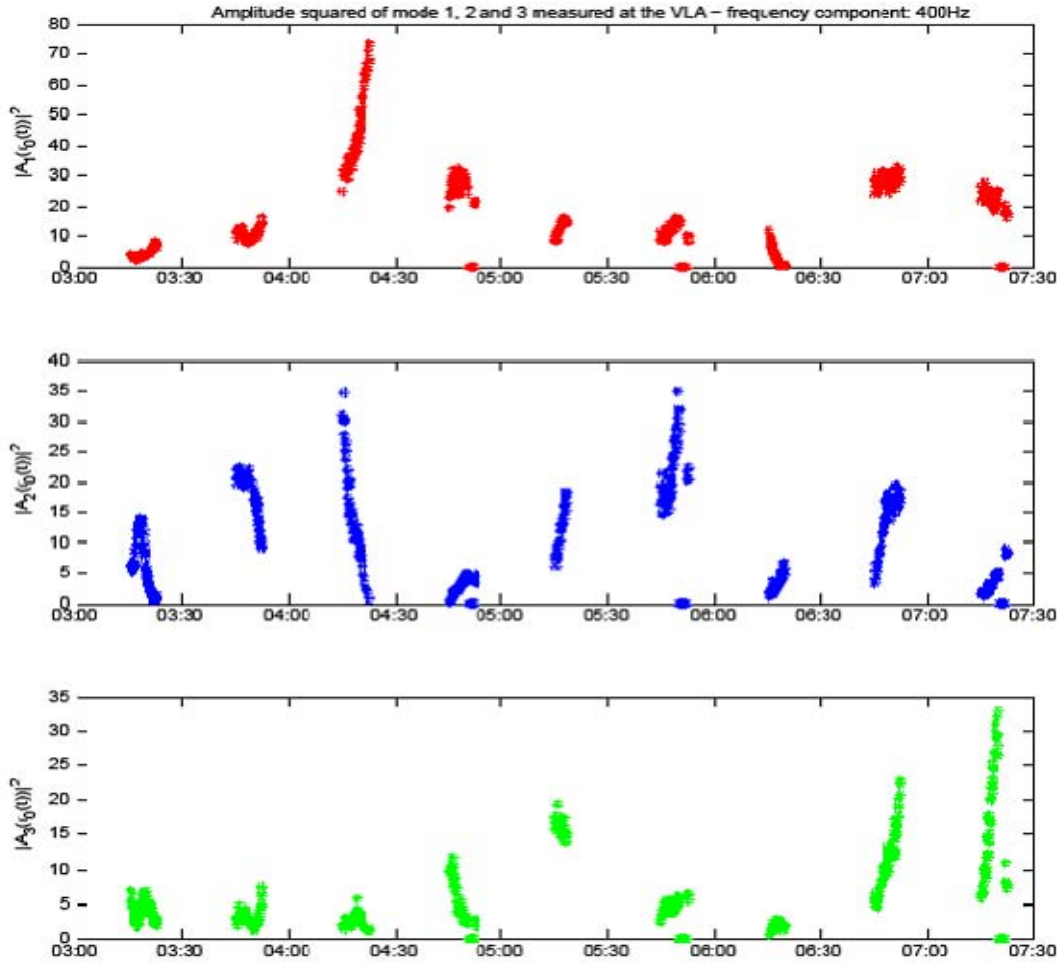
Figure 18.   Same as Figure 14 for a signal observed between 0315 GMT and 0715GMT on May 7, 2001.

B.   COMPARISON BETWEEN MODEL AND OBSERVATIONS: MODAL ENERGY VARIABILITY

As stated in the introductory chapter of this report, the goal of this project was to test the fast theoretical model designed by Colosi against the in-situ data presented in the previous section. The following results were evaluated from MATLAB based programs built upon this theory. The runs were conducted both on UNIX and Windows systems.

Before looking closely at the results, this section considers a few difficulties regarding the strengths and weaknesses of the comparison. First, as explained in chapter II, this model was designed for quick implementation, and many assumptions were made for this purpose, obviously decreasing the accuracy of the study's results when the mode coupling is strong. Secondly, as discussed earlier, this model neglects tidal and subtidal variabilities, as well as the effects caused by random linear internal waves, though these elements could significantly alter the observed acoustic signal (Chiu et al., 2004). Thirdly, data collection methods applied during this campaign of measurements did not perfectly match those required to exhaustively evaluate the model. For instance, the locations of the different oceanographic moorings made a few parameters, particularly ISW speed, very difficult to evaluate. This parameter is, however, essential in the evaluation of the characteristic half-width of the soliton and is a sensitive input for this model, as will be demonstrated later. Finally, bathymetric coupling can also influence the incidental mode amplitudes on the NLIWs and thus represent an additional complication.

For any of the three test case studies, this study conducted a direct comparison between the data and the model as illustrated in Figures 19, 21, 23, 25 and 27. In these figures, the 400Hz component of the mode energy received at the VLA is displayed with respect to the location of the soliton in the acoustic path. The modeled data in these figures are represented with blue lines and blue dots, while the observed data are in red. Significantly, in these five figures, like the observations, the model demonstrated fast changes in the predicted energy received at the array. Although these results were promising, a direct superposition of the observed data on top of the modeled data appeared difficult. Indeed, many of the statistical tools employed here are hypersensitive to slight changes in the inputs, such as the soliton speed, width or amplitude. Therefore, this study superposed only a couple of significant points over the simulated data for any sequence of 88 pulses. In addition to these points, which represent averages over the first and second parts of each sequence, errorbars encompass the extremes on both sides of the mean values. Finally, all the observed data were scaled with estimates of the unperturbed mode amplitude, evaluated from sections where there were no NLIWs. Figures 20, 22, 24, 26 and 28 are scatterplots that combine observed and modeled data. The value of the

36

correlation coefficient is indicated in the upper part of these figures in order to help us in assessing the quality of this model and the relevance of the comparison. These latter values were also compared to the sample error ε defined by $\varepsilon \approx \sqrt{2/n}$, where n represents the number of events accounted in the correlation calculation. Finally, the soliton amplitude, speed and width used as inputs for the runs are similar to the information presented in Chapter II.
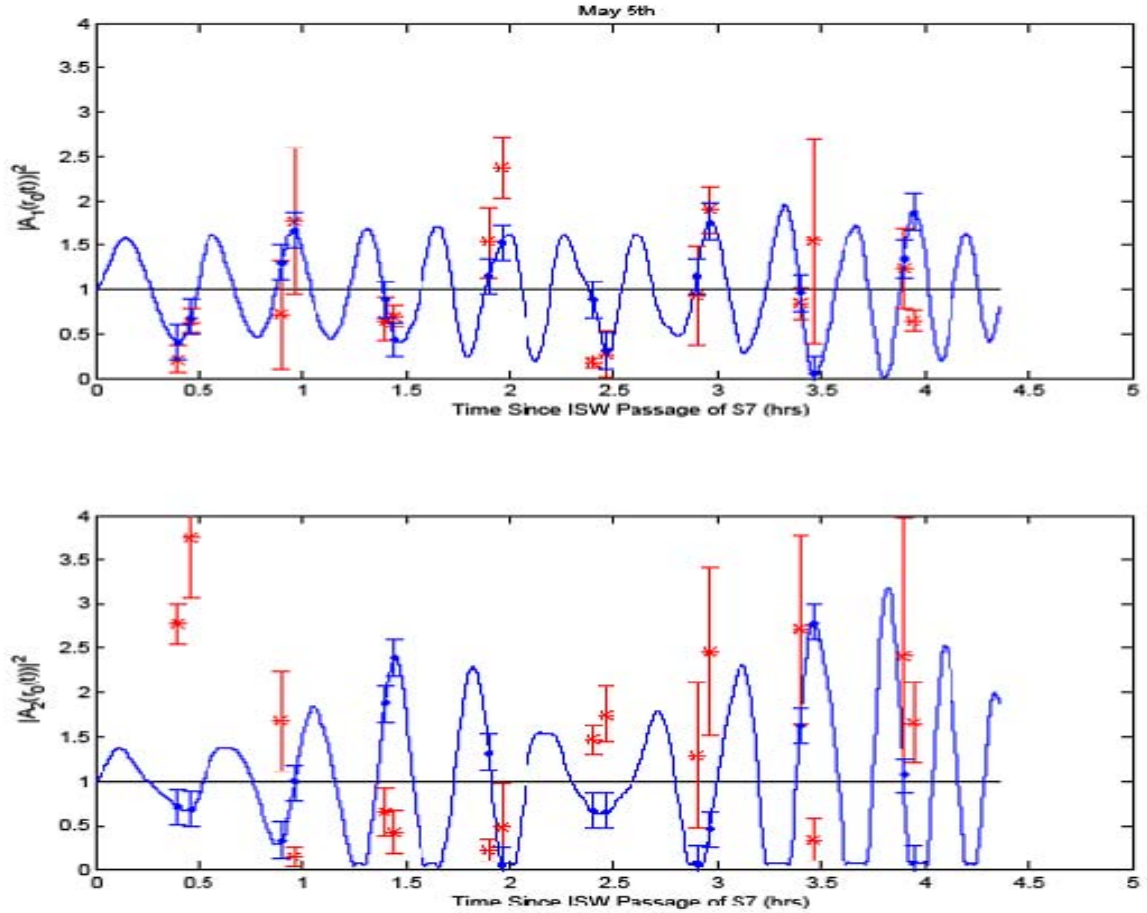
Figure 19. Relative mode energy fluctuation conveyed by the 400Hz carrier frequency and received at the array for mode 1 and mode 2 on May 5, 2001. The blue lines, dots and error bars represent the modeled data while the red dots and whiskers are the observed ones.
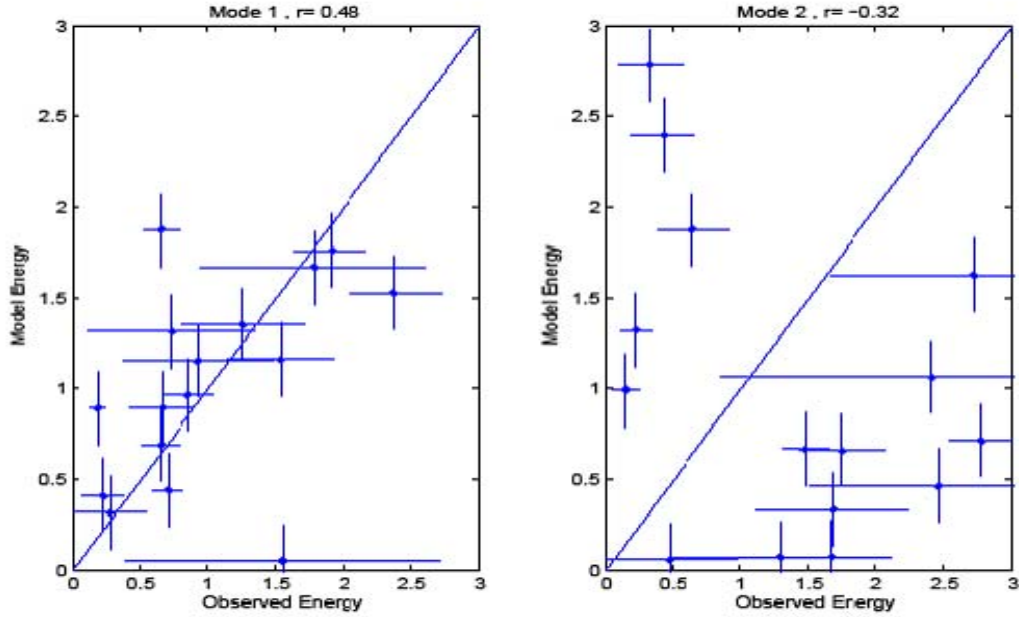
Figure 20.   Scatterplot comparing observed mode energy to modeled mode energy for mode 1 and 2 on May 5, 2001 for the 400Hz carrier frequency.

A few main results can be extracted from the figures above. First, as expected from the definition of the mode amplitude described by Equation 2.17, the simulation predicts huge oscillations of the mode energy. However, because of the changes in the bathymetry and in the shape of the soliton, these oscillations lack periodic consistency and show some variability as the soliton moves shoreward. While the model successfully predicts the mode energy variability for mode 1, its results are quite poor regarding mode 2.

Obviously, the results are not perfect, and the correlation coefficient is just a little better than the sample error, $\varepsilon \approx 0.35$. Nevertheless, as illustrated in the scatterplot, almost all the points are in the neighborhood of the slope 1 line, and the correlation coefficient is decreased by a few outliers. For mode 2, it seems difficult for the model to predict the right energy, as illustrated in Figure 20. Figure 19 suggests that the model is able to track the tendency of the energy changes, but the continual presence of time leads and lags makes the statistical results quite poor. Many factors could explain these differences between mode 1 and higher order modes, particularly the fact that this model uses a weak, single scattering approximation which may no longer hold for modes higher

than one. Moreover, random linear internal waves, the complex bathymetry or other kinds of variability can induce mode coupling, and are thought to affect these higher modes more.

Finally, the model appears to generate better results in the first part of the plot when the soliton has not yet reached the sharp continental shelf between S5 and S4. This result could have been anticipated, since the model does not take into account the non linear interactions of the soliton with the bottom.
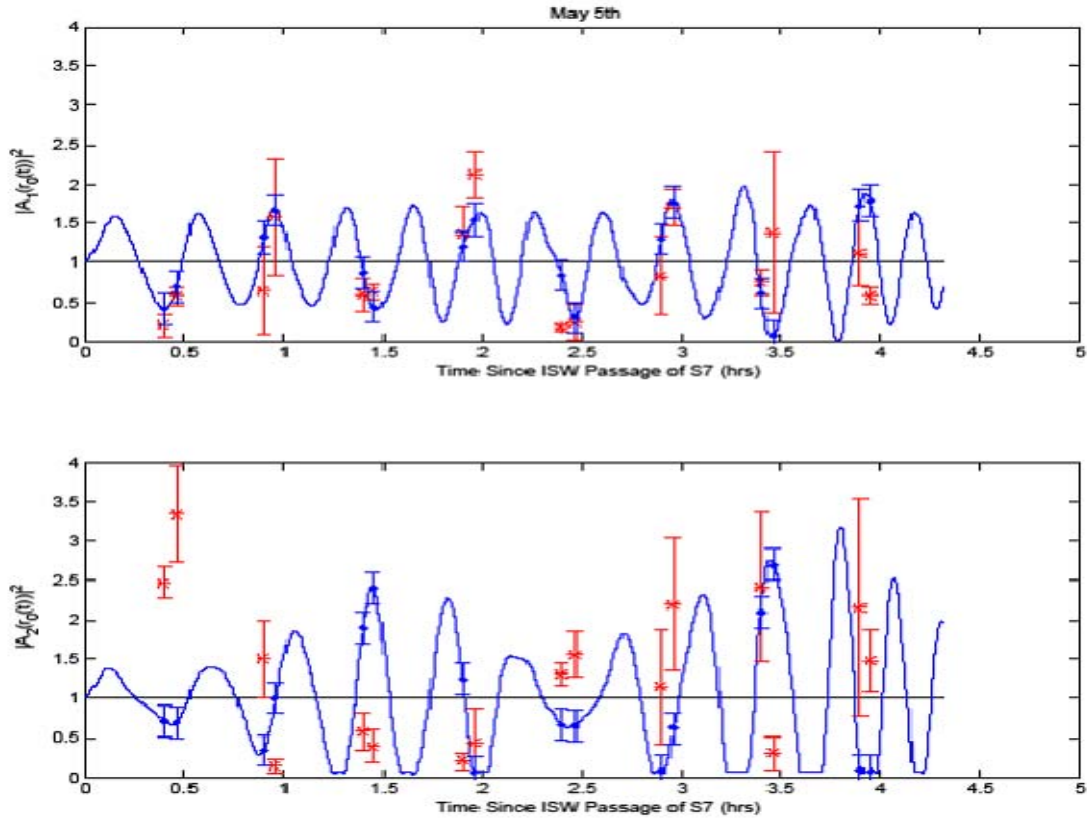
Figure 21.   Same as Figure 19 for the 395Hz carrier frequency.

This study gauged the ability of this model to predict not only the energy conveyed by the main carrier frequency, but any component of the 100Hz-bandwidth pulse. To this end, this study conducted the same kind of analysis for two other frequencies, namely 395Hz and 405Hz, which also carry a lot of energy. Figures 21, 22, 23 and 24 present these results, which bear similarities to those observed for 400Hz. The fourth section of this chapter explores the sensitivity of the model regarding frequency.

39
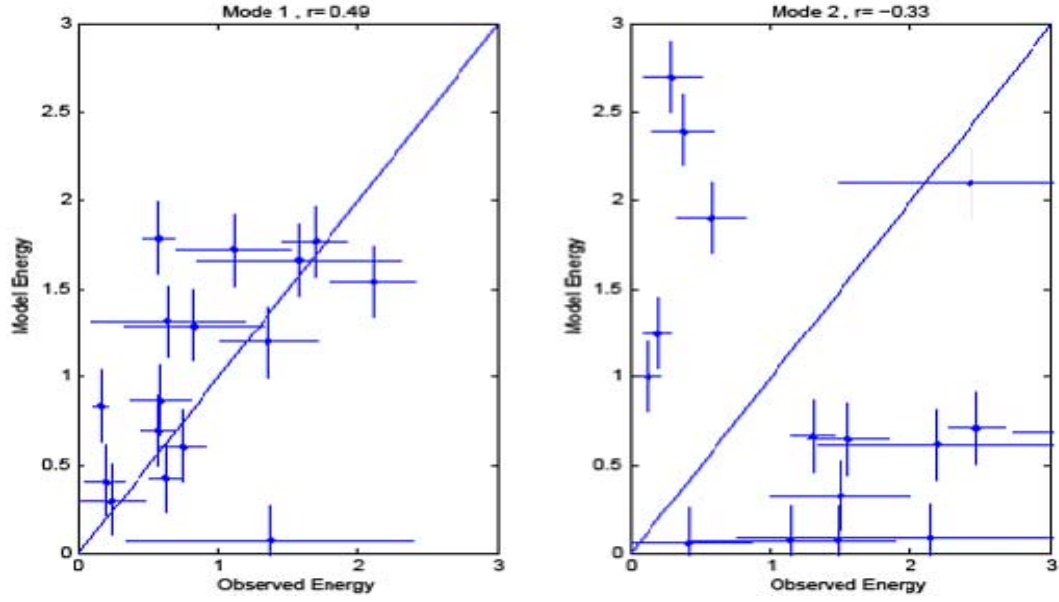
Figure 22.　Same as Figure 20 for the 395Hz carrier frequency.
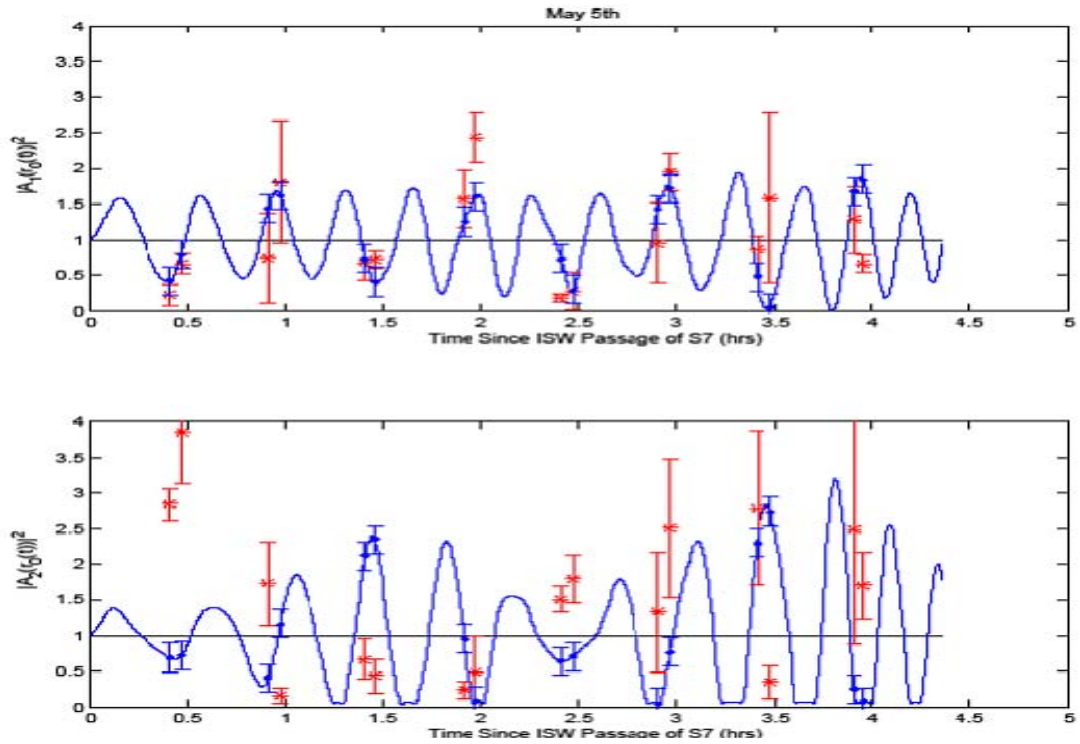
Figure 23.　Same as Figure 19 for the 405Hz carrier frequency.
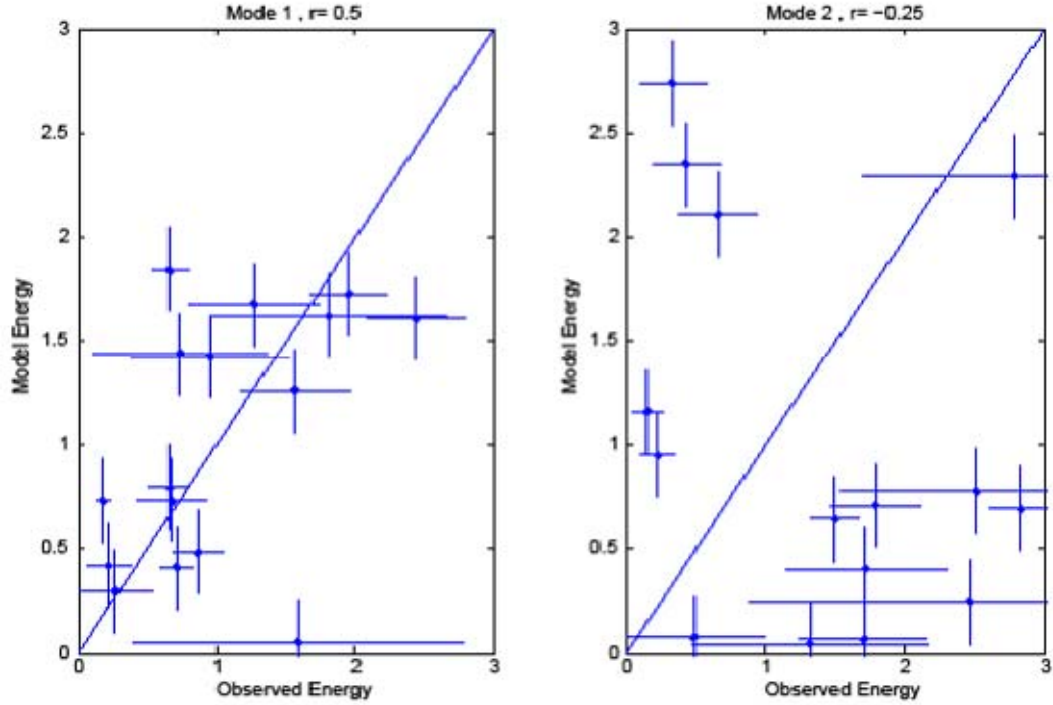
Figure 24. Same as Figure 20 for the 405Hz carrier frequency.

After testing the model's energy predictions, the same kind of analysis was conducted for May 6 as a series of three solitons propagated along the acoustic path. Technical failures prevented proper collection of acoustic data during the whole period of time, so only a few points were available for this analysis. However, in this case, which used only ten points to evaluate the results, the correlation coefficients are even higher. Then, the expected value for the sample error is given by $\varepsilon \approx \sqrt{2/n} = 0.45$. These values confidently suggest that the model's results are relevant, and that there is a significant difference between results between modes 1 and 2. Moreover, the fact that the coefficient correlation reached a value close to 0.8 in the second case study is very promising for the model. Because three large solitons were observed along the acoustic path in this case, it is likely that their influence on the water column variability is much bigger than for the first case study and largely overcomes the relative influence of other environmental variability.
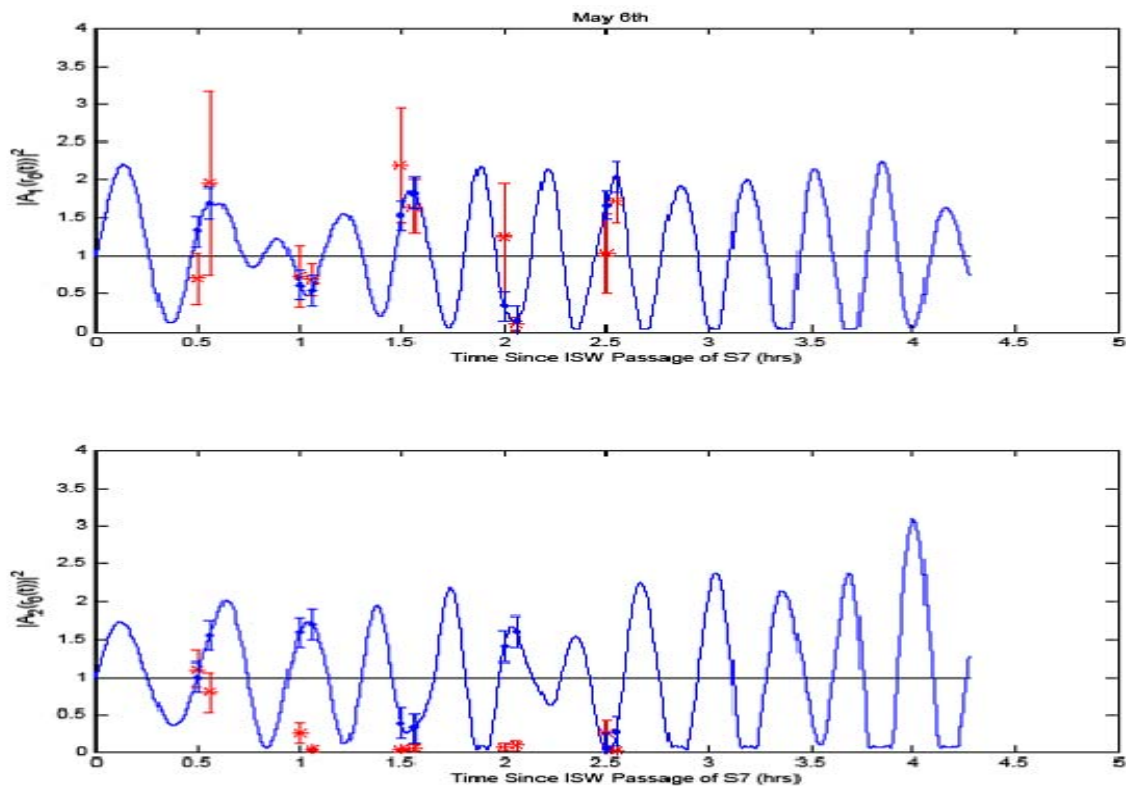
Figure 25.   Same as Figure 19 on May 6, 2001. A series of three huge solitons was observed along the acoustic path.
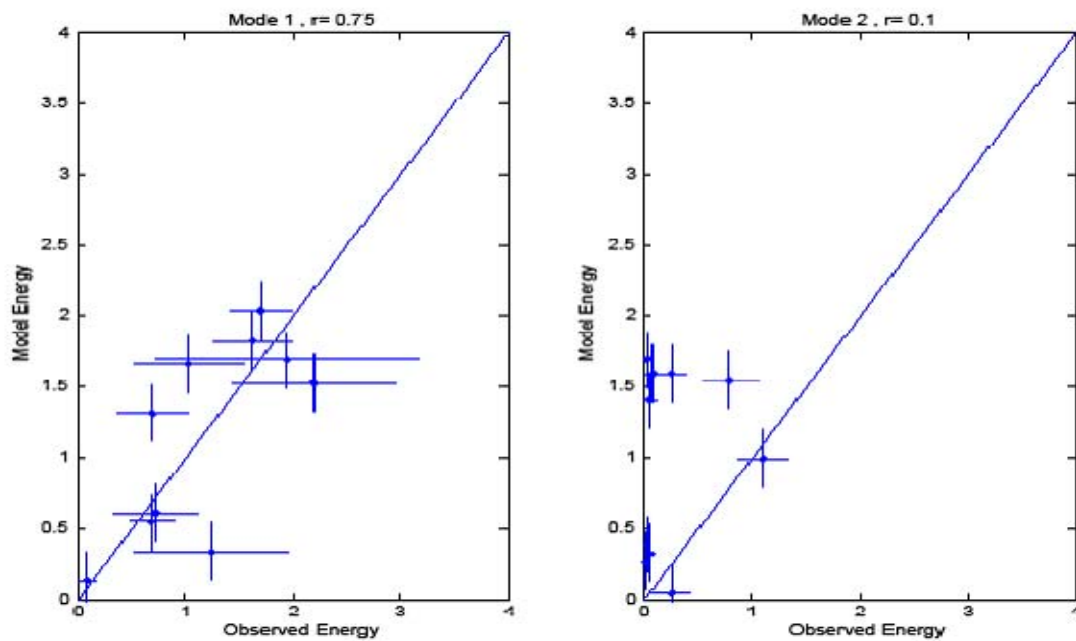
Figure 26.   Same as Figure 20 on May 6, 2001.

C. COMPARISON BETWEEN MODEL AND OBSERVATIONS: TIME SPREADING

Part of the effects caused by the solitons on the signals observed at the array was related to energy fluctuations arising from mode coupling, as demonstrated earlier. Looking at Figures 13, 15 and 17, it is nevertheless notable that the signal shows significant time spread in the presence of solitons relative to the case without ISWs. In fact, mode coupling is known to act on modal phase as well as modal amplitudes. The current section focuses on this aspect of the interactions between solitary internal waves and sound propagation. Then, the time spreading observed in the in-situ data were compared against the simulated results. Two main variables were used to estimate the spreading: the time lagged-intensity covariance of the signal and the travel time fluctuation. The first variable more adequately characterizes the spreading, which affects in-situ data, and is described by the following equation:

$$\Im_n(\tau') = \left\langle \int_{-\infty}^{\infty} I_n(\tau + \tau').I_n(\tau)d\tau \right\rangle \text{ where } I_n(\tau) = \left| A_n(\tau) \right|^2 . \tag{3.2}$$

Regarding the spreading predicted by the model, chapter II demonstrates that the mode amplitude phase fluctuation is frequency dependent and given by:

$$\delta\theta_n(R) = Arg([A_n(0) - i.\sqrt{\pi}.\sum_{j=1}^{N_s}\sum_{m=1}^{N}(\frac{k_m}{k_n})^{1/2}.A_m(0).C_{mn}(j).\Delta(j).\exp[-\frac{k_{mn}^2.\Delta^2(j)}{4}].e^{i.k_{mn}.r_0(j)}]) . \tag{3.3}$$

Then, the travel time fluctuation of the mode is given by:

$$\delta\tau = \frac{d(\delta\theta_n(R))}{d\omega} . \tag{3.4}$$

If the phase $\delta\theta_n$ varies linearly across the bandwidth of the signal, the pulse does not spread, but is only advanced or delayed. This advance or delay is termed a travel time bias, τ_1.
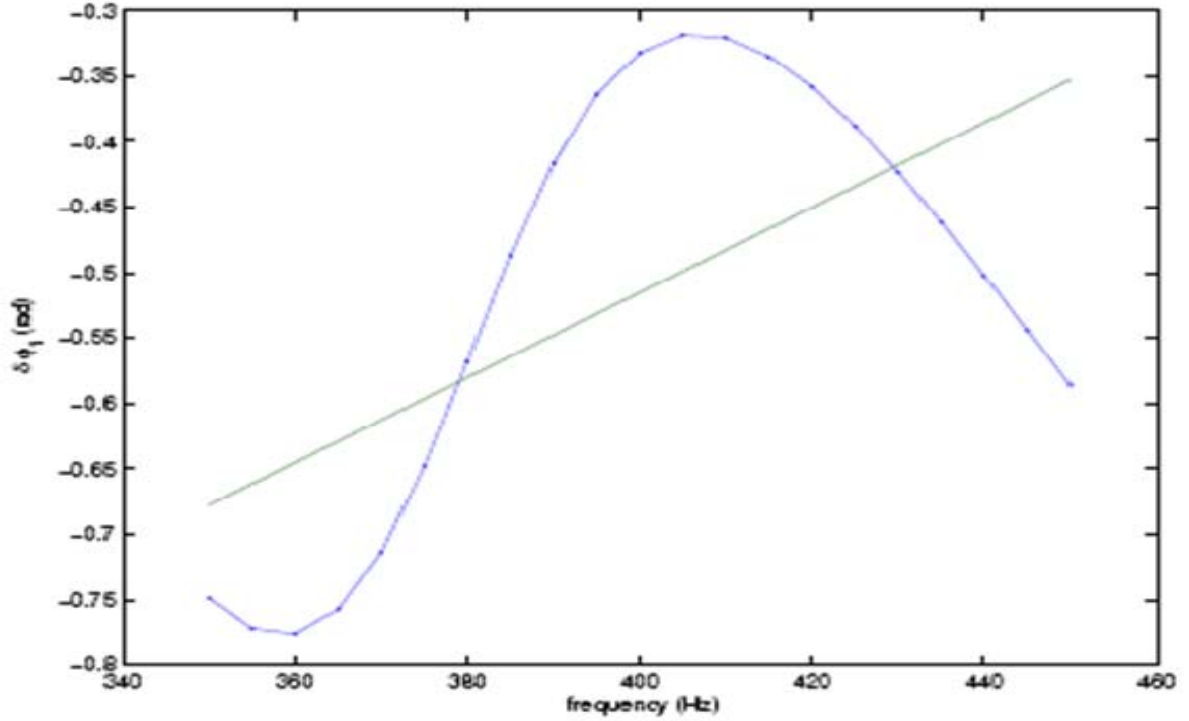
Figure 27.   Simulated phase across the 350 to 450 Hz bandwidth on May 5, 2001. The soliton is located 30km away from the source. The linear fit to the phase is shown in green.

However, if the phase variation is non-linear, then dispersion or time spreading occurs. Figure 27 shows an example of the phase variation across the frequency band 350 to 450Hz for the simulations on May 5; clearly, both modal bias and spreading are occurring. The modal time bias is qualified τ_1 by fitting a line through the phases $\delta\theta_n$, and the bias thus becomes the slope of this linear fit. To quantify the spread, one subtracts from the linear fit, forming a detrended phase function $\delta\hat{\theta}_n$, which is then used in Equation 3.4 to compute time fluctuation as a function of frequency. The pulse spread, which is also the root mean square variation of τ across the bandwidth, can be expressed by:

$$\tau_0 = \sqrt{\left\langle \tau^2(\omega) \right\rangle}\Big|_\omega . \tag{3.5}$$

Figure 28 shows the estimates of the bias and spread as a function of the ISW position r_0. What is first evident is that the bias and spread increase when the non linear

44

wave is more distant from the source. This is understandable, since the modes propagate at different speeds, and thus accumulate larger time differences at larger ranges. The time fluctuation of a mode will be greatest if the observed energy in that mode travels as much of the source receiver distance as other modes and only couples near the receiver. The modulation of the bias by the beat wavenumber resonance is also notable. Depending on the relative phase of the modes at the ISW location r_0, the bias can be either positive or negative. Additionally, the bias and spread represent significant fractions of the 400Hz period (2.5 ms), so that these corrections could be very important for time coherent processing. Further remarkable are results from simulated data based on soliton characteristics from May 6, as shown in Figures 29 and 30. Clearly, these last two figures, particularly the values of the spread, suggest that the signal would experience less spread as a result of many large solitons rather than a single isolated one.
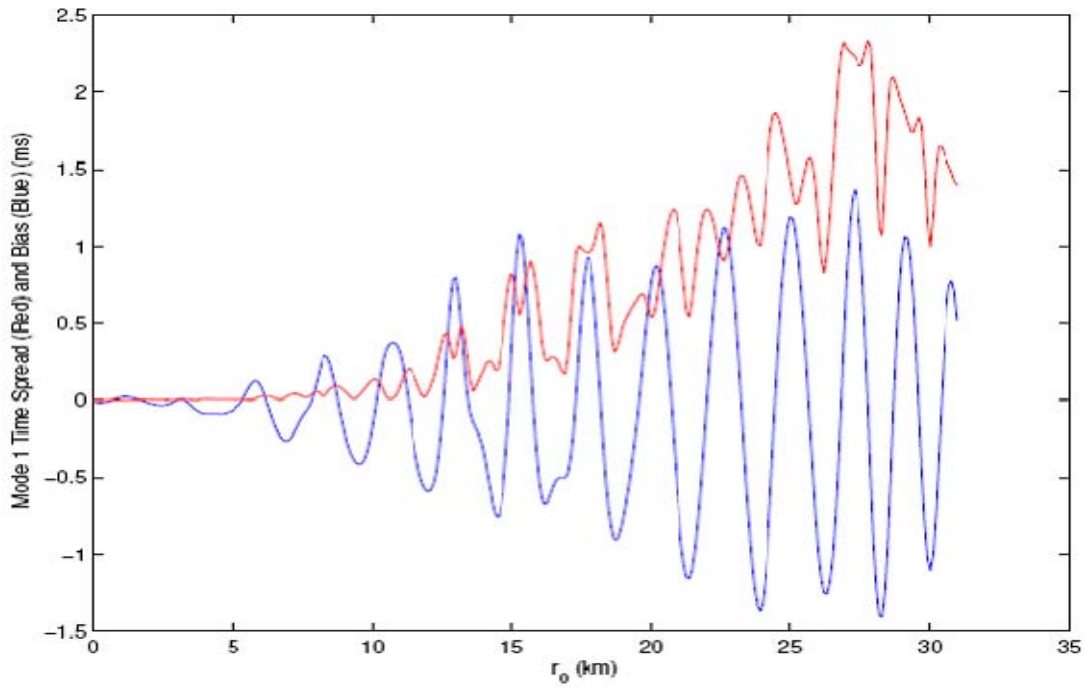
Figure 28.   Mode 1 pulse bias and spread on May 5 as a function of the distance from the source, r_0.
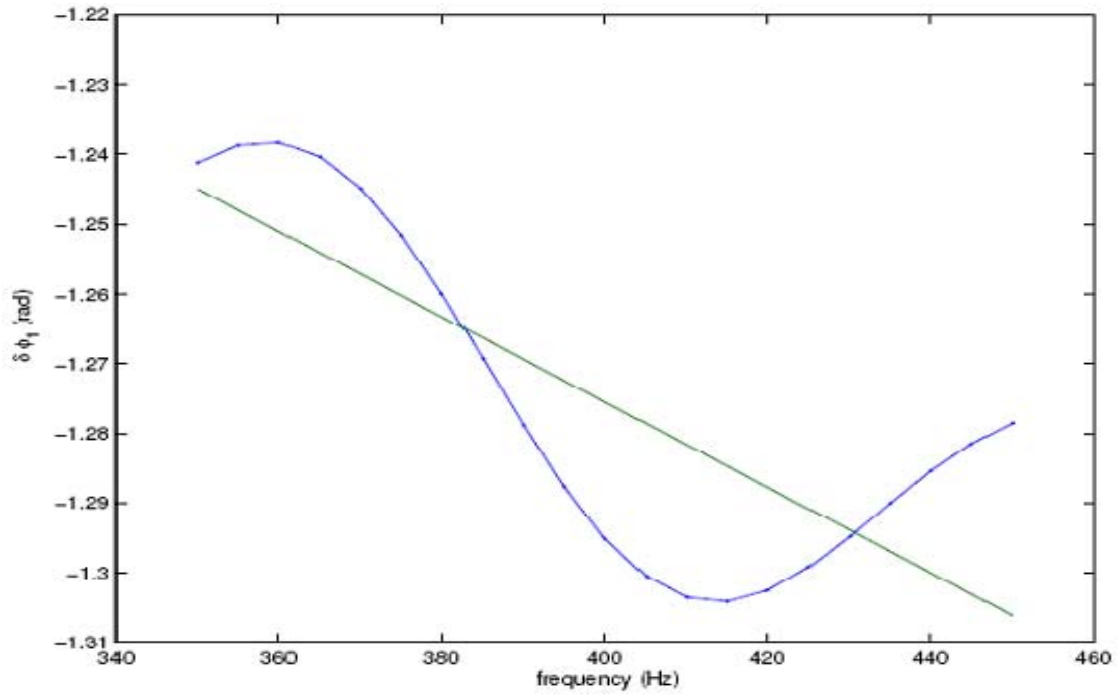
Figure 29.   Same as Figure 27 for May 6.
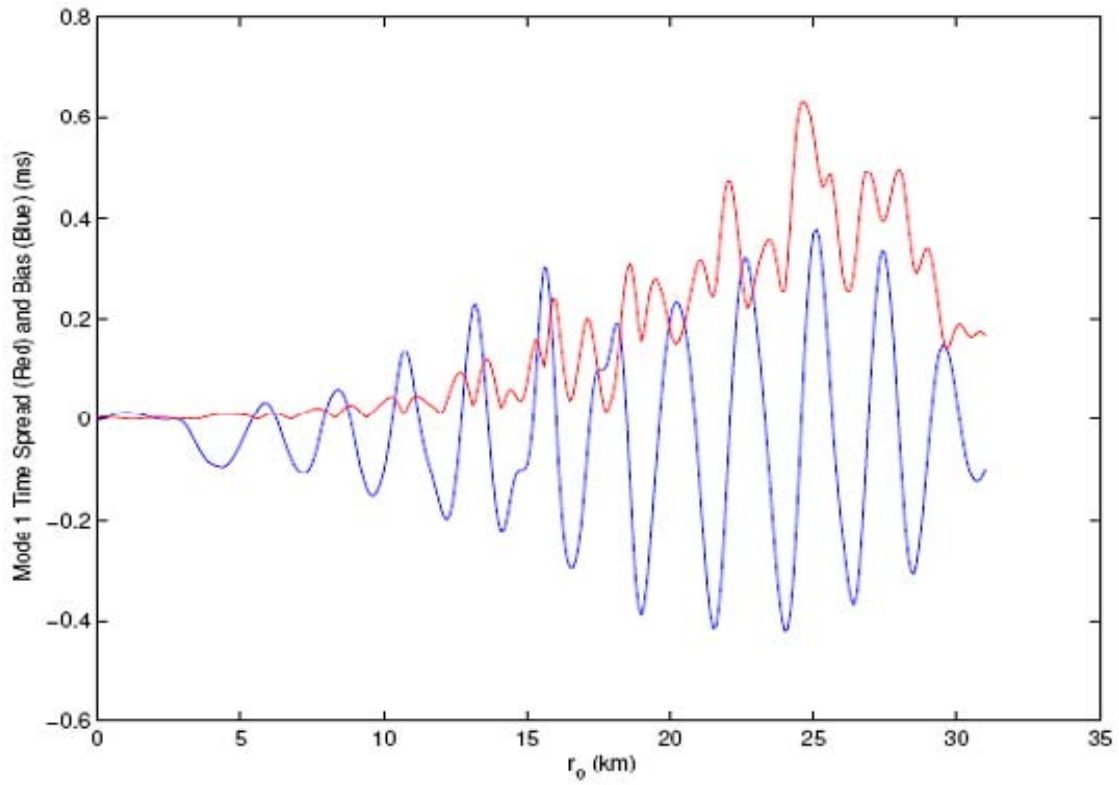
Figure 30.   Same as Figure 27 for May 6.

46

As illustrated in Figure 31, and as predicted by the model, the observed spreading is quite noticeable for the case studies and more dramatic on May 5 than on May 6. The model also predicted a larger spread of the signal as the NLIW neared the array. This result was unfortunately not truly observable from the data, as illustrated in Figures 32 and 33. Finally, it is significant that this spreading caused by the ISW is relatively small, less than 3 ms, and does not explain all the distortion in Figures 13 and 15.

Figure 31 displays the time lagged-intensity covariance of the signal observed for the three case studies and focuses on the comparison between these three days for mode 1 and mode 2. Figures 32 and 33 more carefully detail the evolution of the spreading with time. Indeed, in these figures, the case study is separated in two halves (1st part and 2nd part) to track the evolutions caused by the propagation of the soliton. The first part (red curves) represents the energy observed when the soliton was more than 15 km from the array; the second part (green curves) characterizes the period when the soliton was less than 15 km from the array. Finally, the variables σ_0, σ_{15} and σ_{16} characterize the e-folding of the covariance for the three case studies and are known to characterize the spreading. In Table 1, the spreadings observed on May 5 and 6 are represented by σ_{sp5} and σ_{sp6}, defined by:

$$\sigma_{sp5}^2 = \sigma_{15}^2 - \sigma_0^2 \text{ and } \sigma_{sp6}^2 = \sigma_{16}^2 - \sigma_0^2.$$

Table 1.   Covariance σ_0, σ_{sp5} and σ_{sp6}.

	May 7, 2001 - σ_0	May 5, 2001 - σ_{sp5}	May 6, 2001 - σ_{sp6}
Mode 1	6.1 ms	10.7 ms	6.1 ms
Mode 2	6.4 ms	10.5 ms	5.0 ms
Mode 3	6.5 ms	10.2 ms	3.9 ms
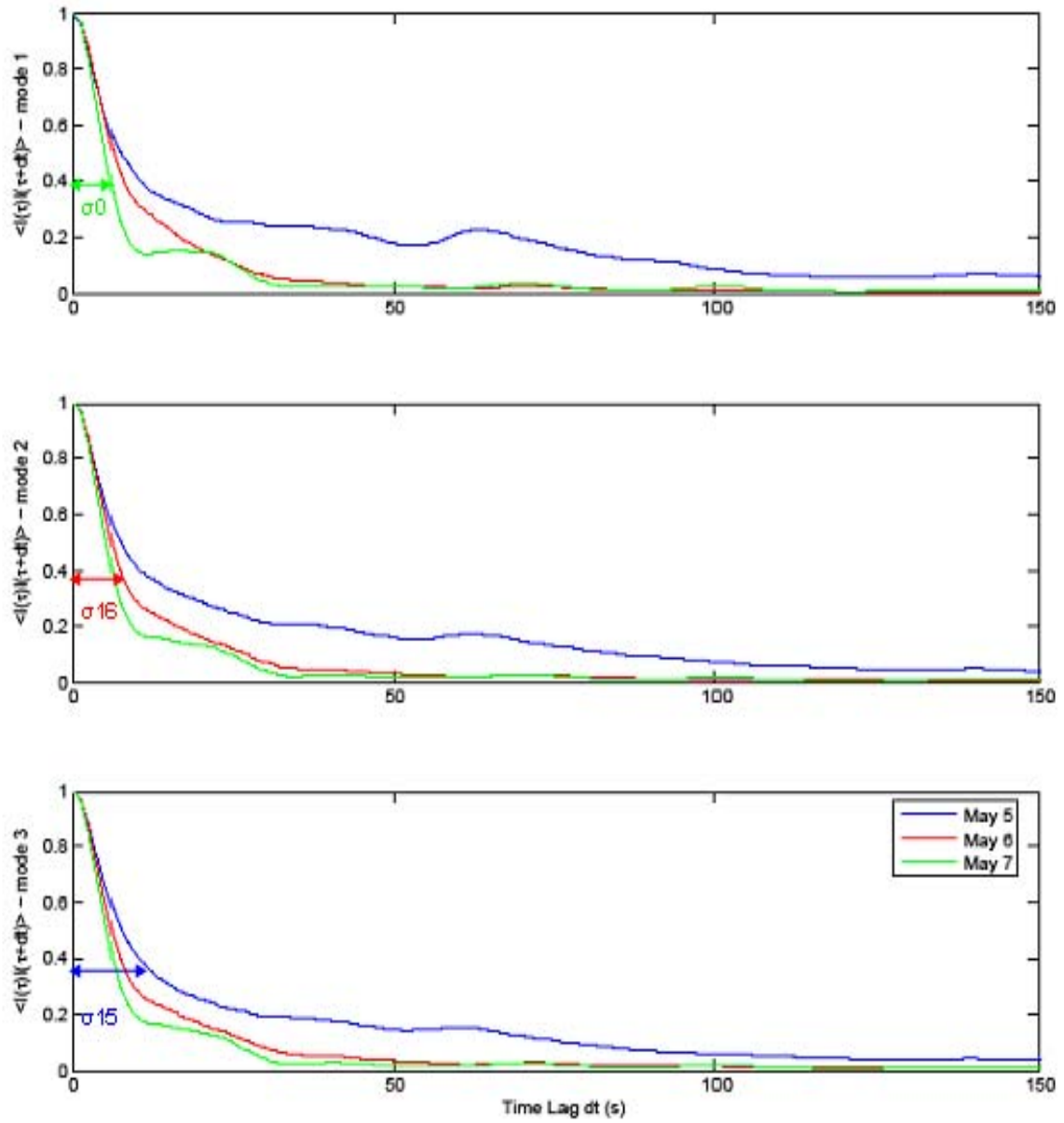
Figure 31.   Time lagged-intensity covariance of the signal on May 5, 6 and 7, 2001.

As evident in Figure 33, the analysis was unable to observe any difference between the first part of the path and the second part, as expected from the modeled spreading, despite the presence of a soliton in the acoustic path. Moreover, the observed spreading was definitely larger than the modeled. From these observations, spreading caused by the ISW appears to be much less important than the spreading caused by other environmental variability, particularly the random linear internal waves.
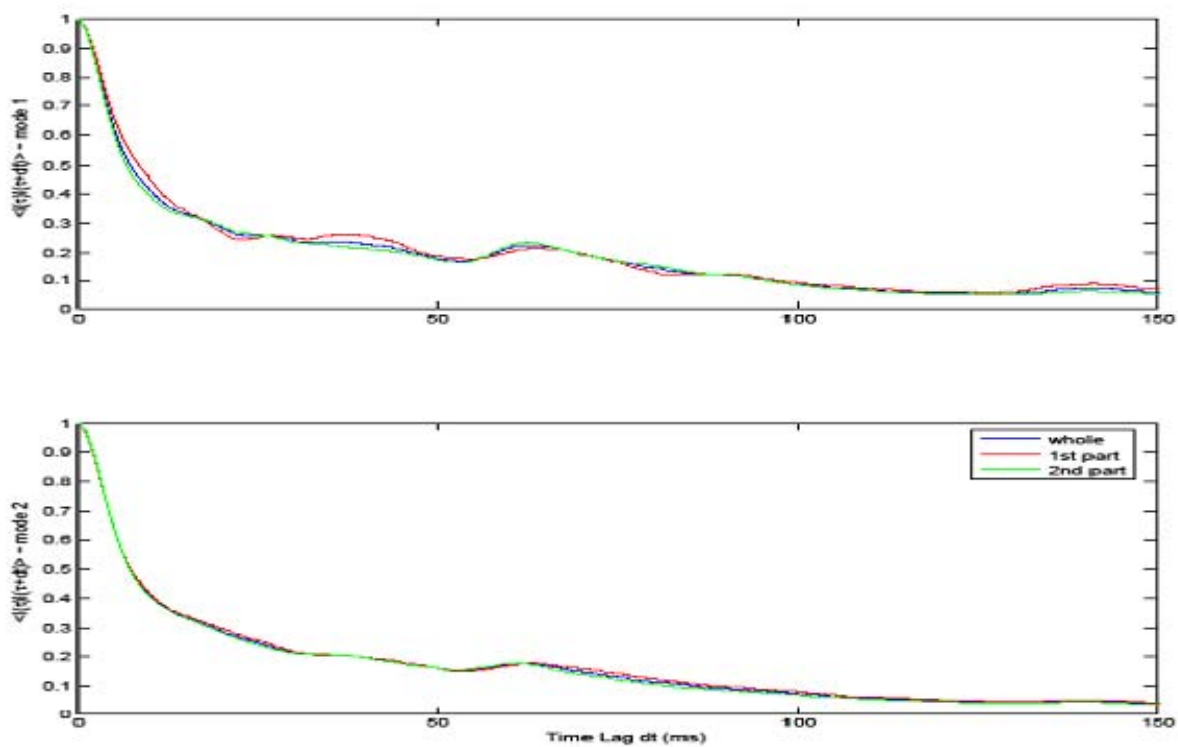
Figure 32.   Time lagged-intensity covariance of the signal on May 7, 2001 for mode 1 and mode 2.
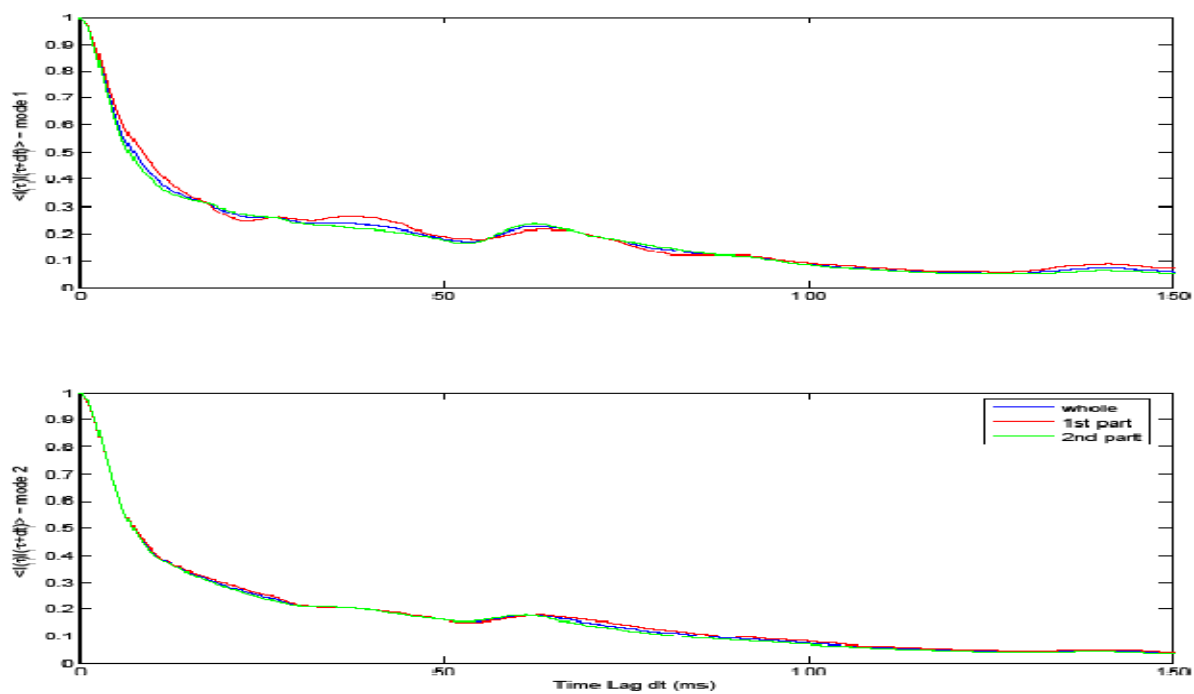
Figure 33.   Same as Figure 32 on May 5, 2001.

49

D. SENSITIVITY OF THE MODEL

The last step in the evaluation of the model was to test its sensitivity against some of its inputs, namely the propagation speed of the soliton, its amplitude and width and a few frequencies within the bandwidth.

As the environmental conditions, such as the temperature, salinity and density, were quite similar during the setting of the solitons on May 5 and 6, 2001, the model was able to investigate the relative influence of the number of solitons, their amplitude and width by just looking at the simulation for these two days. The propagation speed was also assumed to be identical in the following comparison.
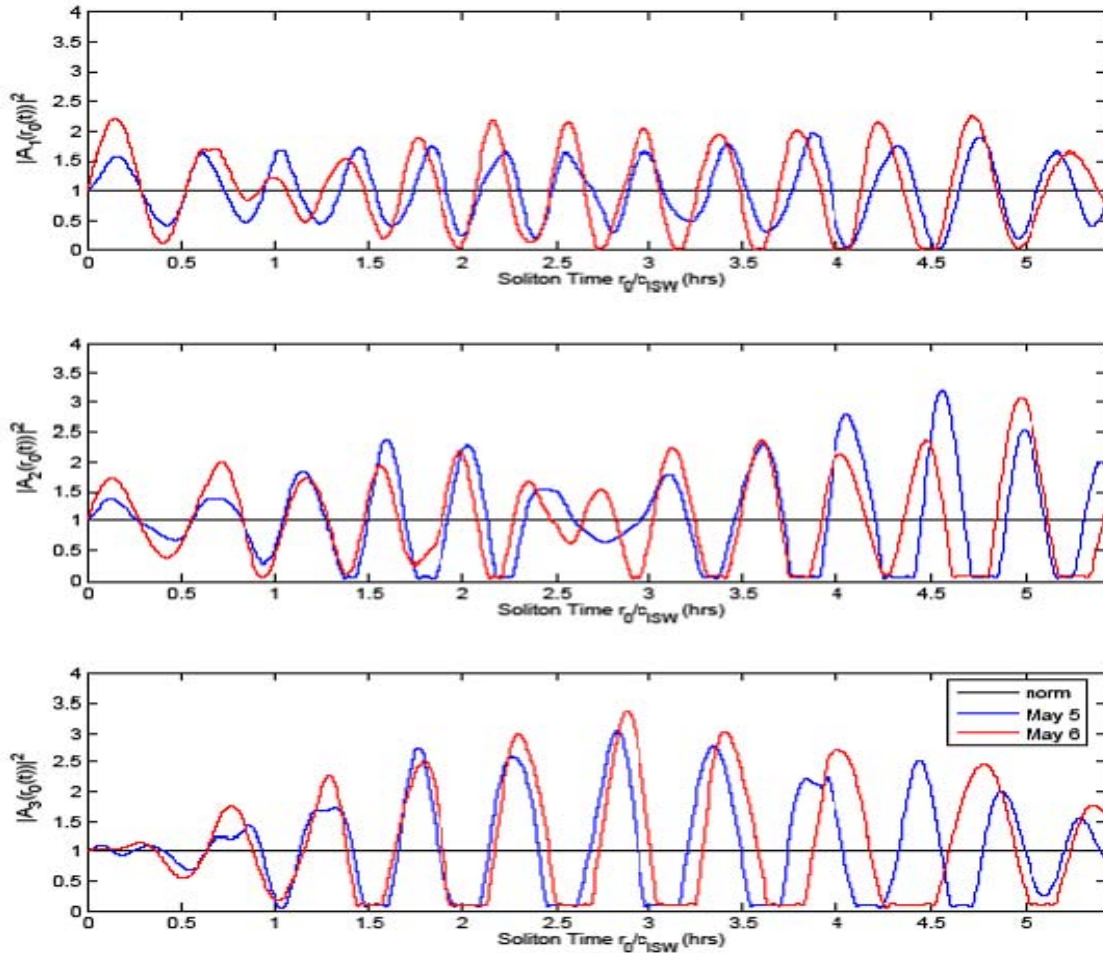
Figure 34.   Simulated modal energy received at the VLA on May 5 and 6, 2001.

Clearly, any of the three solitons observed on May 6, 2001, was bigger than the soliton reported on May 5, 2001. In fact, the amplitude of the soliton does not change the whole shape of the energy variation; in contrast, the amplitude tends to magnify the existing variations, as illustrated in Figure 34. The addition of multiple waves tends to create some constructive and destructive effects in the simulation, which may explain the observed lags and leads between the two simulations.
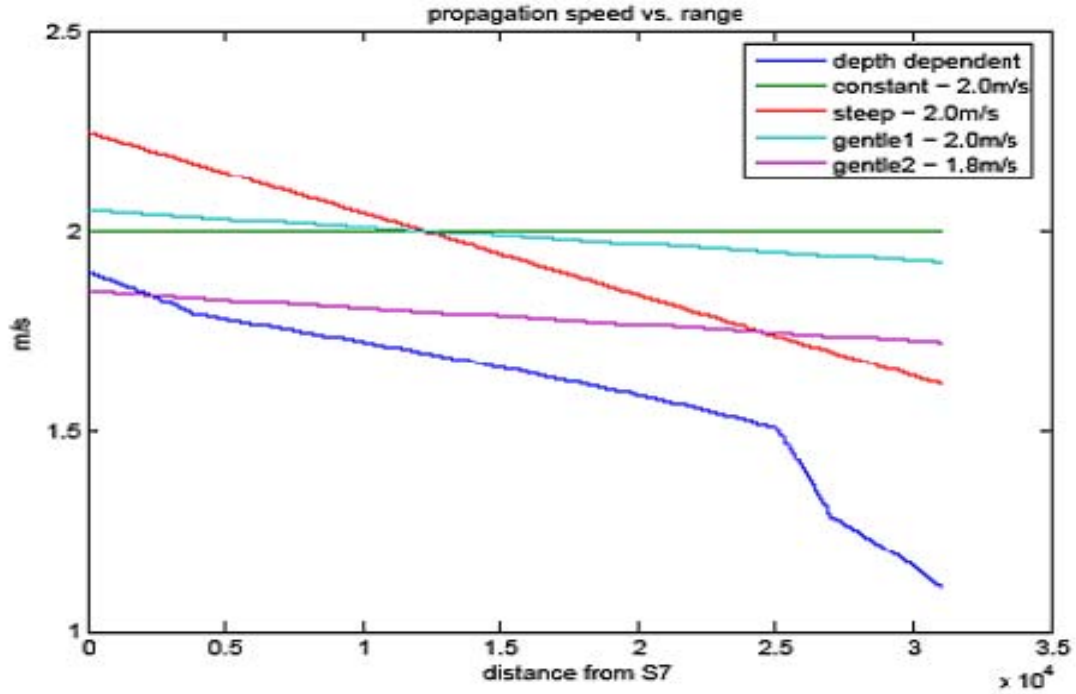
Figure 35.   Five different ISW speed profiles between moorings S7 and S5.

This section also examined the propagation velocity of the soliton. Actually, during the numerous tests conducted for this project, the model/data comparison was highly sensitive to this variable. The ISW speed was also a critical factor since it was difficult to pinpoint accurately. Indeed, the only available and appropriate data were the currents at moorings S4, S5 and S7, the temperature measurements at these same locations, which revealed the signature of the soliton, and a few SAR images, which indicated the direction of propagation itself. From these different observations, the actual speed of the soliton could be deduced, followed by the speed of the soliton as it is seen across the acoustic path. This latter speed proved to be slightly bigger since the

propagation of the soliton and the acoustic path had different orientations. Then, different speeds were simulated, as illustrated in Figure 35, and the model was run for any of these five simulations.
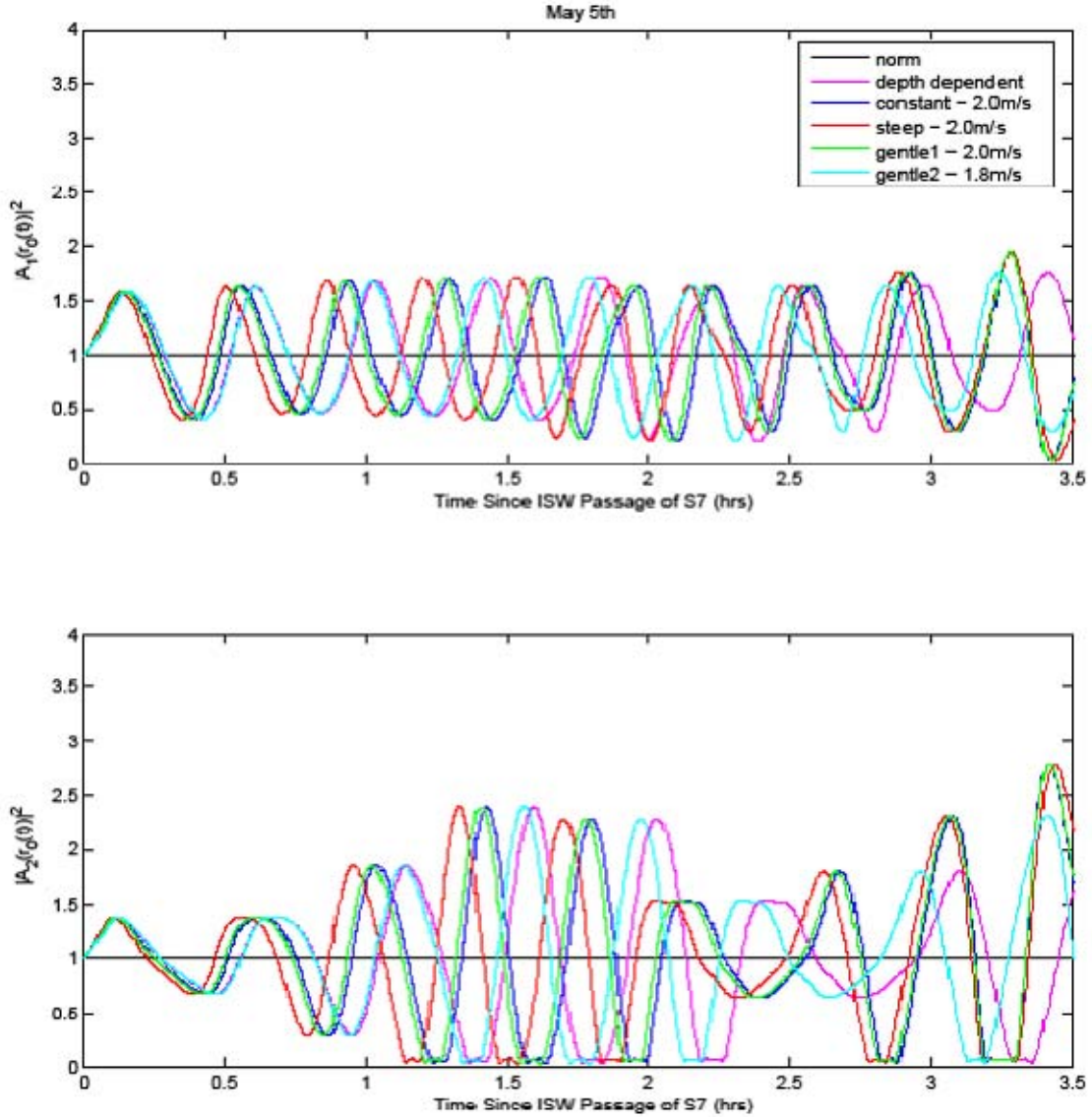
Figure 36.   Simulated fluctuations of the 400Hz component of the mode energy for mode 1 (upper panel) and mode 2 (lower panel) as a function of the propagation of an ISW in the acoustic path for 5 different ISW speed profiles.

These examples were used to test three linearly decreasing speed profiles associated with the motion of the soliton from S7 to S5, two possessing gentle slopes and one with a steep slope. This work also simulated a constant speed profile and a depth-

dependent profile that agreed with the linear wave theory in shallow waters. As demonstrated in Figure 36, the differences between the five runs are dramatic, and both the average speed over the path and the slope seem to be important.
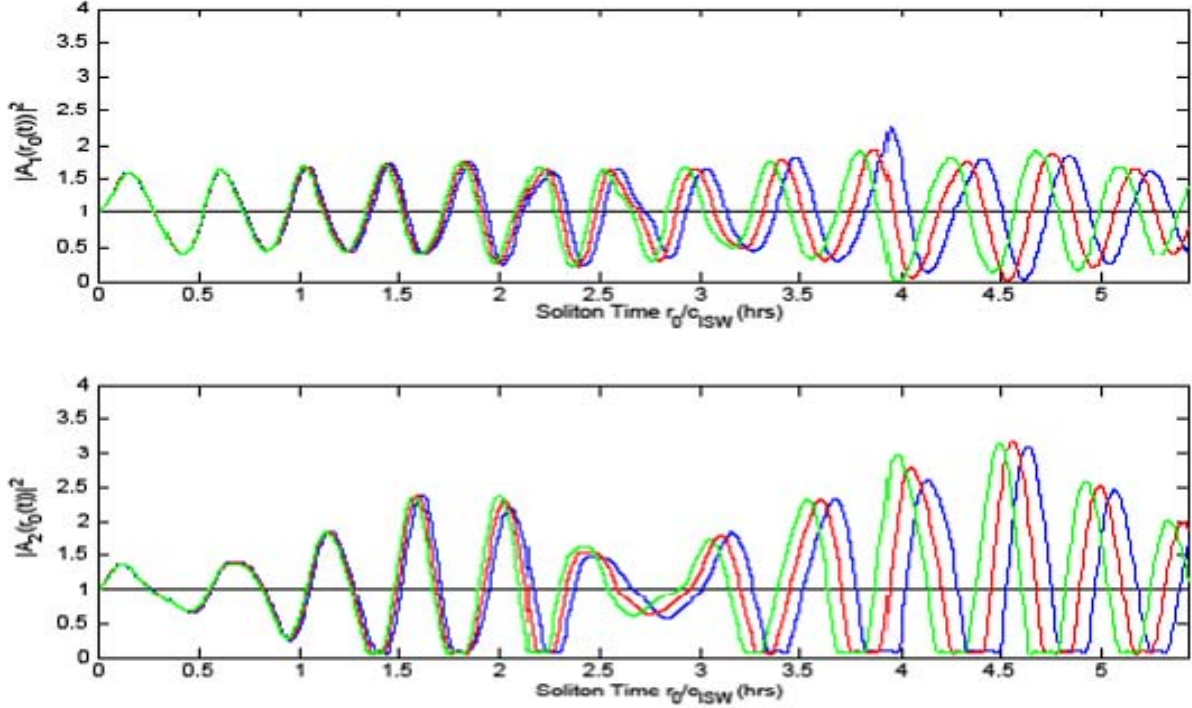
Figure 37.   Simulated fluctuations of the mode energy for mode 1 (upper panel) and mode 2 (lower panel) as a function of the propagation of an ISW in the acoustic path for three different frequency components of the signal: 375Hz, 400Hz and 425Hz.

The last variable in the critical analysis of the model was its frequency dependence. As illustrated in Figure 37, and earlier in Figures 21 to 24, the results were conclusive. Furthermore, the model itself proved greatly promising, as it was able to predict the energy variations for any frequency component of the signal.

E.   DISCUSSION AND COMMENTS

Despite the difficulties in extracting the appropriate data for the 2001 Asian experiment, the model proved highly adept at predicting the energy variations when a few solitons came into the acoustic path. This was particularly true for mode 1, which was the easiest one to resolve with the available vertical array. The results observed for mode 2

and for any higher mode did not meet the study's expectations; as stated earlier, many explanations could be offered to explain this unforeseen result. For one, coupling effects and scattering effects are much more complex for these higher modes, which are also probably more sensitive to fluctuations caused by linear internal waves, the bathymetry or other environmental variability.

Regarding the time spreading, the modeled data did not agree with the observed data, and once again these differences are most likely the result of influences by other kinds of environmental variability.

Finally, despite the vast amount of data collected during ASIAEX 2001, this study did not collect adequate ISW speed profiles; unfortunately, this data is essential to run the model. Thus, with more constraining data, the results from the model could have been different. Future runs of the same kind of comparison should consider working a shorter range for the acoustic path and a simpler bathymetry, which would suppress some undesirable variability and coupling.

IV.   DETECTION OF NON LINEAR INTERNAL WAVES BY SYNTHETIC APERTURE RADARS

Internal waves are one of the first ocean phenomena detected on synthetic aperture radar (SAR) images, where they appear as a sequence of bright and dark quasi-parallel lines. This result was early described by Alpers (1985), Apel et al. (1979). Based on the quality of these pictures, very promising results are consistently observed from SAR satellites. In order to understand the strength of these systems in characterizing solitons, this next section provides a review of some central concepts concerning SAR images. Following that is a review of the basic theory supporting the detection of solitons by SAR systems. Finally, the study presents an elegant theory by Zheng et al. (2001) that proposed two simple ways of retrieving the characteristic width and amplitude of the non linear internal waves. The following chapter determines the relevance of the theory by testing it against in-situ data for different environments. This analysis gives particular attention to wind effects.

A.   SYNTHETIC APERTURE RADARS AND OCEANIC PURPOSES

Synthetic aperture radars were developed in the 1970s in order to improve the spatial resolution offers by real aperture radars. The first satellite to carry a SAR system was SEASAT (1978), which provided very promising results regarding wind retrieval, detection of oceanic features such as oil slicks and non linear internal waves and ship tracking. These abilities are particularly important because clouds are transparent for radar satellites and radar information can be retrieved either by day or by night. Moreover, radars are active systems and allow advanced data processing for finer resolution. Finally, as their temporal and spatial coverage and storage capacities improve in the future (RADARSAT 2 vs. RADARSAT 1), they will become more and more applicable.

From real aperture radar physics, it is known that for a specific frequency f (or wavelength λ) and a slant range R , the azimuth resolution is entirely dependent on the

aperture length L_a. However, for the altitude at which satellite imaging sensors operate, engineering difficulties hamper achievement of L_a/λ values greater than several hundreds, this value being inversely proportional to the azimuth resolution. Through the use of synthetic aperture radars, however, 10 meter-resolutions can be achieved. In the 1950s, it was realized that the Doppler spread of the echo signal could be used to synthesize a much longer aperture so as to greatly improve the resolution of side-looking radars. It is beyond the scope of this chapter to consider all the applications and theoretical concerns behind SAR images; this chapter will focus only on the theory that supports soliton detection by SAR images. Table 2 summarizes the characteristics of the main SAR systems.

Table 2.   Characteristics of the main SAR systems. After Olmsted (1993).

	Mission		
Orbit	ERS-1	JERS-1	Radarsat
Altitude	785 km	568 km	793-821 km
Inclination	98.516°	97.662°	98.594°
Period	6027.907 s	5799.72 s	6042 s
Repeat Cycle	3, (35, 176) days	44 days	24 days
Orbit Type	sun synchronous	sun synchronous	sun synchronous
Ground Track Velocity	6.628 km/s	6.883 km/s	6.576 km/s
Instrument			
Frequency	C-Band (5.3 GHz)	L-Band (1.275 GHz)	C-Band (5.3 GHz)
Wavelength	5.66 cm	23.5 cm	5.66 cm
Pulse Repeition Freq.	1640–1720 Hz	1505.8–1606 Hz	1270–1390 Hz
Pulse Length (BW)	37.1 µs (15.5 MHz)	35 µs (15 MHz)	42 µs (11.6,17.3,30 MHz)
Polarization	VV	HH	HH
Antenna Size L × W	10 X 1 m	11.9 X 2.4 m	15 X 1.5 m
Peak Power	4.8 kW	1.3 kW	5 kW
Average Power	300 W	71 W	300 W
Noise Equivalent σ_0	-18 dB	-20.5 dB	-21 dB
Image			
Swath Width	100 km	75 km	50,100,150,500 km
Max Resolution Rg × Az	12.5 X 12.5 m	7 X 7 m	10 X 10 m
Resolution @ # looks	30 @ 4	18 @ 3	28 X 30 @ 4
System			
On Board Storage	None	Tape 20 min	2 Tapes @ 14.5 min
Look Angle	Right 20.355°	Right 35.21°	R & L 20–50°
Incidence Angles, Mid	19.35–26.50°, 23°	36.14–41.51°, 38.91°	22.64–59.56°, 45.12°
Footprint Rg × Az	80 X 4.8 km	70 X 14 km	50-150 X 4.3 km
Doppler BW	1260 Hz	1157 Hz	939 Hz
Coherent Integ Time	.6 s	1.7 s	.46 s
Windowing	Hamming	Hamming	Hamming
Pulse Compression Ratio	580:1	525:1	491, 727, 1260:1
Range Sample Rate	18.96 MHz	17.1 MHz	12.9, 18.5, 32.3 MHz
Maximum Data Rate	105 Mb/s	30 Mb X 2 Mb/s	105 Mb/s
Quantization	5 bits/sample	3 bits/sample	4 bits/sample

For a homogenous medium with a slightly rough surface and an intermediate incident angle, generally between 20° and 70°, the scattering from the surface can be described using the Bragg model. The Bragg scattering theory and its domain of applicability are described comprehensively in Plant (1990), and only the most important results for this project will be presented here. This theory states that any section of that surface wave spectrum resonates with the incident wave in producing strong backscattering. The Bragg resonance condition is also given by: $\frac{2L}{\lambda}.\sin\theta = n$ where L is the ocean wavelength, λ is the radar wavelength and θ represents the incident angle associated with the satellite system and $n = 1, 2, ...$

Radar images are also considered to be two-dimensional representations of the intensity of radar return signals. If one assumes that the radar receiving system is a perfectly linear system, the intensity of radar return signals should depend linearly on the roughness of the target surface, which is quantified by the backscatter cross section per unit area. For an ocean surface, Plant derived an expression for the normalized radar cross section of a slightly rough surface, σ_0:

$$\sigma_0(\theta)_{ij} = 16.\pi.k_0^2.\left|g_{ij}(\theta)\right|^2.\Psi(0, 2k_0 \sin\theta_0), \tag{4.1}$$

where k_0 is the wavenumber of the electromagnetic signal. $\Psi(0, 2k_0 \sin\theta_0)$ is the two-dimensional variance spectrum of surface displacement evaluated for the wavevector $(k_x = 0, k_y = 2k_0.\sin\theta_0)$. The axes of reference are relative to the viewing direction of the satellite, the x-axis being parallel to the track of the satellite. In other words, the backscatter is caused only by surface waves which lie within a restricted wavelength range and travel nearly toward or away from the antenna. It is further notable here that this expression breaks for steep waves. For this latter case, Plant (1990) proposed a much more complicated equation called the composite surface theory, which includes the mean surface slope and displacement. Finally, the indices ij denote the polarizations of the incident and backscattered radiation, and, if ε_r is the relative dielectric constant of seawater, $g_{ij}(\theta)$ is the first order scattering coefficients given by:

$$g_{HH}(\theta) = \frac{(\varepsilon_r - 1).\cos^2 \theta}{(\cos \theta + (\varepsilon_r - \sin^2 \theta)^{1/2})^2} \quad \text{for horizontal polarization and,}$$

$$g_{VV}(\theta) = \frac{(\varepsilon_r - 1).((\varepsilon_r.(1 + \sin^2 \theta) - \sin^2 \theta).\cos^2 \theta}{(\varepsilon_r.\cos \theta + (\varepsilon_r - \sin^2 \theta)^{1/2})^2} \quad \text{for vertical polarization.} \qquad (4.2)$$

Thus, this set of equations states that, for a given radar wave number k_0 and incident angle θ_0, the intensity of the radar return signals depends only on the two-dimensional wavenumber spectral density of the surface ocean wave field, Ψ. As indicated in Table 1, the Canadian SAR system RADARSAT, which is used in the analysis, is polarized horizontally.

B.   INTERACTION BETWEEN NON LINEAR INTERNAL WAVES AND SURFACE WIND WAVES.

Based on measurements by Zhang and Cox (1994), and the balance equation for the two-dimensional wavenumber spectral density of the surface ocean wave field, Zheng et al. (1994) proved that Ψ could be written:

$$\Psi = m_3^{-1}.(m.(\frac{u*}{c})^2 - 4\gamma.k^2.\omega^{-1} - S_{\alpha\beta}.\frac{\partial U_\beta}{\partial x_\alpha}.\omega^{-1}).k^{-4}. \qquad (4.3)$$

Even if this equation is quite coarse, the method is still elegant. Indeed, Zheng et al. (2001) retrieved Ψ from the principal of conservation of wave energy. Actually, the balance equation for the two-dimensional variance density spectrum of surface elevation can be written:

$$\frac{\partial \Psi}{\partial t} + (U + c_g).\nabla_h \Psi = S_{wd} + S_{nl} + S_{ds} + S_{cu}. \qquad (4.4)$$

In this equation, largely used in wave models, Ψ is calculated for any frequency f or wavenumber k and any direction φ. S_{wd}, S_{nl}, S_{ds} and S_{cu} represent the source terms for wind wave interaction, resonant wave-wave interactions, dissipation and wave current interactions. Assuming a steady state and using previously derived solutions for the source terms, Zheng et al., retrieved equation 4.3.

The coefficient m_3 originates from the wave-wave non linear term presented by McGoldrick (1965); this project does not directly use the coefficient and therefore will undertake no further investigation of it. The value of m was equal to 0.04, $u*$ is the friction velocity, γ is the viscosity of seawater ω is the dominant angular frequency of the surface waves. $S_{\alpha\beta}$ is the excess momentum flux tensor, U_β is the velocity component of the large scale current field , k is the observed wavenumber. The third term on the right side of equation (4.3) is given by:

$$S_{\alpha\beta}.\frac{\partial U_\beta}{\partial x_\alpha} = \frac{1}{2}(\frac{\partial u}{\partial x}.\cos^2 \phi + (\frac{\partial u}{\partial y} + \frac{\partial v}{\partial x}).\cos\phi.\sin\phi + \frac{\partial v}{\partial y}.\sin^2 \phi).$$ (4.5)

u and v were said to be the velocity components of the surface currents and ϕ is the wave direction. α and β are subscripts representing the horizontal axis of reference. This latter term, illustrated in Figure 38 and Figure 39, relates to the objectives of this theory and will be investigated more closely in the next section.

The manipulation of the previous equations requires careful handling of the different coordinate systems used by Zheng et al. Plant derived equation 4.1 using a coordinate system related to the viewing direction; equation 4.4 must be used in a Cartesian coordinate system associated with the cardinal directions. Finally, Zheng et al., used equation 4.5 in a coordinate system associated with the direction of the non-linear internal waves. Despite the confusion in the notations, the main ideas behind this theory offer valuable qualitative estimates of the influence of the different components on the backscattered energy. The section dedicated to the wind influences looks more closely at the definition of S_{wd}.

Because the spatial variability of the viscosity is small in the oceans (except in estuaries, coastal regions, polluted areas, and frontal zones), the contribution of the second term in equation 4.3 to a radar image can be considered as a constant. Obviously, the two other terms play key roles in generating an ocean radar image.
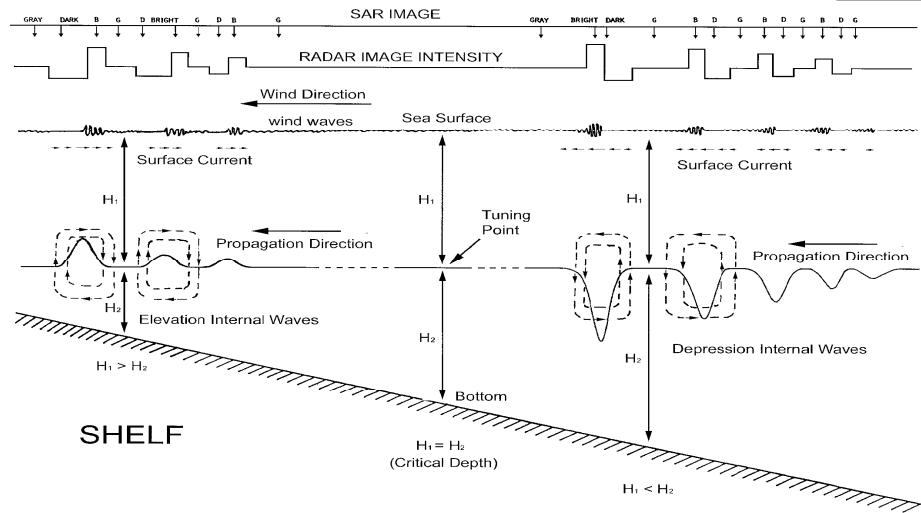
Figure 38.   Schematic of the interaction between non linear waves and surface wind waves and their effects on SAR images. After Hsu and Liu (2000).

It is significant here that equation 4.3 is based on the principal of conservation of wave energy and does not hold for rapidly changing wind conditions. Nor does it hold in very shallow waters, where dissipation or non linear interactions can be very important. Moreover, this equation was designed for gravity-capillary waves and a different equation should be used for capillary waves. However, regarding the wavelength of the most common SAR systems, such as ERS and RADARSAT, this equation is sufficiently accurate.
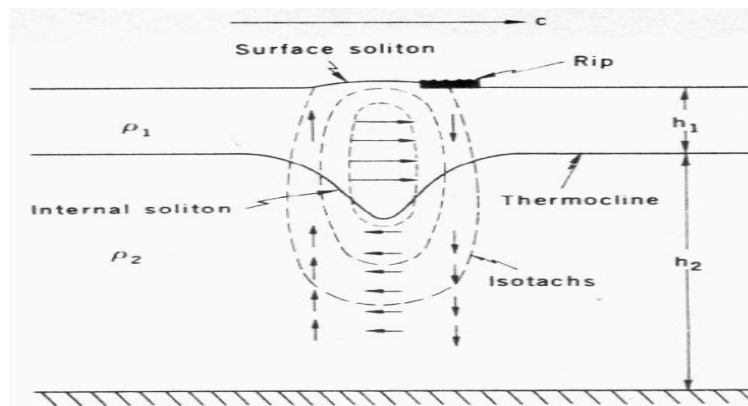
Figure 39.   Internal soliton in a two-layer fluid with finite depth. Dashed lines are isotachs of the water particle speed. Arrows indicate magnitude and direction of the water particle movement. After Osborne and Burch (1980).

C. DETERMINATION OF THE CHARACTERISTIC HALF WIDTH AND THE ASSOCIATED AMPLITUDE IN THE KORTEWEG AND DEVRIES MODEL

In their paper, Zheng et al. (2005) presented two methods based on the KdV equation. This section also summarizes their basic ideas, while the following chapter reports the results that were found using their techniques.

The first chapter of this report introduced the KdV equation for a two-layer model, and its solution was described by a secant function, such that:

$$\eta(x,t) = \eta_0 \sec h^2(\frac{x-Vt}{\Delta}) \tag{4.6}$$

where $\Delta = \sqrt{\frac{12\gamma}{\alpha.\eta_0}}$ is the characteristic width and $V = c_0 + \frac{\alpha.\eta_0}{3}$, the soliton velocity.

The first technique presented by Zheng et al., is based on the direct calculation of the interaction between the soliton and the surface waves. Then, using the previous definition of the depression in a barotropic two-layer model, one can deduce the velocity in the upper and lower layers, respectively u_1 and u_2, such that:

$$u_1(x,t) = (\frac{c_0.\eta_0}{h_1}).\sec h^2(\frac{x-V.t}{\Delta}),$$
$$u_2(x,t) = -(\frac{c_0.\eta_0}{h_2}).\sec h^2(\frac{x-V.t}{\Delta}). \tag{4.7}$$

One can then write that:

$$S_{\alpha\beta}.\frac{\partial U_\beta}{\partial x_\alpha} = -\frac{c_0.\eta_0.\cos^2\phi}{h_1.\Delta}.\tanh(\frac{x-V.t}{\Delta}).\sec h^2(\frac{x-V.t}{\Delta}). \tag{4.8}$$

Using equation 4.1 and 4.8, one derives an expression for the backscattered energy received by a satellite and caused by a soliton:

$$\sigma_{0.IW}(\theta)_{ij} = Q(k,g_{ij},\theta,\varphi,\delta).[\frac{c_0.\eta_0.\cos^2\phi}{h_1.\Delta}.\tanh(\frac{x-V.t}{\Delta}).\sec h^2(\frac{x-V.t}{\Delta}).\omega^{-1}] \tag{4.9}$$

$$\text{with } Q(k, g_{ij}, \theta, \varphi, \delta) = 16.\pi.k_0^2 . \left| g_{ij}(\theta) \right|^2 . m_3^{-1}.k^{-4}.f(\varphi, \delta). \qquad (4.10)$$

Essentially, this equation means that it is the alternating compressive and tensile effects of the internal wave currents that render them visible on the surface. Actually, the modification of surface wave spectrum by internal waves can be very significant, increasing the spectral level on the order of 200% (Apel, 2007). Moreover, for a SAR satellite, the frequency and the antenna polarization are fixed, and the incidence angle, the viewing direction, the propagation direction of the soliton and the dielectric constant change only a little within the range of an ocean internal wave packet. Therefore, Q can be treated approximately as a constant over the range of a soliton. Equation 4.10 is slightly different from that proposed by Zheng et al., and takes into account the looking direction of the satellite as well as the propagation direction of the non linear internal waves through the term $f(\varphi, \delta)$. If the latter need not be thoroughly evaluated in this theory, it is, however, essential to cover while looking at the wind effects.

In order to retrieve the characteristic half-width, one can use a normalized version of equation 4.9 and compare it to the normalized and centered SAR pixel values along a transect profile. A curve fitting method would also render the raw data smoother. Because SAR images inherently contain noise, this work relied on hand chosen pixels that characterize the soliton. They roughly represent the major features of the bright and dark lines associated with the soliton.

As the next chapter discusses, this method offers interesting results that can be altered by wind speed and direction. To overcome this difficulty, Zheng et al., introduced another method, which they called the peak-to-peak method. This method aims at retrieving the characteristic half-width by measuring the distance between successive maximum and minimum. Equation 4.9 proves the existence of these remarkable points, which are characterized by bright and dark lines on SAR images. Mathematically, these two points satisfy the following equation:

$$\left. \frac{\partial \sigma_{0.IW}}{\partial x} \right|_{\substack{x\max \\ x\min}} = 0 \qquad (4.11)$$

which is equivalent to:

$$\sec h^2(\frac{\frac{1}{2}d_{pp}-V.t}{\Delta})-2tgh^2(\frac{\frac{1}{2}d_{pp}-V.t}{\Delta})=0 \tag{4.12}$$

with d_{pp} being the distance between the maximum and the minimum.

Solving this equation, one obtains the following relationship between d_{pp} and Δ:

$$d_{pp}=2\ln(\frac{\sqrt{2}+\sqrt{6}}{2}).\Delta\approx1.32\Delta. \tag{4.13}$$

This demonstration, derived by Zheng et al., forms an essential foundation for understanding the whole theory of this work. Because it requests only two points, this method is very powerful and overcome most of the difficulties related to other factors such as wind. As later sections will discuss, however, the minimum is difficult to identify in the presence of strong winds or small incidence angles.

From these two methods and the KdV theory presented in the first chapter it is then possible to retrieve the amplitude of the perturbation based on the definition of the characteristic half-width given by equation 4.6.

D.   COMMENTS ON WIND EFFECTS

Equation 4.3 provides an elegant means to qualitatively estimate the influence of different variables on the radar cross-section measured by SAR systems. As explained above, this work simplifies many of the previous equations and omits several important features of the wind effects. In fact, Zheng et al., limited their analysis of the wind effects to comparisons of orders of magnitude between the wave-current source term and wind input source terms.

Wright et al. (1977) first introduced the expression for the wind input presented by Zheng et al. Since then, Chalikov and Belevich (1993) have designed a considerably more complicated expression, currently in use by advanced wave models such as WAM:

$$S_{wd}(f,\varphi)=\beta.\omega.F(f,\varphi). \tag{4.14}$$

$F(f, \varphi)$ is the two-dimensional variance density spectrum of surface elevation expressed as a function of wave frequency and direction. This function is equivalent to the previous Ψ. β is a non dimensional wind-wave interaction parameter which can be approximated by:

$$10^4 . \beta = \begin{cases} -a_1 . \tilde{\omega}_a^2 - a_2 \\ a_3 . \tilde{\omega}_a . (a_4 . \tilde{\omega}_a - a_5) - a_6 \\ (a_4 . \tilde{\omega}_a - a_5) . \tilde{\omega}_a \\ (a_7 . \tilde{\omega}_a - a_8) \\ a_4 (\tilde{\omega}_a - 1)^2 + a_{10} \end{cases} \text{ for } \begin{cases} \tilde{\omega}_a \leq 1 \\ -1 < \tilde{\omega}_a < \Omega_1/2 \\ \Omega_1/2 < \tilde{\omega}_a < \Omega_1 \\ \Omega_1 < \tilde{\omega}_a < \Omega_2 \\ \Omega_2 < \tilde{\omega}_a \end{cases} \text{ where } \begin{cases} \Omega_1 = 1.075 + 75 C_\lambda \\ \Omega_2 = 1.2 + 300 C_\lambda \\ a_0 = 0.25 a_5^2 / a_4 \\ a_1 = 0.25 + 395 C_\lambda \\ a_2 = 0.35 + 150 C_\lambda \\ a_3 = (a_0 - a_2 - a_1)/(a_0 - a_4 + a_5) \\ a_4 = 0.3 + 300 C_\lambda \\ a_5 = a_4 \Omega_1 \\ a_6 = a_0 . (1 - a_3) \\ a_7 = (a_9 . (\Omega_2 - 1)^2 + a_{10})/(\Omega_2 - \Omega_1) \\ a_8 = a_7 \Omega_1 \\ a_9 = 0.35 + 240 C_\lambda \\ a_{10} = -0.05 + 470 C_\lambda \end{cases} \qquad (4.15)$$

In this set of equations, $\tilde{\omega}_a = \dfrac{\omega . u_\lambda}{g} \cos(\varphi - \varphi_w)$, it is the non dimensional frequency of a spectral component. φ_w is the wind direction, u_λ is the wind velocity at some particular elevation $\lambda = \dfrac{2\pi}{k |\cos(\varphi - \varphi_w)|}$ and finally, C_λ is the drag coefficient.

This system is obviously quite complex but presents the advantage of assessing the wind influence on backscattered signal through the term β. As illustrated earlier, the return radar signal depend on the viewing direction from the satellite φ and its wavenumber $k = 2.k_0 . \sin \theta = \dfrac{4\pi}{\lambda_0} . \sin \theta$, with θ being the incidence angle of the satellite system. As the frequency is fixed for a particular radar system, the wind can affect the results because of its magnitude u_λ and the difference between the looking angle φ and the wind direction φ_w. Thus strong wind and upwind/downwind looking angles will favor

64

a strong background radar signal. This effect can obviously cover the signature of non linear internal waves or prevent discrimination of minima. In their paper, Zheng et al., assessed that the maximum wind at which soliton detection by SAR systems is possible should be around 5 m/s. Actually, the maximum wind is thought to be higher than that, around 25m/s for ERS-1 (Raney, 1995) and around 15 m/s for RADARSAT (Staples, personal communication, 2007). This limit depends on the soliton direction and strength, the wind speed and direction; it is also highly dependent on the specifications of the satellite system, particularly its level of saturation.

A lower threshold could be defined as well. Indeed, as presented in the Bragg model, the detection of oceanic features by SAR systems is based on their analysis of the wave spectrum for the radar wavelength. Thus, a smooth ocean observed during no wind conditions will not backscatter anything toward the satellite system, but will reflect the radar signal away from it at an angle equal to the incidence angle, as stated by the laws of optics. The wind must also be strong enough to develop capillary waves or small gravity waves detectable by SAR satellite. From wave theory and observations, this limit could be reached for wind speeds greater than 1.5 m/s. Additionally, a second parameter contributes to the definition of this lowest limit, namely the detection threshold of the satellite system. This parameter, which is highly dependent on the satellite, proves difficult to evaluate. In fact, as stated by Raney (1995), the minimum wind speed that ERS1 requires to detect oceanic features such as slicks or internal waves is about 2.5m/s, and the same condition applies to RADARSAT (Staples, personal communication, 2007). Both of these results are rules of thumb based on observations.

THIS PAGE INTENTIONALLY LEFT BLANK

V.   RESULTS AND OBSERVATIONS (2)

This section will test the two methods presented earlier, which retrieve the width and amplitude of non linear internal waves using satellite data. Some statistics were made to compare the strength of the backscattered signals for the different environments. All the following results and observations were collected during the timeframe of ASIAEX 2001. The different temperature profiles were collected at moorings S4, S5 and S7; the satellite images were observed by the Canadian system RADARSAT; and the wind data were measured by the scatterometer SSMI when available, or given by the global model GFS since no relevant in-situ data were available for this period of time. Within this timeframe, only three pictures containing solitary internal waves were recorded for this area of interest, and they were all provided by RADARSAT. This system was the only SAR system available, as systems such as ERS and JERS experienced some failures. All the data were filtered out using an enhanced lee filter available in ENVI to make them a little smoother and limit the speckle effects inherent to SAR images.

Before looking closely at the results obtained, this section will reflect on the limitations existing in this analysis. First, the small number of pictures available makes it of limited interest regarding statistics, even if it still gives good qualitative information about the relationships between solitons, wind and SAR systems. Additionally, all the wind measurements used in this analysis were provided by SSMI or GFS, whose resolution are respectively 25km and about 100km (1°). The accuracy of this information is expected to be around 20° regarding the direction and around 1-2 m/s regarding the speed; thus, wind effects must be considered with caution. Finally, one of the most difficult parameters to estimate was the speed of the soliton because of the poor vertical and horizontal resolutions of the oceanographic array with regard to this project. This parameter was, however, essential for the calculation of the width of the observed solitons. The speed used to estimate the width of the soliton was a linearly decreasing velocity with the bottom, its average value coming directly from the observations at S7, S5 and S4 and the satellite images; they were also compared to data provided by Ramp (2004).

Finally, the main information regarding the characteristics of the soliton or the environmental data related to the three SAR images are gathered in Table 3 below. In this table, the close and far areas are 5 x 5 km squares for the smallest and greatest incidence angle (no soliton). The soliton area is a 5 x 5km area encompassing the whole soliton signature (dark and bright). The dark and bright areas are 1 x 1km squares associated with the areas of minimum and maximum caused by the soliton. The mean value represents the average brightness within the box. The SAR data were all scaled to bytes in that table (0-255).

Table 3.　　Summary of the statistics observed for different scenes in the three SAR pictures.

Day 114 – 1012GMT- wind direction (to)/speed: 255°/7m/s – looking direction: 77°					
Lat: 21.69°N Long: 117.22°E		Processed Range: 113.3km Incidence Angle: 27.5° Heading: 347°		Soliton width: 530m Soliton amplitude: 105m Soliton propagation: 300°	
	Close	Far	Soliton	Bright	dark
Area	5km x 5km	5 x 5	5 x 5	1 x 1	1 x 1
Pixels	160000	160000	160000	6400	6400
Mean value	139.5	72.2	90.0	123.0	54.2
Standard deviation	60.0	44.0	58.2	61.8	41.3
Day 124 – 1020GMT- wind direction (to)/speed: 210°/5m/s– looking direction: 77°					
Lat: 21.68°N Long: 117.00°E		Processed Range: 112.2km Incidence Angle: 39.1° Heading: 347°		Soliton width: 370m Soliton amplitude: 60m Soliton propagation: 310°	
	Close	Far	Soliton	Bright	dark
Area	5km x 5km	5 x 5	5 x 5	1 x 1	1 x 1
Pixels	160000	160000	160000	6400	6400
Mean value	153.4	107.3	106.4	121.4	87.9
Standard deviation	62.2	53.9	57.4	60.2	53.4
Day 125 – 2215GMT- wind direction (to)/speed: 40°/3m/s– looking direction: 283°					
Lat: 21.87°N Long: 116.92°E		Processed Range: 113.6km Incidence Angle: 23.2° Heading: 193°		Soliton width: 470m Soliton amplitude: 70m Soliton propagation: 295°	
	Close	Far	Soliton	Bright	dark
Area	5km x 5km	5 x 5	5 x 5	1 x 1	1 x 1
Pixels	160000	160000	160000	6400	6400
Mean value	197.7	72.7	174.8	210.8	147.1
Standard deviation	49.8	29.2	54.1	51.8	49.7

A. FIRST CASE STUDY: APRIL 24, 2001
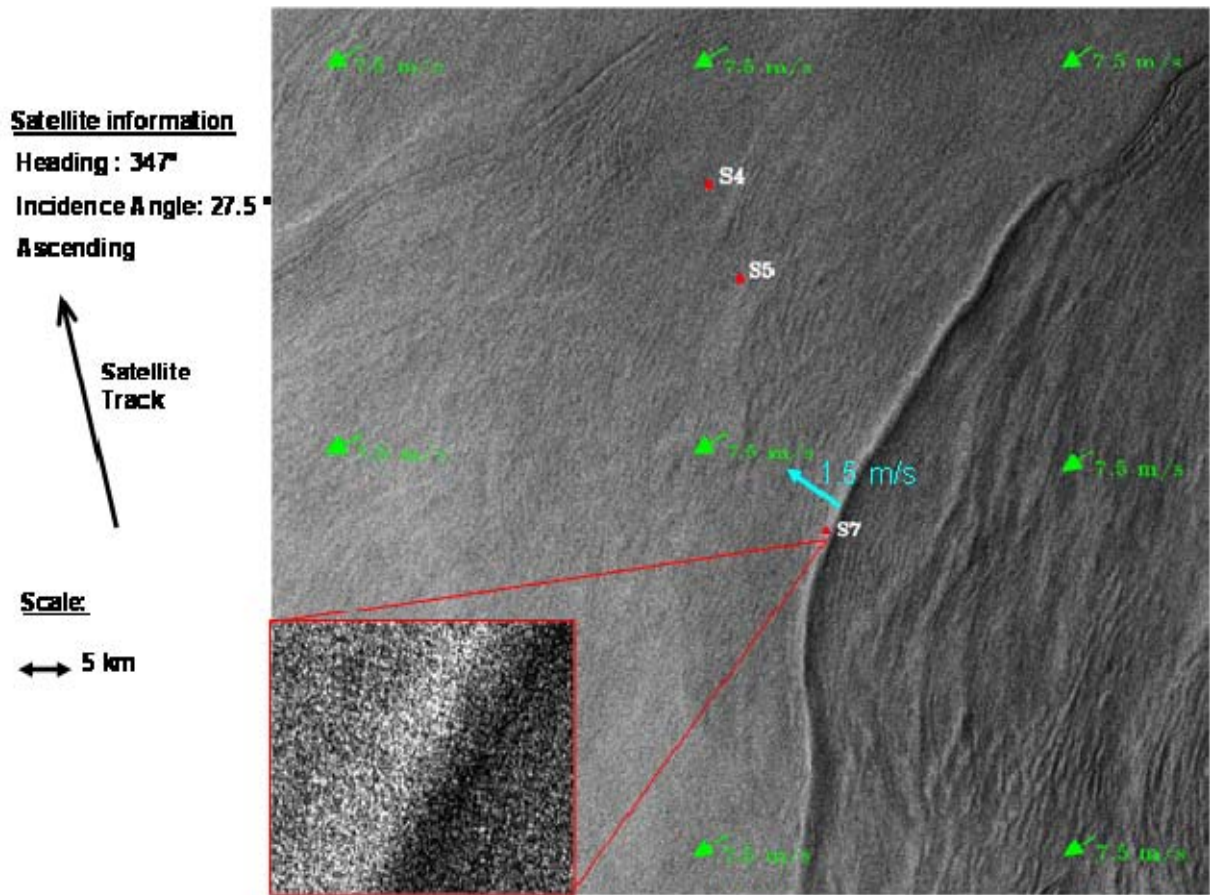
Figure 40.   SAR image from RADARSAT on April 24th, 2001 around 1010GMT as a soliton is passing S7. The satellite track, the scale, the observed current (moorings) and wind (GFS – 1°x1° resolution) are superposed over the picture. A zoomed window (3 x 3 km) is superimposed in the left bottom corner.

This image shows the presence of a large soliton in the vicinity of mooring S7. Its influence is clearly depicted in Figure 41, which represents the temperature observed at 16 different levels as the satellite passed over the area of interest. Based on these last measurements and an approximation of the velocity of the soliton, it is possible to deduce the width of the wave and its amplitude using equation 1.7. Further, it was estimated that the characteristic half-width was about 550 meters, and the amplitude was observed to be 95 meters. It must be noticed here that the amplitude may be quite complex to evaluate.

69

Indeed, the amplitude corresponds to the maximum vertical displacement of water as the soliton comes through. It obviously varies with the strength of the solution as well as the strength of the stratification, which is, in our two-layer model, related to the depth of the upper layer. Here the amplitude is assumed to be the relative maximum vertical displacement as described by Ramp (2004), and the upper layer was defined by looking at the actual density profile.
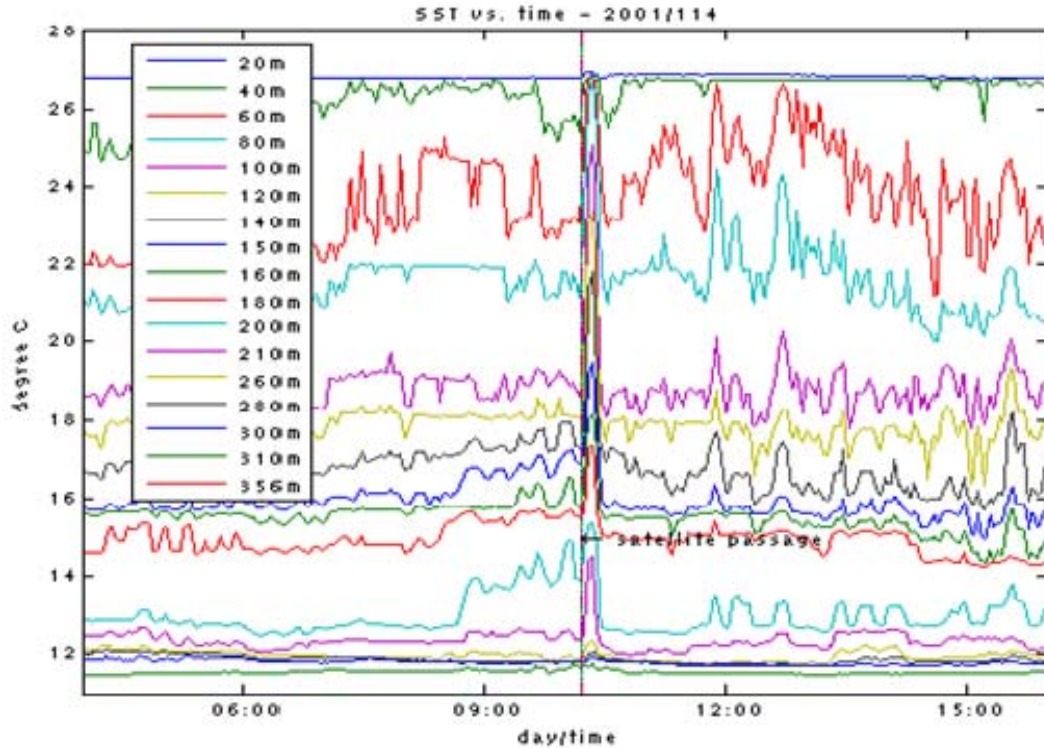
Figure 41.   Temperature measurements at S7 before and after the satellite passage.

To test the methods described by Zheng et al., different transect profiles were observed within the zoomed window in Figure 40. Figure 42 also displays the kind of signature obtainable from a SAR image. Such a noisy plot can be confusing and needs to be analyzed concomitantly with the picture itself. ENVI offers the opportunity to move along the profile and to follow the cursor on the image at the same time. It is then possible to identify the most characteristic points in the bright and dark zones related to the soliton, and identify the maximum and minimum necessary to apply both methods. For this first case, it also appears that the peak-to-peak method presented earlier gives

quite good results, since the observed characteristic half-width was 514 meters, representing a 6 % error. Using the curve fitting method, the characteristic width is also estimated to be between 500 meters and 600 meters as shown in Figure 43. This latter figure emphasizes one of the weaknesses of the method, that being that it is difficult to fit both the bright and the dark parts of the soliton signature. This problem is inherent to SAR systems, since they have both maximum and minimum detection thresholds. From this example, the peak-to peak method seems simpler to use and tends to give better results. In fact, maximum and minimum can be identified quite easily with an uncertainty of one to two pixels, which means less than 50 meters; this resolution is fine enough for most of the applications related to solitons.
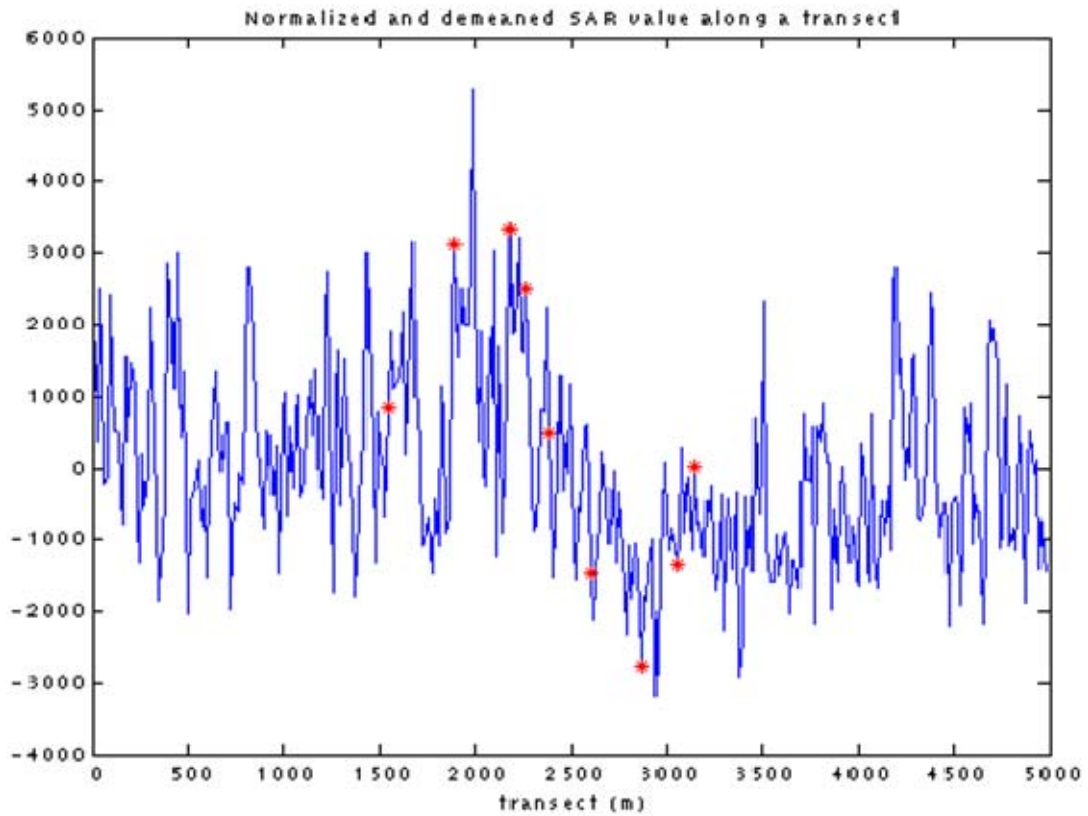
Figure 42.   Normalized and demeaned transect profile of the SAR information across the soliton and in the vicinity of S7. The red crosses represent the significant points chosen to determine the characteristic width of the wave. $d_{pp} = 678m$ and $\Delta = 514m$.

71

It must noticed on the SAR image that here the maximum, minimum, bright and dark areas are all well-defined, which makes the retrieval of the half-width quite easy. In the other cases, however, the boundaries between these different areas were not so obvious because of the wind or the strength of the soliton.
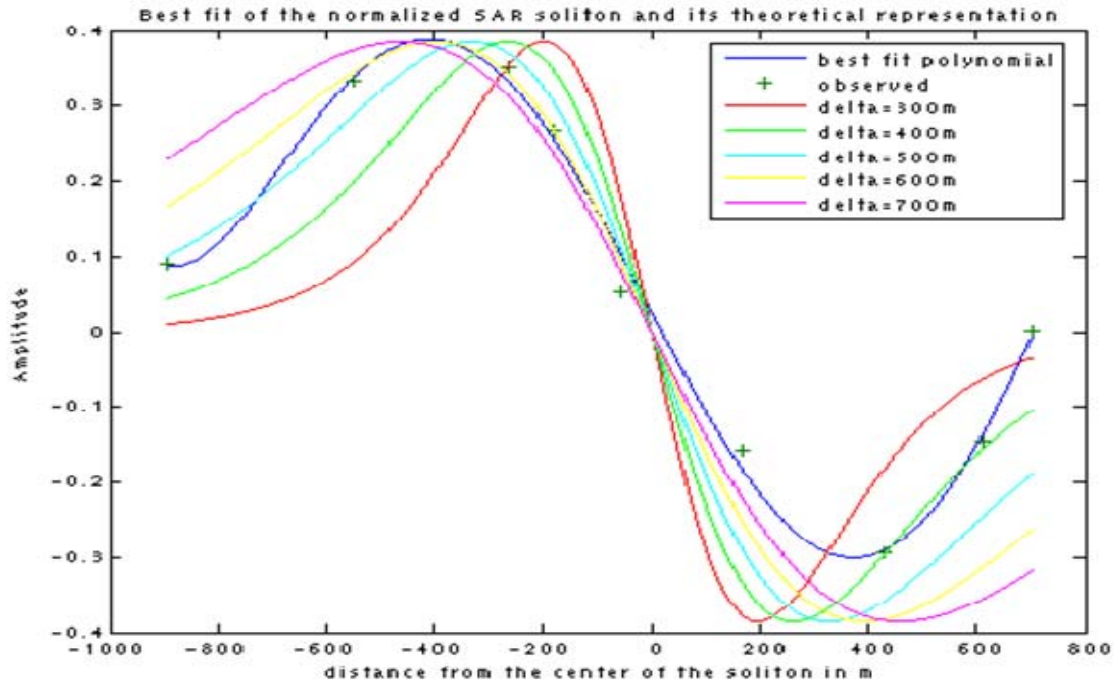
Figure 43.   Best fitted curve (5th order polynomials) and theoretical secant curves associated with the observed soliton for different characteristic widths.

Regarding the amplitude, the results are not as good and the two-layer model presented previously barely resolved this parameter. As exposed in equation 1.7, the characteristic half-width is greatly dependent on the thickness of the upper layer, but because the water column is continuously stratified, it is very difficult to set a clear limit between the two layers (Figure 44). If one chooses to set the upper layer to be defined by the mixed layer depth or the original depth of the more displaced water, it appears that Zheng's model tends to underestimate the amplitude of the wave. For example, for a 90 meter upper layer at S7, the amplitude is expected to be only around 30 meters, less than a half of the observed value. This part of the model is clearly a limitation to the application of this theory, and future implementation requires improvements by using some stratified models such as the one described by Lamb and Yan (1996). Moreover, the

secant function in the model makes the amplitude very sensitive to the depth of the upper layer, as illustrated in Figure 45.
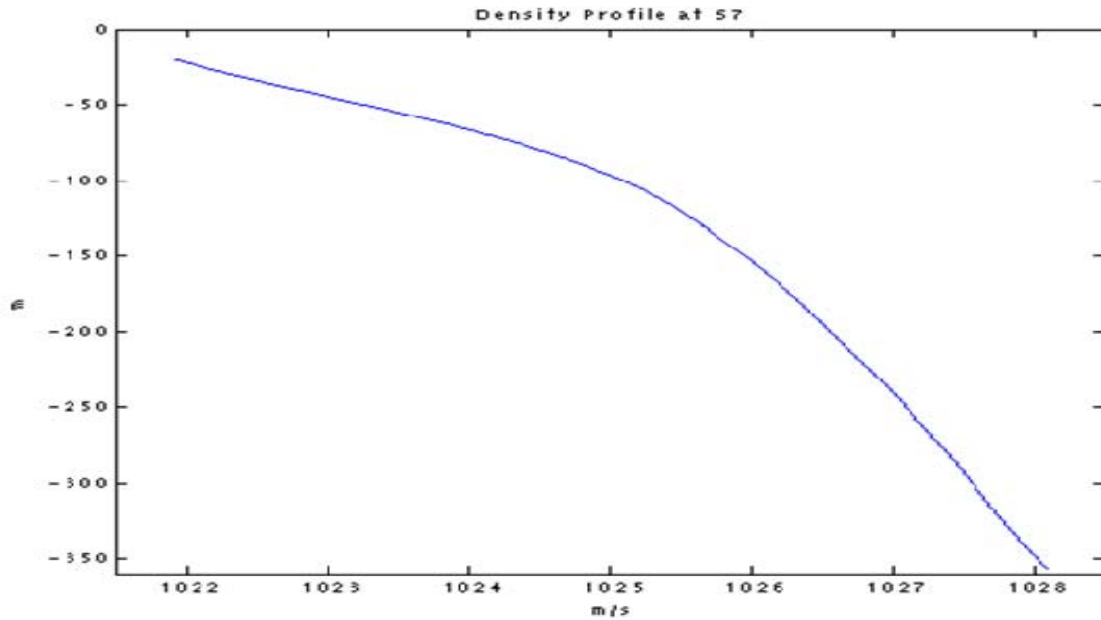
Figure 44.   Average density profile at mooring S7 during ASIAEX2001.
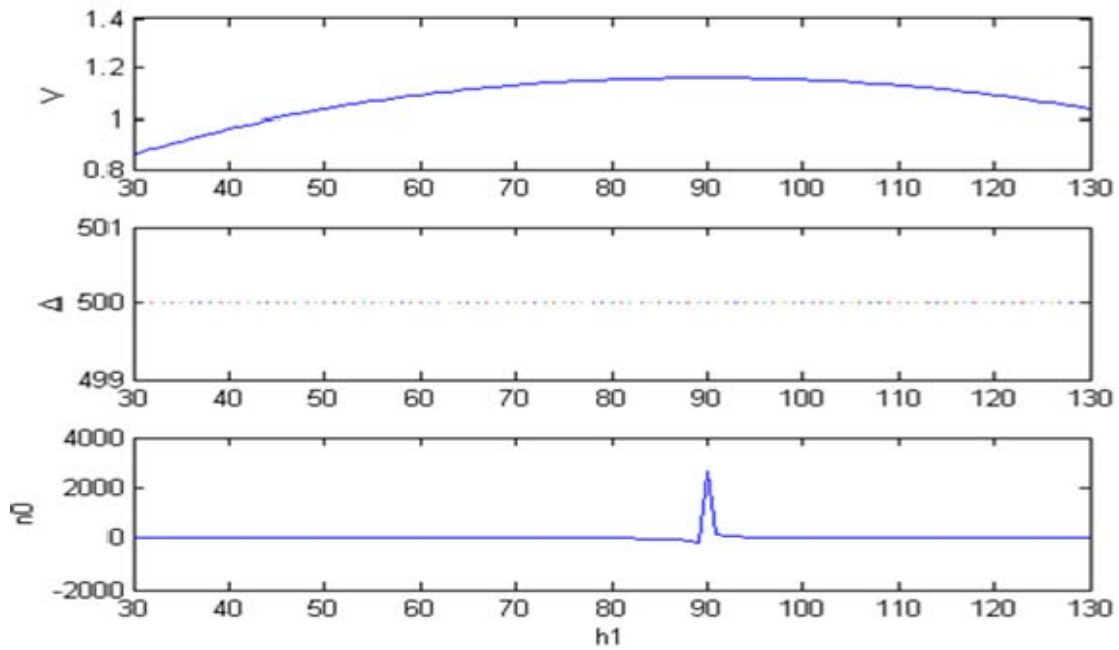
Figure 45.   Sensitivity of the amplitude and the propagation speed of the soliton to the definition of the upper layer depth, h_1 at mooring S5. The characteristic half-width is set to be 500 meters.

B. SECOND CASE STUDY: MAY 4, 2001

The first case offered the clear depiction of a soliton on a SAR image. However, for this second case, the presence of non linear waves was not so obvious, as illustrated in Figure 46. These internal waves would have been difficult to obtain without the collection of oceanographic data at moorings S5 and S4, because of speckling effects caused by SAR. Moreover, even if many solitons were observable on May 4, 2001 in the South China Sea, they were all quite small. In this example, only the leading soliton of the series will be described. The characteristics of this wave are an upper layer depth equal to 80 meters, an amplitude equal to 40 meters and a width around 530 meters . The analysis of the current feature utilized an approach identical to that of the first case study, and is presented in the following figures.
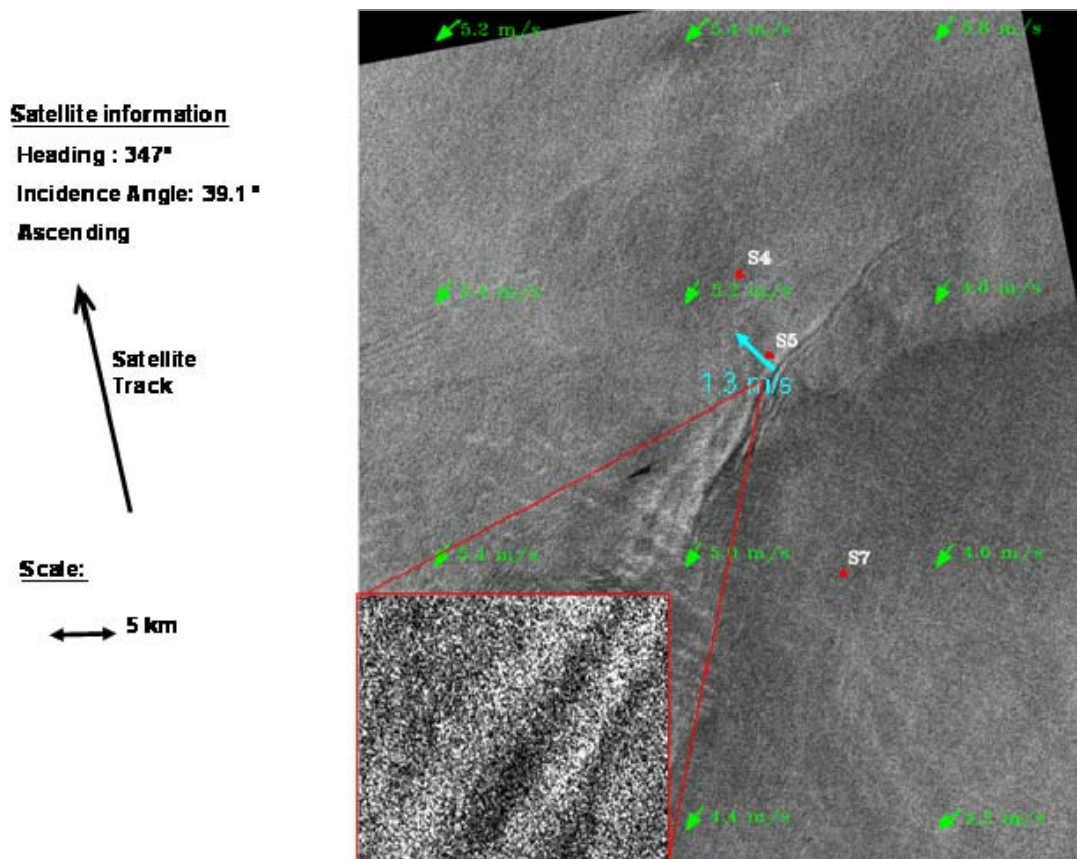
Figure 46.   SAR image from RADARSAT on May 4, 2001 around 1020GMT as a soliton is passing S5. The satellite track, the scale, the observed current and wind (GFS) are superimposed and a zoom of the area of interest is added in the bottom left corner.

74

The presence of solitons in the South China Sea is once again quite obvious in Figure 47, which represents the evolution of the temperature profiles for different levels at mooring S5. This series of waves is characteristic of a perfect dnoidal group of solitons, as presented in the introduction of this paper (Figure 3). Equation 4.9 expresses the backscattered energy and shows that it is highly dependent on the depth of the upper layer, the width of the soliton and the amplitude of the wave, as well as the wind characteristic or the incident angle. For this case, all the parameters which could make the signature of the non linear waves noticeable acted against it. Indeed, the incidence angle was quite large and greater than 35°, which reduces the backscattered energy. Additionally, both the looking direction and the wind direction made the SAR system less efficient (Table 3 and 4), the three parameters which characterize the wave tended to decrease the backscattered energy. Surprisingly, the signature was still noticeable, and these observations may suggest than even weak solitons are observable by SAR images as soon as enough wind blows to create capillary waves to return the radar signal.
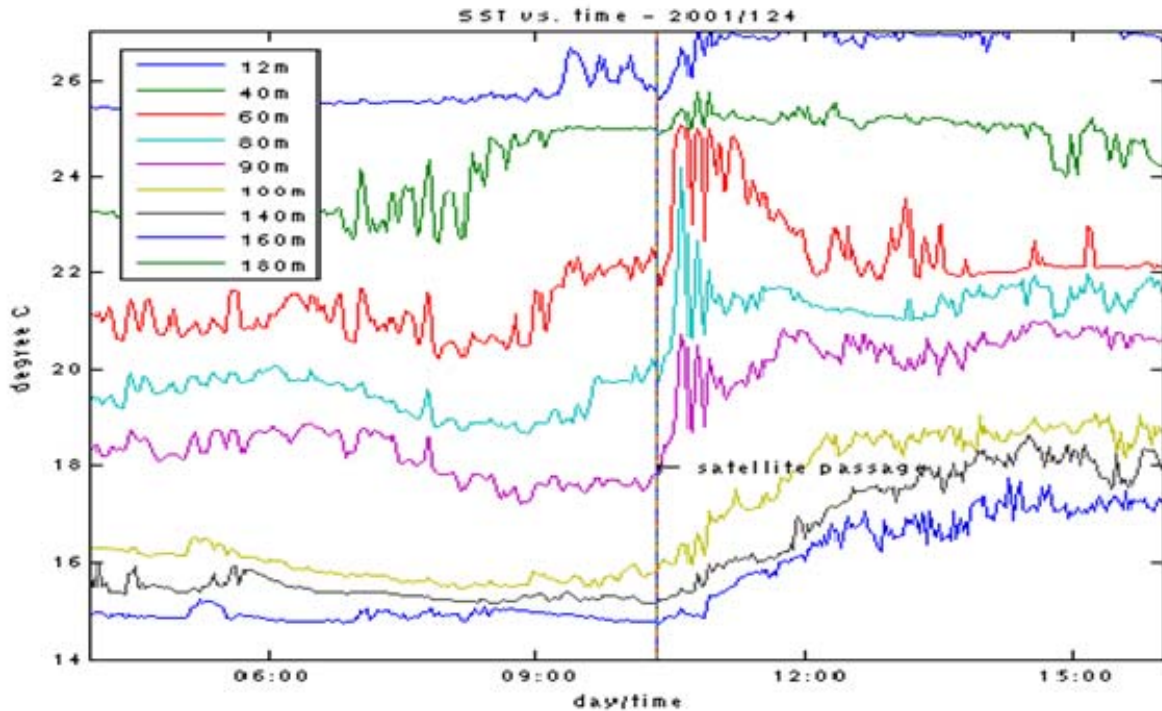
Figure 47.   Temperature measurements at S5 before and after the satellite passage at 8 different levels.

Applying Zheng's method to this picture was, however, very difficult for this case, and the results obtained are not very conclusive. As illustrated in Figures 48 and 49, the SAR data observed were quite noisy, and the fit curving shows its limitations, since it was impossible to get a clear representation of the presence of the soliton within the noise. Thus, the best fit polynomial (fifth order) used here does not at all match the theoretical representation of the wave for different widths (Figure 49). Moreover, as shown in the zoomed window of Figure 46 compared to Figure 48, the distinction between dark and bright areas is not as clear, rendering determination of the location of the maximum and minimum more difficult. Indeed, using the peak-to peak method, the characteristic width is estimated to be a little bit less than 400 meters, while the observations give a result greater than 500 meters. Once again, here the results for the amplitude were not very good.
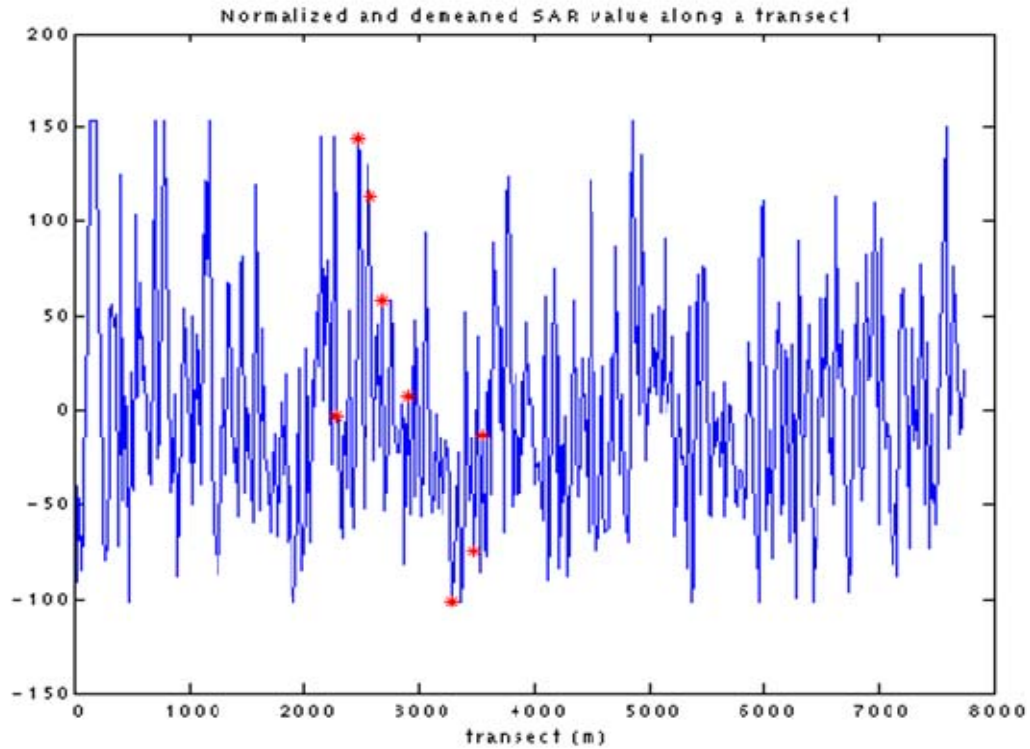
Figure 48.   Normalized and demeaned transect profile of the SAR information across the soliton and in the vicinity of S5. The red crosses represent the significant points chosen to determine the characteristic width of the wave. $d_{pp} = 520m$ and $\Delta = 393m$.
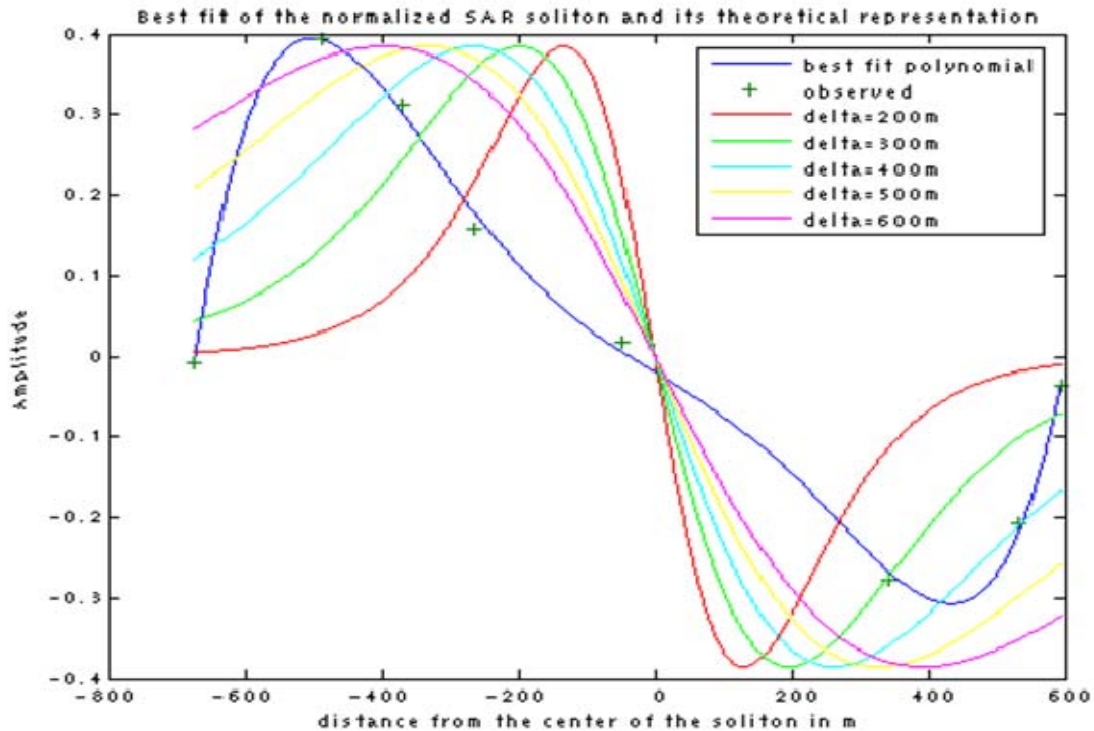
Figure 49.   Best fitted curve (5th order polynomials) and theoretical secant curves associated with the observed soliton for different characteristic widths.

C.   THIRD CASE STUDY: MAY 5, 2001

This last case study offers interesting complimentary information regarding SAR detection of non linear internal waves. For this particular picture, the incidence angle at the closest edge to the satellite was very small, around 20°, which is a value for which the Bragg scattering theory applies less confidently. Secondly, in this case, winds were thought to be very light, blowing at speeds close to 3 m/s. This latter value was given by the large grid model GFS, and can be considered as doubtful or inaccurate. Nonetheless, the value still offers a good order of magnitude, and one can assume that the wind speed was within 1 m/s of this value. As shown in Figure 50, the soliton could, however, be easily identified for many reasons. First, the orientation of the looking direction with respect to the wind direction was favorable. Furthermore, the small incidence angle supports a stronger backscattered signal, which, while enhancing the presence of the

wave, does not help in discriminating maximum and minimum. Finally, the characteristics of the soliton render it strong enough to be detectable by the satellite system. The upper layer was estimated to be around 80 meters, while the amplitude of the wave at this location was about 50 meters. The width of the soliton was approximately 300 meters, making it a lot sharper than the two previous waves but with a greater amplitude than the second case study.
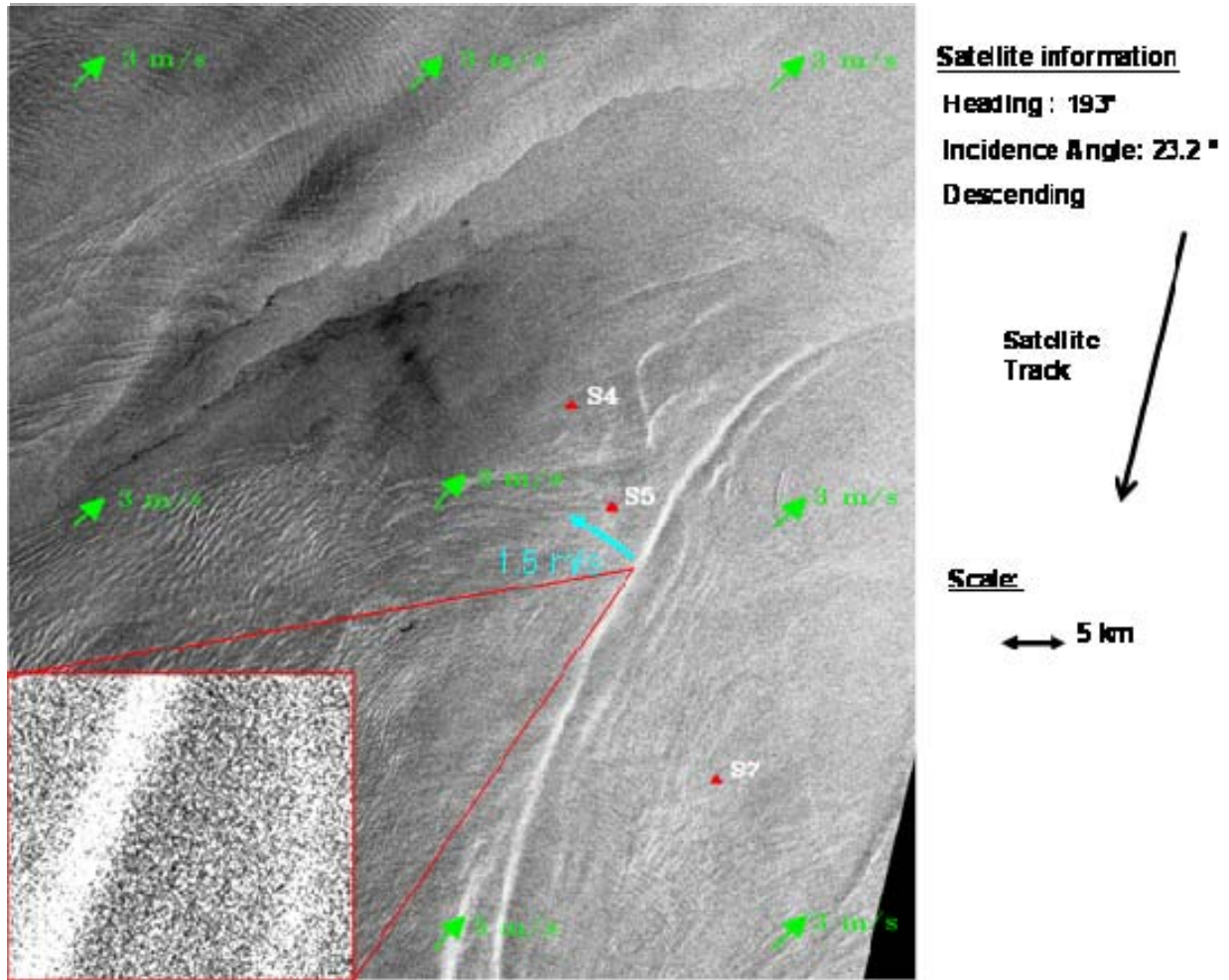
Figure 50.   SAR image from RADARSAT on May 5, 2001 around 2215GMT as a soliton is passing S7. The satellite track, the scale, the observed current (moorings) and wind (GFS –1°x1°resolution) are superposed over the picture. A zoomed (3 x 3 km) window of the area is added in the bottom left corner) of the picture.

Comparison of the pictures offers interesting insight because the last two cases shared close soliton characteristics. In the second case, the soliton was very difficult to identify in the noise, whereas the signature is very clear in this last case. The fourth section of this chapter will look closely at these observations, while the immediate section will focus on the determination of the width and the amplitude using the two methods. Once again, only the leading soliton was considered, even though a second and a third following wave was noticeable both on Figure 50 and 51. In this last figure, it must be noticed that the signature of the soliton is more obvious than in the previous case.
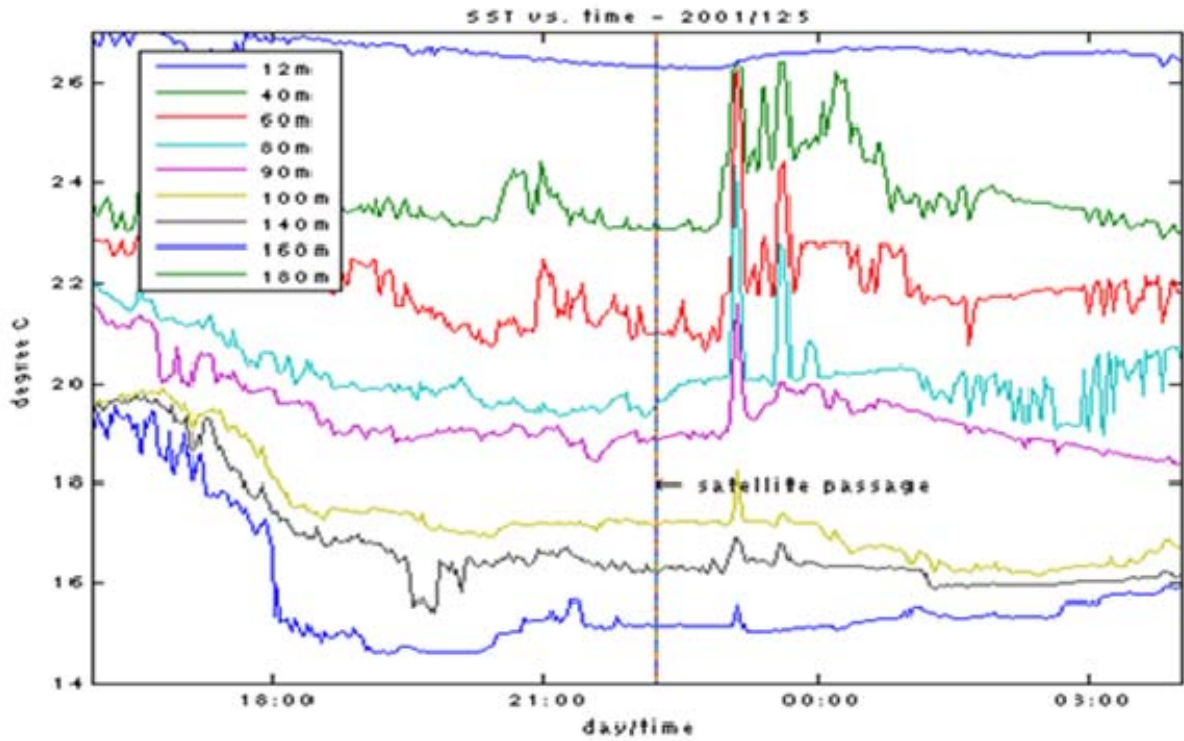
Figure 51.   Temperature measurements at S5 before and after the satellite passage at 8 different levels.

From the peak to peak method, the characteristic half-width was calculated to be around 450 meters, while the curve fitting method determined it to be between 500 and 600 meters. These two results are both quite far from the mooring observations, which state that the half-width was about 300 meters. Once again, the amplitude was greatly underestimated with these two procedures. These complications in the prediction of

79

soliton width most likely arise from the small incidence. The small incidence angle creates a strong background reflected energy that probably hid the minimum associated with the soliton. The small incidence also tends to make the maximum larger as more pixels reach the saturation threshold of the system. As noticeable in the zoomed window of Figure 50, it was very difficult to discriminate significant points from the background in the expected dark area of the soliton or to set an accurate minimum for the peak to peak method. The light wind which blew on May 5 probably did not favor strong interactions with the soliton and the appearance of a negative or below normal signal.
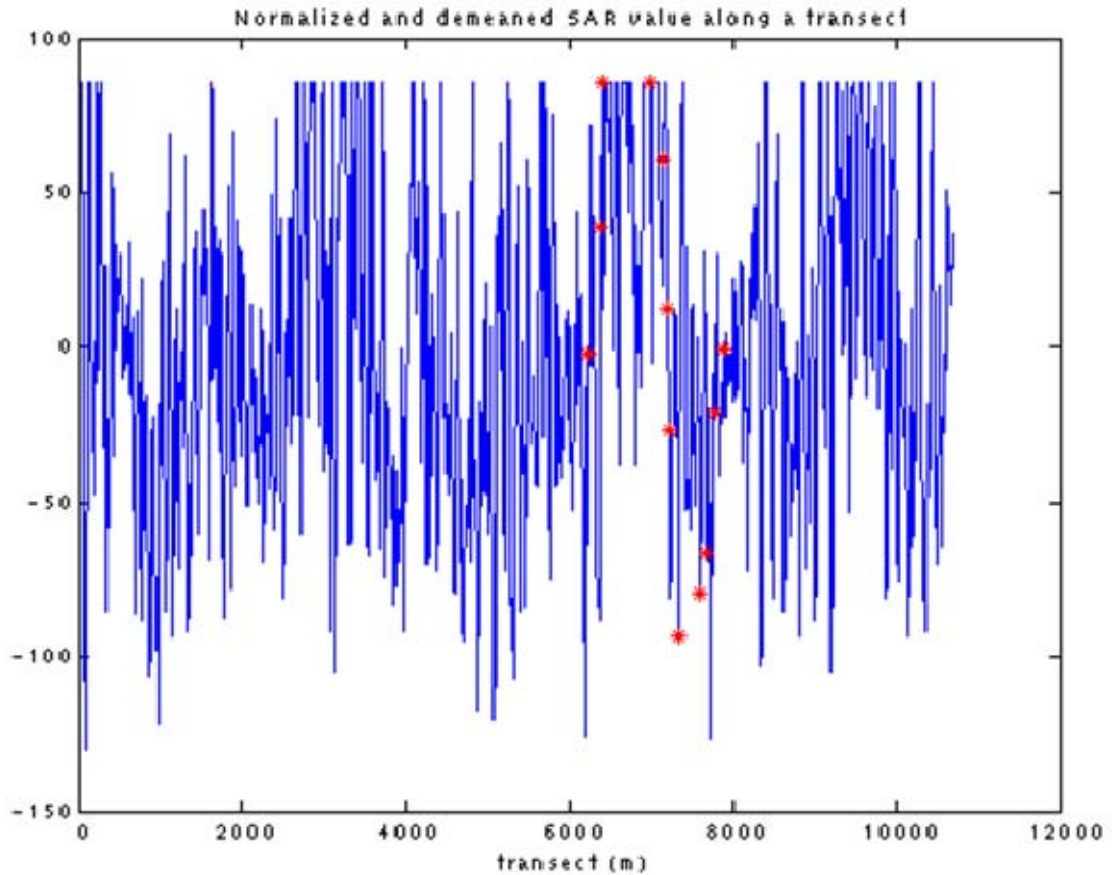
Figure 52.   Normalized and demeaned transect profile of the SAR information across the soliton and in the vicinity of S5. The red crosses represent the significant points chosen to determine the characteristic width of the wave. $d_{pp} = 594m$ and $\Delta = 450m$.
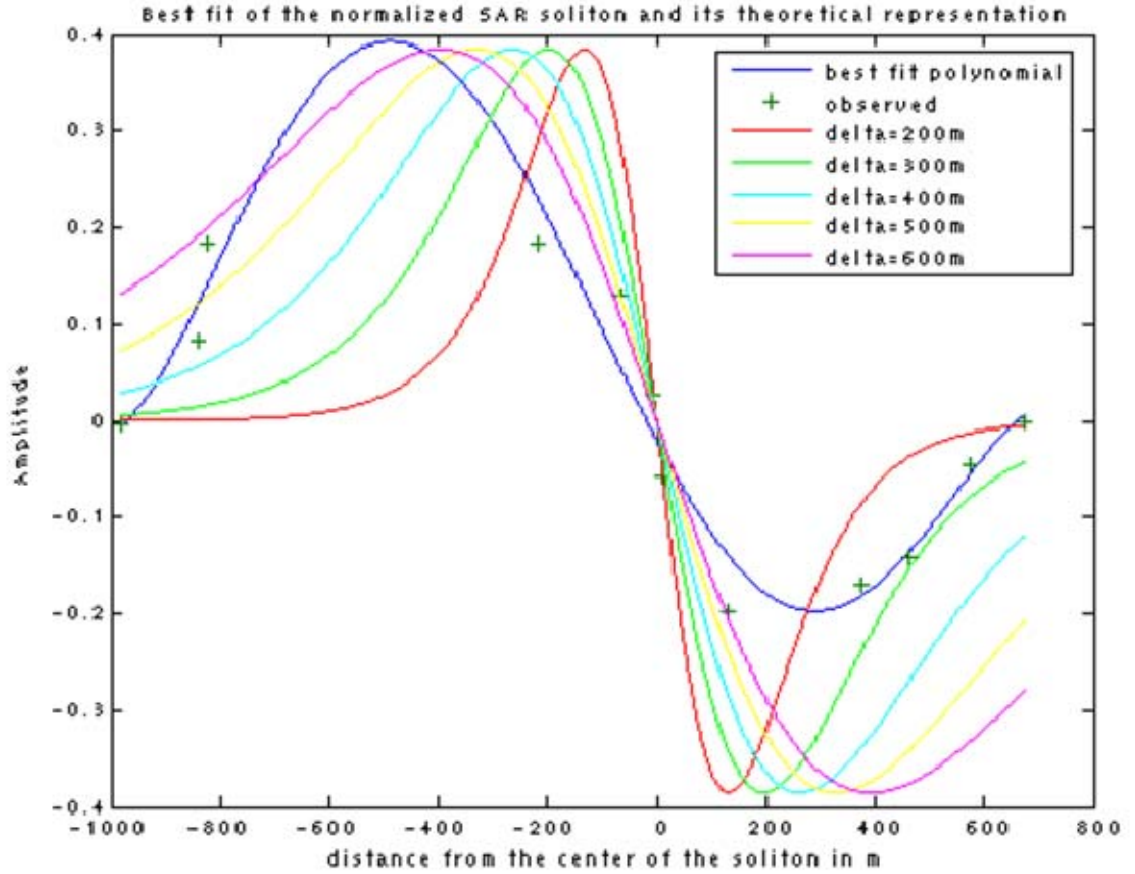
Figure 53.   Best fitted curve (5th order polynomials) and theoretical secant curves associated with the observed soliton for different characteristic widths.

D.   STATISTICS AND COMMENTS

In their study, Zheng et al., promoted their method and claimed that it was capable of retrieving the main characteristics of the solitons; this was verified with our first case study for the width. The theory behind this elegant model is certainly correct, even if some parameters could be described more accurately. However, the last two case studies presented above enhance the limitations associated with it. From the three case studies, it also appears that the second method based on the distance between minimum and maximum is much more conclusive that the one based on curve fitting. The method provides an easier way to get the characteristic half-width of a soliton, since it only

requires two points. Compared to the collection of huge amounts of oceanographic data, this method can also be considered accurate enough to get the characteristic width necessary for the acoustic model presented previously or some other applications involving solitons. From these examples, it also seems much more complicated to get the amplitude right, and this part of the theory should be reviewed in a future work. The main weaknesses of Zheng's method were probably related to two important factors: wind considerations and the building of the reference axes, which brings out the connection between the wind direction, the soliton propagation and the looking angle of the satellite.

1. Wind and Incidence Angle Effects

As discussed previously, the wind and the incidence angle are factors which can significantly affect the detection or characterization of non linear internal waves. The following table gathers some information about the three previous SAR pictures and aims at comparing the relative effects of the incidence angle, the wind speed and direction and the strength of the soliton. Once again, these results must be used carefully, since the wind information from the scatterometer SSMI or the model GFS are not very precise.

Table 4.   Relative variation in backscattered energy implied by the presence of a soliton in the image along with environmental information.

Relative deviation from the background	Bright area	Dark area	Standard deviation within the soliton	$\Delta\varphi = \varphi - \varphi_w /$ $\cos(\Delta\varphi)$	Wind speed	Soliton amplitude and width (m)
Day 114	+46%	-35%	+21%	-178° / -1.0	7	105/530
Day 124	+7.5%	-22%	+2%	-133° / -0.68	5	60/370
Day 125	+23%	-14%	+9%	243° / -0.45	3	70/470

The basic results illustrated in this table are the enhanced features brought by the presence of a soliton. Thus, for the first case, the brightness is increased by 46% in the bright zone and decreased by 35% in the dark, which make the wave very easy to discriminate. This result is also observed for the two following cases, though the

variations are not as dramatic. In the following two cases, the angle $\Delta\varphi$ is less favorable and the wind is lighter. From only three pictures, it is difficult to determine the most efficient wind speed regarding SAR detection of solitons; nor can the importance of wind speed relative to wind direction be established. Resolution of these issues requires a more thorough study. It seems, however, that winds around 5m/s offer better results than light and strong winds. From comparisons of order of magnitudes between the terms of equation 4.4, Zheng et al., stated in their paper that the maximum wind stood by SAR systems should be around 5 m/s. Looking at the different cases presented here, one could objectively expect this wind threshold to be higher than that and closer to 10 or 15 m/s (Raney, 1995).
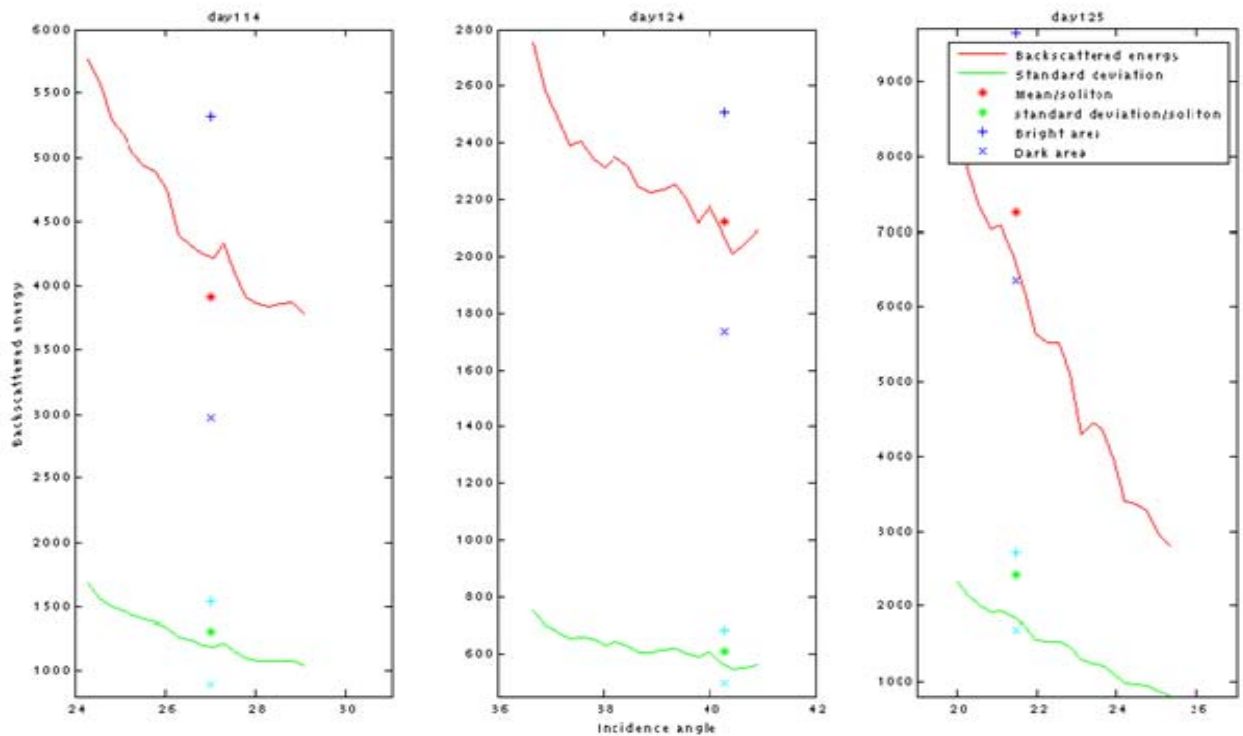
Figure 54.   Backscattered energy (and standard deviations) for different incidence angles and for three different environments (day 114, day 124 and day 125). Statistics associated with the bright and dark signatures of the soliton are indicated by blue crosses (1 x 1 km). The red and green stars indicate the average over an area including both the bright and the dark areas.

Figures 54 and 55 display the mean backscattered energy and its standard deviation for 5km x 5km squares. The discrete values (stars) represent the backscattered energy in the bright and dark areas associated with the solitons (1km x 1km) and the mean and standard deviation for 5km x 5km areas centered on the solitons.

These two figures emphasize the effects of the incidence angle on the backscattered energy. These figures also clearly show the signature of the soliton. Finally, in Figure 55, the comparison between day 114 and day 125 reveals that, for the same incidence angle, the returned energy is much stronger in the presence of moderate or strong winds. Moreover, it seems that as the angle decreases the system tends to saturate much faster.
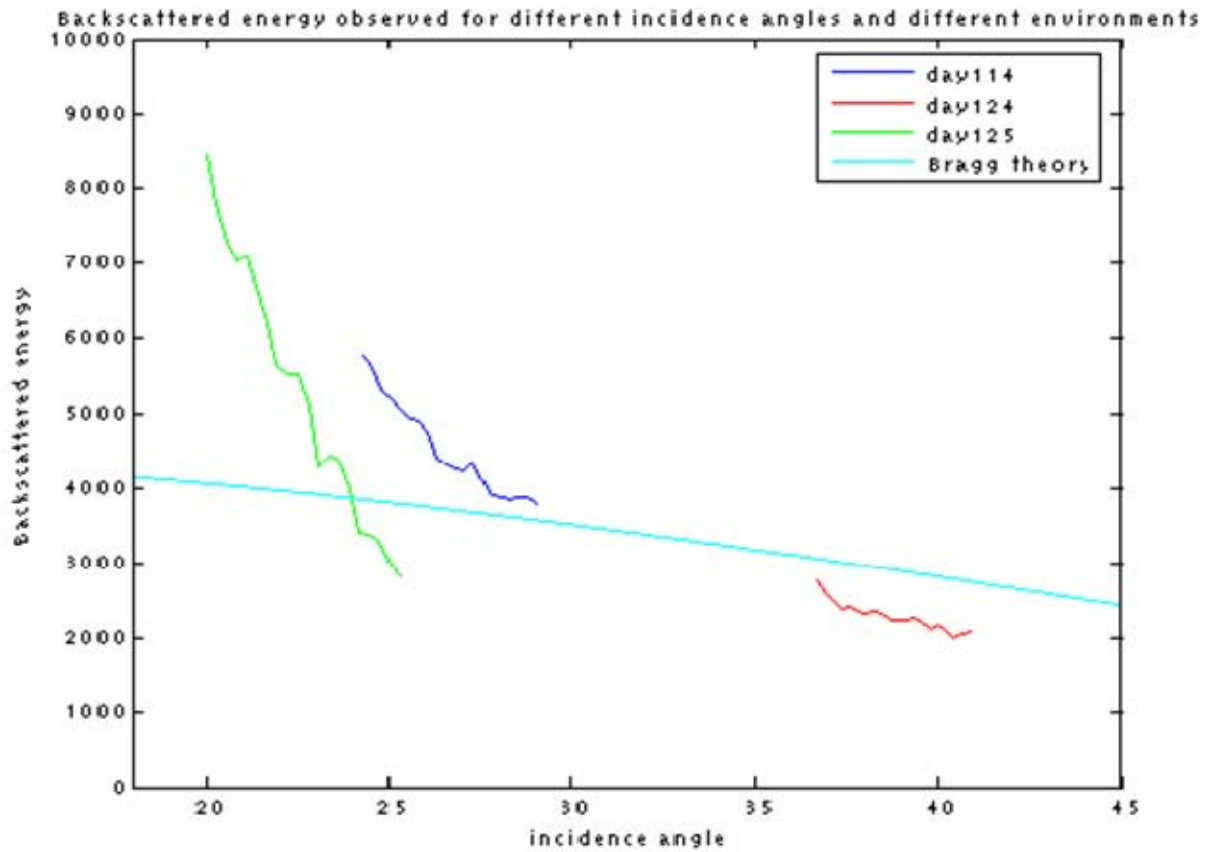

Figure 55.   Backscattered energy observed for different incidence angles for 3 different environments. The turquoise line represents a scaled scattering coefficient $g_{HH}(\theta)$.

2. Conclusions and Future Works

As stated earlier, because of the small amount of data available, this study could not aim at giving exhaustive conclusions about the relationships between SAR systems, solitary internal waves and wind. However, this study offered several interesting insights, among which was the fact that solitons can be detected for low winds around 2 to 3m/s, and that the width of a soliton can be approximated accurately enough for many operational purposes using Zheng's method. This study is, however, of a qualitative nature, and a thorough experiment should be conducted to infer more accurate conclusions about the wind effects on SAR detection of solitons. The ASIAEX experiment was a good start for this kind of analysis, since it gathers oceanographic data, acoustic data and SAR data. The following discussion provides several suggestions for improving the current analysis; the expensive cost of such improvements would also be debatable, but detailed reflection on this point is outside the scope of this conclusion.

Clearly, future study requires better spatial resolution. The spacing between S7 and S5 here was about 25 km and 5 km between S5 and S4, making the observations of the propagation speed very difficult. This parameter is, however, essential in the determination of the width of the soliton. The timeframe of the whole experiment should be increased, much like it was during the Windy Islands Experiment (WISE) in 2005; unfortunately, the cost of the SAR images taken during the experiment in question precluded their use in this study. The current SAR systems do not repeat their cycles very often; to obtain solitons, as well as a large variety of wind conditions and multiple SAR images, requires a long experiment, probably around 5 or 6 months. On the other hand, studies could proceed with surveillance of many areas at the same time. As stated earlier, wind is an important variable in that comparison, and only poor data were available for this study. A thorough experiment would require the observations of surface winds by buoys concomitantly with the oceanographic measurements. Finally, improvements in the method proposed by Zheng et al., are necessary to get correct amplitudes for the solitons, as this parameter is even more important than the width, particularly for acoustic purposes.

THIS PAGE INTENTIONALLY LEFT BLANK

VI. CONCLUSION

Non linear internal waves are currently a hot topic in the oceanographic, acoustical and military communities since they contribute greatly to the water column variability. Using data collected during an experiment in South China Sea in 2001, this project tested the ability of a simple analytic model based on Dyson series to characterize acoustic intensity fluctuations through the retrieval of mode amplitude in the presence of solitons. This theory, presented in the first three chapters of this report, demonstrates its viability by obtaining relevant results for mode 1, one of the most energetic regarding the settings of the experiment. Though the results were not as conclusive for higher modes, the model appears promising. The model relies on several assumptions, such as the weak mode coupling approximation, the single scattering theory or the simplistic depiction of the interactions between the non linear internal waves and the bottom. Nevertheless, the model returns solid qualitative results regarding the mode energy variations. In particular, one of the most satisfying results of this analysis is the prediction of the fast oscillations of the acoustic mode energy as the ISWs move away from the source. Regarding the spreading of the signal observed in the data from ASIAEX 2001, the modeled data did not agree with the observations. The modeled spreading was too small, and the increase of the spreading with time predicted by the model was not observable in the in-situ data. Other environmental variability, such as random linear waves, diurnal effects or mesoscale phenomena, are most likely responsible for the discrepancies in the model.

Moreover, it appears that the measurements collected during ASIAEX 2001 did not perfectly match those required to conduct this comparison. Despite the vast amount of data collected during this experiment, it was very difficult to obtain some of the main characteristics of the ISWs, such as their amplitude, width and speed, this latter variable being a very sensitive input for the mode. In fact, only two moorings were truly available to simulate the speed of the soliton and to provide information about the amplitude and width. This constraint negatively affected the accuracy of the comparison. Because of this drawback, it might prove beneficial to conduct a more thorough analysis of this model using experiments with simpler bathymetry, continuous measurements and finer spatial

resolutions, particularly regarding the spacing between moorings and between the source and the receiver. Regarding the limitations of this model, future studies should probably focus on determining its domain of applicability with respect to water depth and frequency. The current study proved that the results calculated by the model were quite poor for very shallow waters less than 150 meters, generally due to the complex interactions of the waves with the bottom. This model would also most likely break down for frequencies greater than 1000Hz, for which the single scattering theory will no longer apply.

As stated in the second and third chapters of this report, the amplitude, characteristic half-width and the propagation speed of the soliton proved to be essential inputs for the model. This project also described how SAR systems could obtain this information. Indeed, over the recent decades, these systems proved their capacity at detecting these particular oceanic features and will soon be able to describe their inner characteristics. Obviously, the current techniques, such as the one presented by Zheng et al., offer only approximate results; however, a few computational and theoretical improvements in their methods could significantly improve these methods. This study also particularly noted the importance of wind effects in the analysis of SAR images and the retrieval of soliton information. This analysis emphasized the evidence of upper and lower thresholds regarding wind speed, but the limited amount of data prevents an accurate definition. Estimations thus stem from existing data collected by SAR systems for winds between 3 and 12 m/s.

LIST OF REFERENCES

Alpers, W., **(1985)**. "Theory of radar imaging of internal waves," Nature, 314, pp. 245-247.

Apel, J. R., **(1979)**. "Observations of internal wave surface signatures in ASTP photographs.," Apollo-Soyuz Test Project Summary Science Report, F. El-Baz and D. M. Warner, Eds., NASA Publication SP-412, pp. 505-509.

Apel, J. R., L. A. Ostrovsky, Y. A. Stepanyants and J. F. Lynch **(2007)**. "Internal solitons in the ocean and their effect on underwater sound," J. Acoust. Soc. Am, 121(2), pp. 695-722.

Chalikov, D. V., and M. Y. Belevich, **(1993)**. "One-dimensional theory of the wave boundary layer," Bound.-Layer Meteor., 63, pp. 65-96.

Chiu, C.S., S. R.Ramp, C. W. Miller, J. F. Lynch, T. F. Duda, and T. Y.Tang, **(2004)**. "Acoustic intensity fluctuations induced by South China Sea internal tides and solitons," IEEE J. Oceanic Eng. 29(4), pp. 1249-1262.

Colosi, J. A., **(2007)**. "Acoustic mode coupling induced by shallow water nonlinear internal waves: Sensitivity to environmental conditions and space-time scales of internal waves," J. Acoust. Soc. Am, submitted in 2007.

Creamer, D.B., **(1996).** "Scintillating shallow water waveguides," J. Acout. Soc. Am., 99(5), pp. 2825-2838

Dozier, L.B. and F.D. Tappert, **(1978)**. "Statistics of normal-mode amplitudes in a random ocean. I. Theory.," J. Acout. Soc. Am., 63, pp. 353-365

Dozier, L.B., **(1982)**. "A coupled mode model for spatial coherence of bottom-interacting energy," *Proceedings of the Stochastic Modeling Workshop*, edited by C.W. Spofford and J.M. Haynes (ARL-Universityof Texas, Austin Texas)

Duda, T. F., and J. C. Preisig **(1999)**. "A modeling study of acoustic propagation through moving shallow water solitary wave packets," IEEE, J. Oceanic Eng. 24(1), pp. 16-32.

Duda, T.F. , J. F. Lynch, J. D. Irish, R. C. Beardsley, S. R. Ramp, C.-S. Chiu, T. Y. Tang, and Y. Y. Yang, **(2004a)**. "Internal tide and nonlinear internal wave behavior at the continental slope in the Northern South China Sea," IEEE J. Oceanic Eng. 29(4), pp. 1105-1130.

Duda, T. F., J. F. Lynch, A. E. Newhall, L. Wu, and C.-S. Chiu, **(2004b)**. "Fluctuations of 400 Hz sound intensity in the 2001 ASIAEX South China Sea experiment," IEEE J. Oceanic Eng., 29(4), pp. 1264-1279.

Fredricks, A., J. A. Colosi, J. F. Lynch, G. Gawarkiewicz, C.-S. Chiu, and P. Abbot **(2005)**. "Analysis of multipath scintillations observed during the summer 1996 New England shelfbreak PRIMER study," J. Acoust. Soc., 117(3), pp. 1038-1057.

Headrick, R. H., J. F. Lynch, J. N. Kemp, A. E. Newhall, K. Von de Heydt, J. R. Apel, M. Badiey, C.-S. Chiu, S. Finette, M. H. Orr, B. Pasewark, A. Turgot, S. Wolf and D. Tielbuerger **(2000)**. "Acoustic normal mode fluctuation statistics in the 1995 SWARM internal wave scattering experiment," J. Acoust. Soc. Am, 107(1), pp. 201-220.

Hsu, M.-K., and A. K. Liu, **(2000)**. "Internal wave study in the South China Sea using SAR" Continental Shelf Research, 20 (4-5), pp. 389-410.

Jensen, F. B., W. A. Kuperman, M. B. Porter, and H. Schmidt, **(1993)**. "Computational Ocean Acoutics," Springer-Verlag, New York.

Kinsman, B., **(1984)**. "Wind waves, their generation and propagation on the ocean surface," Dover Publications, Inc, New York.

Lamb, K. G., and L. Yan, **(1996)**. "The evolution of internal wave undular bores: Comparisons of a fully nonlinear numerical model with weakly nonlinear theory'', J. Phys. Oceano., 26, pp. 2712-2734.

Le Caillec, J.-M., **(2006)**. "Study of the SAR signature of internal waves by non linear parametric autoregressive models," IEEE J. Geoscience Remote Sensing, 44(1), pp. 148-158.

Liu, A. K., Y. Zhao, T.Y. Tang. And S. R. Ramp, **(2004)**. " A case study of internal wave propagation during ASIAEX 2001," IEEE J. Oceanic Eng., 29(4), pp. 1144-1156.

Lynch, J. F., G. G. Gawarkiewicz, C.-S. Chiu, R. Pickart, J. H. Miller, K. B. Smith, A. Robinson, K. Brink, R. Beardsley, B. Peerry, and G. Potty, **(1997)**. "Shelfbreak PRIMER – An integrated acoustic and oceanographic field study in the mid-Atlantic Bight," in Sahllow-Water Acoutics (R. Zhang and J. Zhou Editors), China Ocean Press, pp. 205-212.

McGoldrick, L. F., (1965). "Resonant interactions among capillary-gravity waves," J. Fluid Mech., 21, pp. 305-331.

Munk, W. H., and F. Zachariasen, **(1976)**. "Sound propagation through a fluctuating stratified ocean: Theory and observations. J. Acoust. Soc. Amer., 59, pp. 818-838.

Olmsted, C., **(1993)**. "Alaska SAR Facility – Scientific SAR user's guide," ASF.

Osborne, A. R., and T. L. Burch, (1980). "Internal waves in Adaman Sea," Science, 208, pp. 451-460.

Phillips, O. M., **(1977)**. "The Dynamics of the Upper Ocean – 2nd edition," pp. 67-68, Cambridge Univ. Press. New York.

Plant, W. J. **(1990)**. " Bragg scattering of electromagnetic waves from air/sea interface," Surfaces Waves and Fluxes, vol. II, Remote Sensing, edited by G.L. Geernaert and W. J. Plant, pp. 41-108, Kluwer Acad., Norwell, Mass.

Preisig, J. C. and T. F. Duda, **(1997)**. "Coupled acoustic mode propagation through continental-shelf internal solitary waves," IEEE J. Oceanic Eng. 22, pp. 256-269.

Ramp, S. R. , T. Y. Yang, T. F. Duda, J. F. Lynch, A. K. Liu, C.-S. Chiu, F. L. Bahr, H.-R. Kim, and Y.-J. Yang, **(2004)**. "Internal solitons in the northeastern South China sea part 1: Sources and deep water propagation," IEEE J. Oceanic Eng., 29(4), pp. 1157-1181.

Raney, R. K., **(1995)**. "SAR systems," in Oceanographic Applications of Remote Sensing, M. Ikeda and F. W. Dobson, Eds. CRC Press, pp443-455.

Rouseff, D., A. Turgut, S. N. Wolf, S. Finette, M. H. Orr, B. Pasewark, J. Apel, M. Badiey, C. S. Chiu, R. Headrick, J. F. Lynch, J. N. Kemp, A. E. Newhall, K. von der Heydt, and D. Tielbuerger **(2002)**. "Coherence of acoustic modes propagating through shallow water internal waves," J. Acoust. Soc. Am., 111(4), pp. 1655-166.

Sakurai, J. J., **(1985)**. "Modern Quantum Mechanics," Addison-Westley, Redwood City, California.

Staples, G., and M. Dutkiewicz, **(2003)**. "SAR ocean features: Internal waves and surface wind fields – Technical report," MDA, RX-RP-51-4312.

Wright, J. W., W. J. Plant and D. L. Schuler **(1977)**. "Dual frequency remote ocean-wave spectrometer," United States Patent – 4,054,879.

Young, A. C., **(2006)**. **"**Two dimensional acoustic propagation through oceanic internal solitary waves: weak scattering theory and numerical simulation**,"** June 2006, Advisor: J. A. Colosi http://bosun.nps.edu/uhtbin/hyperion-image.exe/06Jun_Young.pdf Accessed: 19 November 2007.

Zhang, X and Cox, C. S. **(1994)**. "The spectrum of capillary-gravity and capillary wind waves observed in a wave tank," Air-Sea Interface Symposium, Marseille, France, June 24-30,1993, In "*The Air-Sea Interface*," M.A. Donelan, W.H. Hui, and W.J. Plant, eds. The University of Toronto Press, Toronto, pp. 357-365

Zheng, Q., Y. Yuan, V. Klemas and X.-H. Yan **(2001)**. "Theoretical expression for an ocean internal soliton synthetic aperture radar image and determination of the soliton characteristic half width," J. Geophys. Res., 106(C11), pp. 31415-31423.

Zhou, J., X. Zhang, and D. Rogers, **(1991)**. "Resonant interaction of sound with internal solitons in a coastal zone," J. Acoust. Soc. Am., 90, pp. 2042-2054.

INITIAL DISTRIBUTION LIST

1. Defense Technical Information Center
   Ft. Belvoir, Virginia

2. Dudley Knox Library
   Naval Postgraduate School
   Monterey, California

3. John A. Colosi
   Department of Oceanography
   Naval Postgraduate School
   Monterey, California

4. Philip A. Durkee
   Department of Meteorology
   Naval Postgraduate School
   Monterey, California

5. Mary L. Batteen
   Department of Oceanography
   Naval Postgraduate School
   Monterey, Californ

6. Fabrice Hardouin
   Centre Militaire d'Océanographie
   Service Hydrographique et Océanographique de la Marine
   Brest, France

7. Yves Morel
   Centre Militaire d'Océanographie
   Service Hydrographique et Océanographique de la Marine
   Toulouse, France